Ingenius

Ingenius • Número 21 • january/june 2019. Semester Journal of Science and Tecnology of the Universidad Politécnica Salesiana of Ecuador. Publication dedicated to studies related to the Sciences of Mechanical Engineering, Electrical Engineering, Electronic Engineering, Mechatronic Engineering, Systems Engineering and Industrial Engineering.

Editors Board

Rafael Antonio Balart Gimeno, PhD, Universidad Politécnica de Valencia, España – Editor-in-chief.

John Ignacio Calle Sigüencia, MSc, Universidad Politécnica Salesiana, Ecuador – Editor-in-chief-2.

Marlon Xavier Quinde Abril, MSc, Universidad Politécnica Salesiana, Ecuador –Deputy editor.

Scientific board

Juan López Martínez, PhD, Universidad Politécnica de Valencia, España.

Elena Fortunati, PhD, Universidad de Perugia, Italia.

Gustavo Rovelo Ruiz, PhD, Hasselt University, Diepenbeek, Bélgica.

Franklin Gavilanez Alvarez, PhD, American University, Estados Unidos.

Piedad Gañan Rojo, PhD, Universidad Pontificia Bolivariana, Colombia.

José Alex Restrepo, PhD, Universidad Simón Bolívar, Venezuela.

Sergio Lujan Mora, PhD, Universidad de Alicante, España.

Martha Zequera Díaz, PhD, Pontificia Universidad Javeriana, Colombia.

Grover Zurita, PhD, Universidad Privada Boliviana, Bolivia.

Vladimir Robles, PhD, Universidad Politécnica Salesiana, Ecuador.

Germán Arévalo, PhD, Universidad Politécnica Salesiana, Ecuador.

Wilbert Aguilar, PhD, Universidad de las Fuerzas Armadas, ESPE, Ecuador.

John Morales García, PhD, Universidad Politécnica Salesiana, Ecuador.

Jack Bravo Torres, PhD, Universidad Politécnica Salesiana, Ecuador.

Walter Orozco, PhD, Universidad Politécnica Salesiana, Ecuador.

Mariela Cerrada, PhD, Universidad Politécnica Salesiana, Ecuador.

Julio César Viola, PhD, Universidad Politécnica Salesiana, Ecuador.

Sergio Gamboa Sánchez, PhD, Universidad Nacional Autónoma de México, México.

Roger Abdón Bustamante Plaza, PhD, Universidad de Chile, Chile.

Christian Blum, PhD, Consejo Superior de Investigaciones Científicas, España.

Silvia Noemi Schiaffino, PhD, Universidad Nacional del Centro de la Provincia de Buenos Aires, Argentina.

Analía Adriana Amandi, PhD, Universidad Nacional del Centro de la Provincia de Buenos Aires, Argentina.

Rubén de Jesús Medina Molina, PhD, Universidad de Los Andes, Venezuela.

Johnny Josué Bullón Torrealba, PhD, Universidad de Los Andes, Venezuela.

Rodrigo Palma Hillerns, PhD, Universidad de Chile, Chile.

Gerardo Espinoza Pérez, PhD, Universidad Nacional Autónoma de México, México.

Alexandre Mendes Abrão, PhD, Universidad Federal de Minas Gerais, Brasil.

Kamla Abdel Radi Ismail, PhD, Universidad Estatal de Campinas Unicamp, Brasil.

Arnaldo Da Silva, PhD, Universidad Estatal de Campinas Unicamp, Brasil.

Álvaro Rocha, PhD, Universidad de Coimbra, Portugal.

José Antenor Pomilio, PhD, Universidad Estatal de Campinas Unicamp, Brasil.

Luis Paulo Reis, PhD, Universidad de Minho, Portugal.

Luís Fernandes, PhD, Escuela Superior Náutica Infante d. Henrique, Portugal.

Aníbal Traça de Almeida, PhD, Universidad de Coimbra, Portugal.

Jorge Sá Silva, PhD, Universidad de Coimbra, Portugal.

Pedro Manuel Soares Moura, PhD, Universidad de Coimbra, Portugal.

Sérgio Manuel Rodrigues Lopes, PhD, Universidad de Coimbra, Portugal.

Ricardo Madeira Soares Branco, PhD, Universidad de Coimbra, Portugal.

Carlos Alexandre Bento Capela, PhD, Universidad de Coimbra, Portugal.

Filipe Araujo, PhD, Universidad de Coimbra, Portugal.

Luis Manuel Guerra Silva Rosa, PhD, Universidad de Lisboa, Portugal.

Hélder de Jesus Fernandes, Puga, PhD, Universidad de Minho, Portugal.

Filipe Samuel, Pereira da Silva, PhD, Universidad de Minho, Portugal.

César Sequeira, PhD, Universidad de Lisboa, Portugal.

José Teixeira Estêvão Ferreira, PhD, Universidad de Coimbra, Portugal.

Nuno Laranjeiro, PhD, Universidad de Coimbra, Portugal.

Luís Amaral, PhD, Universidad de Lisboa, Portugal.

Jorge Henriques, PhD, Universidad de Coimbra, Portugal.

William Ipanaque, PhD, Universidad de Piura, Perú.

Lorenzo Leija Salas, PhD, Centro de Investigación y Estudios Avanzados del Instituto Politécnico Nacional, México.

Valeri Kontorovich Mazover, PhD, Centro de Investigación y de Estudios Avanzados del Instituto Politécnico Nacional, México.

Alejandro Ávila García, PhD, Centro de Investigación y de Estudios Avanzados del Instituto Politécnico Nacional, México.

Paolo Bellavista, PhD, Universidad de Bologna, Italia.

Carlos Rubio, PhD, Centro de Ingeniería y Desarrollo Industrial, México.

Fernando Hernández Sánchez, PhD, Centro de Investigación Científica de Yucatán, México.

Emilio Muñoz Sandoval, PhD, Instituto Potosino de Investigación Científica y Tecnológica, México.

Yasuhiro Matsumoto Kuwabara, PhD, Centro de Investigación y de Estudios Avanzados del Instituto Politécnico Nacional, México.

David Zumoffen, PhD, Centro Internacional Franco Argentino de Ciencias de la Información y de Sistemas, Argentina.

Vicente Rodríguez González, PhD, Instituto Potosino de Investigación Científica y Tecnológica, México.

Alejandro Rodríguez Ángeles, PhD, Centro de Investigación y de Estudios Avanzados del Instituto Politécnico Nacional, México.

Alistair Borthwick, PhD, Universidad de Edimburgo, Reino Unido.

Copyright. Ingenius 2019, Universidad Politécnica Salesiana. The total or partial reproduction of this journal is allowed, citing the source.

Reviewers board

Federico Dominguez, PhD, Escuela Superior Politécnica del Litoral, Ecuador.

Enrique Carrera, PhD, Universidad de las Fuerzas Armadas, ESPE, Ecuador.

Andrés Tello, MSc, Universidad de Cuenca, Ecuador.

Cristian García Bauza, PhD, Universidad Nacional del Centro de la Provincia de Buenos Aires, Argentina.

Osvaldo Añó, PhD, Universidad Nacional de San Juan, Argentina.

Thalía San Antonio, PhD, Universidad Técnica de Ambato, Ecuador.

Victor Saquicela, PhD, Universidad de Cuenca, Ecuador.

Gonzalo Olmedo, PhD, Universidad de las Fuerzas Armadas, ESPE, Ecuador.

Román Lara, PhD, Universidad de las Fuerzas Armadas, ESPE, Ecuador.

Guillermo Soriano, PhD, Escuela Superior Politécnica del Litoral, Ecuador.

María Fernanda Granda, PhD, Universidad de Cuenca, Ecuador.

Ricardo Cayssials, PhD, Universidad Tecnológica Nacional, Argentina.

Leonardo Solaque Guzman, PhD, Universidad Militar Nueva Granada, Colombia.

José Di Paolo, PhD, Universidad Nacional de Entre Ríos, Argentina.

Astrid Rubiano Fonseca, PhD, Universidad Militar Nueva Granada, Colombia.

Robinson Jiménez, PhD, Universidad Militar Nueva Granada, Colombia.

Alfonso Zozaya, PhD, Universidad de Carabobo, Venezuela.

Mauricio Mauledoux, PhD, Universidad Militar Nueva Granada, Colombia.

Luis Medina, PhD, Universidad Simón Bolivar, Venezuela.

Ernesto Cuadros-Vargas, PhD, Universidad Católica San Pablo, Perú.

Samuel Sepúlveda Cuevas, PhD, Universidad de la Frontera, Chile.

Carlos Cares, PhD, Universidad de la Frontera, Chile.

Rafael Sotelo, PhD, Universidad de Montevideo, Uruguay.

Omar Lopez, PhD, Universidad de Los Andes, Colombia.

Job Flores-Godoy, PhD, Universidad Católica del Uruguay, Uruguay.

Luis Mario Mateus, PhD, Universidad de los Andes, Colombia.

Amadeo Argüelles Cruz, PhD, Instituto Politécnico Nacional, México.

Santiago Bentancourt Parra, PhD, Universidad Pontificia Bolivariana, Colombia.

Germán Zapata, PhD, Universidad Nacional de Colombia, Colombia.

Pedro García, PhD, Universidad Autónoma de Barcelona, España.

Arturo Conde Enríquez, PhD, Universidad Autónoma de Nuevo León, México.

Alberto Cavazos González, PhD, Universidad Autónoma de Nuevo León, México.

Ernesto Vázquez Martínez, PhD, Universidad Autónoma de Nuevo León, México.

Miguel Díaz Rodriguez, PhD, Universidad de Los Andes, Venezuela.

Efraín Alcorta García, PhD, Universidad Autónoma de Nuevo León, México.

Luis Chirinos Garcia, PhD, Pontificia Universidad Católica de Perú, Perú.

Oscar Avilés, PhD, Universidad Militar Nueva Granada, Colombia.

Dora Martínez Delgado, PhD, Universidad Autónoma de Nuevo León, México.

David Ojeda, PhD, Universidad Técnica del Norte, Ecuador.

Irene Beatríz Steinmann, PhD, Universidad Tecnológica Nacional, Argentina.

Mario Serrano, Universidad Nacional de San Juan, Argentina.

Cornelio Posadas Castillo, PhD, Universidad Autónoma Nuevo León, México.

Mario Alberto Rios Mesias, PhD, Universidad de Los Andes, Colombia.

Yudith Cardinale Villarreal, PhD, Universidad Simón Bolivar, Venezuela.

Eduardo Matallanas, PhD, Universidad Politécnica de Madrid, España.

Jose Eduardo Ochoa Luna, PhD, Universidad Católica San Pablo, Perú.

Dante Angel Elias Giordano, PhD, Pontificia Universidad Católica de Perú, Perú.

Manuel Pelaez Samaniego, PhD, Universidad de Cuenca, Ecuador.

Juan Espinoza Abad, PhD, Universidad de Cuenca, Ecuador.

Pietro Codara, PhD, Universidad de Milan, Italia.

Alberto Soria, PhD, Centro de Investigación y de Estudios Avanzados del Instituto Politécnico Nacional, México.

José M. Aller, PhD, Universidad Politécnica Salesiana, Ecuador.

Ferney Amaya F., PhD, Universidad Pontificia Bolivariana, Medellin, Colombia.

Santiago Arango Aramburo, PhD, Universidad Nacional de Colombia, Colombia.

Diego Arcos–Avilés, PhD, Universidad de las Fuerzas Armadas, ESPE, Ecuador.

Pablo Arevalo, PhD, Universidad Politécnica Salesiana, Ecuador.

Roberto Beltran, MSc, Universidad de las Fuerzas Armadas, ESPE, Ecuador.

Leonardo Betancur, PhD, Universidad Pontificia Bolivariana, Medellin, Colombia.

Roberto Gamboa, PhD, Universidad de Lisboa, Portugal.

Paulo Lopes dos Santos, PhD, Universidad do Porto, Portugal.

Pedro André Dias Prates, PhD, Universidad de Coimbra, Portugal.

José Manuel Torres Farinha, PhD, Universidad de Coimbra, Portugal.

Celso de Almeida, PhD, Universidad Estatal de Campinas Unicamp, Brasil.

Ramon Molina Valle, PhD, Universidad Federal de Minas Gerais, Brasil.

Cristina Nader Vasconcelos, PhD, Universidad Federal Fluminense, Brasil.

João M. Ferreira Calado, PhD, Universidad de Lisboa, Portugal.

Guilherme Luz Tortorella, PhD, Universidad Federal de Santa Catarina, Brasil.

Mauro E. Benedet, PhD, Universidad Federal de Santa Catarina, Brasil.

Artemis Marti Ceschin, PhD, Universidade de Brasilia, Brasil.

Gilmar Barreto, PhD, Universidad Estatal de Campinas Unicamp, Brasil.

Ricardo Emilio F. Quevedo Nogueira, PhD, Universidad Federal de Ceará, Brasil.

Weslley Luiz da Silva Assis, PhD, Universidad Federal Fluminense, Brasil.

Ana P. Martinazzo, PhD, Universidad Federal Fluminense, Brasil.

Jorge Bernardino, PhD, Universidad de Coimbra, Portugal.

Luis Geraldo Pedroso Meloni, PhD, Universidad Estatal de Campinas Unicamp, Brasil.

Facundo Almeraya Calderón, PhD, Universidad Autónoma de Nuevo León, México.

Freddy Villao Quezada, PhD, Escuela Superior Politécnica del Litoral, Ecuador.

Jose Manrique Silupu, MSc, Universidad de Piura, Perú.

Germán Ariel Salazar, PhD, Instituto de Investigaciones en Energía no Convencional, Argentina.

José Mahomar Jananías, PhD, Universidad del BIOBIO, Chile.

Arnaldo Jélvez Caamaño, PhD, Universidad del BIOBIO, Chile.

Jorge Andrés Uribe, MSc, Centro de Ingeniería y Desarrollo Industrial, México.

Ricardo Beltran, PhD, Centro de Investigación en Materiales Avanzados, México.

Adi Corrales, MSc, Centro de Ingeniería y Desarrollo Industrial, México.

Jorge Uribe Calderón, PhD, Centro de Investigación Científica de Yucatán, México

José Trinidad Holguín Momaca, MSc, Centro de Investigación en Materiales Avanzados, México.

Juan Manuel Alvarado Orozco, PhD, Centro de Ingeniería y Desarrollo Industrial, México.

Arnaldo Jélvez Caamaño, PhD, Universidad del BIOBIO, Chile.

Javier Murillo, PhD, Centro Internacional Franco Argentino de Ciencias de la Información y de Sistemas, Argentina.

Lucas Daniel Terissi, PhD, Universidad Nacional de Rosario, Argentina.

Rene Vinicio Sanchez Loja, MSc, Universidad Politécnica Salesiana, Ecuador.

Freddy Leonardo Bueno Palomeque, MSc, Universidad Politécnica Salesiana, Ecuador.

Diego Cabrera Mendieta, MSc, Universidad Politécnica Salesiana, Ecuador.

Edwuin Jesus Carrasquero, PhD, Universidad Técnica de Machala, Ecuador.

Carlos Mauricio Carrillo Rosero, MSc, Universidad Técnica de Ambato, Ecuador.

Diego Carrion Galarza, MSc, Universidad Politécnica Salesiana, Ecuador.

Carmen Celi Sanchez, MSc, Universidad Politécnica Salesiana, Ecuador.

Diego Chacon Troya, MSc, Universidad Politécnica Salesiana, Ecuador.

Paul Chasi, MSc, Universidad Politécnica Salesiana, Ecuador.

Juan Chica, MSc, Universidad Politécnica Salesiana, Ecuador.

Diego Marcelo Cordero Guzmán, MSc, Universidad Católica de Cuenca, Ecuador.

Luis Javier Cruz, PhD, Universidad Pontificia Bolivariana, Medellin, Colombia.

Fabricio Esteban Espinoza Molina, MSc, Universidad Politécnica Salesiana, Ecuador.

Jorge Fajardo Seminario, MSc, Universidad Politécnica Salesiana, Ecuador.

Patricia Fernandez Morales, PhD, Universidad Pontificia Bolivariana, Medellin, Colombia.

Marcelo Flores Vazquez, MSc, Universidad Politécnica Salesiana, Ecuador.

Carlos Flores Vázquez, MSc, Universidad Católica de Cuenca, Ecuador.

Carlos Franco Cardona, PhD, Universidad Nacional de Colombia, Colombia.

Cristian García García, MSc, Universidad Politécnica Salesiana, Ecuador.

Teonila García Zapata, PhD, Universidad Nacional Mayor de San Marcos, Perú.

Luis Garzón Mñoz, PhD, Universidad Politécnica Salesiana, Ecuador.

Natalia Gonzalez Alvarez, MSc, Universidad Politécnica Salesiana, Ecuador.

Ernesto Granado, PhD, Universidad Simón Bolívar, Venezuela.

Adriana del Pilar Guaman, MSc, Universidad Politécnica Salesiana, Ecuador.

Juan Inga Ortega, MSc, Universidad Politécnica Salesiana, Ecuador.

Esteban Inga Ortega, PhD, Universidad Politécnica Salesiana, Ecuador.

Paola Ingavélez, MSc, Universidad Politécnica Salesiana, Ecuador.

Cesar Isaza Roldan, PhD, Universidad Pontificia Bolivariana.

Nelson Jara Cobos, MSc, Universidad Politécnica Salesiana, Ecuador.

Ruben Jerves, MSc, Universidad Politécnica Salesiana, Ecuador.

Victor Ramon Leal, PhD, Investigador de PDVSA, Venezuela

Gabriel Leon, MSc, Universidad Politécnica Salesiana, Ecuador.

Edilberto Llanes, PhD, Universidad Internacional SEK, Ecuador.

Luis López, MSc, Universidad Politécnica Salesiana, Ecuador.

Carlos Mafla Yépez, MSc, Universidad Técnica del Norte, Ecuador.

Hader Martínez, PhD, Universidad Pontificia Bolivariana, Medellin, Colombia

Javier Martínez, PhD, Instituto Nacional de Eficiencia Energética y Energías Renovables, Ecuador.

Alex Mayorga, MSc, Universidad Técnica de Ambato, Ecuador.

Jimmy Molina, MSc, Universidad Técnica de Machala, Ecuador.

Andres Montero, PhD, Universidad de Cuenca, Ecuador.

Vicente Morales, MSc, Universidad Tecnica de Ambato, Ecuador.

Fabián Morales, MSc, Universidad Técnica de Ambato, Ecuador.

Diego Morales, MSc, Ministerio de Electricidad y Energías Renovables del Ecuador.

Yoandrys Morales Tamayo, PhD, Universidad Técnica de Cotopaxi, Cotopaxi

Olena Leonidivna Naidiuk, MSc, Universidad Politécnica Salesiana, Ecuador.

Oscar Naranjo, MSc, Universidad del Azuay, Ecuador.

Paul Narvaez, MSc, Universidad Politécnica Salesiana, Ecuador.

Hernán Navas Olmedo, MSc, Universidad Técnica de Cotopaxi, Ecuador.

Cesar Nieto, PhD, Universidad Pontificia Bolivariana, Medellin, Colombia

Fabio Obando, MSc, Universidad Politécnica Salesiana, Ecuador.

Luis Ortiz Fernandez, MSc, Universidade Federal de Rio Grande del Norte, Brasil

Pablo Parra, MSc, Universidad Politécnica Salesiana, Ecuador.

Paulo Peña Toro, PhD, Ministerio de Productividad, Ecuador.

Patsy Prieto Velez, MSc, Universidad Politécnica Salesiana, Ecuador.

Diego Quinde Falconi, MSc, Universidad Politécnica Salesiana, Ecuador.

Diana Quintana Espinoza, MSc, Universidad Politécnica Salesiana, Ecuador.

William Quitiaquez Sarzosa, MSc, Universidad Politécnica Salesiana, Ecuador.

Flavio Quizhpi Palomeque, MSc, Universidad Politécnica Salesiana, Ecuador.

Washington Ramirez Montalvan, MSc, Universidad Politécnica Salesiana, Ecuador.

Fran Reinoso Avecillas, MSc, Universidad Politécnica Salesiana, Ecuador.

Néstor Rivera Campoverde, MSc, Universidad Politécnica Salesiana, Ecuador.

Jorge Romero Contreras, MSc, Universidad de Carabobo, Venezuela

Fabian Saenz Enderica, MSc, Universidad de las Fuerzas Armadas, ESPE, Ecuador.

Luisa Salazar Gil, PhD, Universidad Simón Bolivar, Venezuela

Gustavo Salgado Enríquez, Msc, Universidad Central del Ecuador., Ecuador.

Juan Carlos Santillán Lima, MSc, Universidad Nacional de Chimborazo

Jonnathan Santos Benítez, MSc, Universidad Politécnica Salesiana, Ecuador.

Andrés Sarmiento Cajamarca, MSc, Universidad Federal de Santa Catarina, Brasil

Luis Serpa Andrade, MSc, Universidad Politécnica Salesiana, Ecuador.

Cristian Timbi Sisalima, MSc, Universidad Politécnica Salesiana, Ecuador.

Milton Tipan Simbaña, MSc, Universidad Politécnica Salesiana, Ecuador.

Paul Torres Jara, MSc, Universidad Politécnica Salesiana, Ecuador.

Rodrigo Tufiño Cárdenas, MSc, Universidad Politécnica Salesiana, Ecuador.

Fernando Urgiles Ortíz, MSc, Universidad Politécnica Salesiana, Ecuador.

Juan Valladolid Quitoisaca, MSc, Universidad Politécnica Salesiana, Ecuador.

Efrén Vázquez Silva, PhD, Universidad Politécnica Salesiana, Ecuador.

Julio Verdugo, MSc, Universidad Politécnica Salesiana, Ecuador.

Mary Vergara Paredes, PhD, Universidad de los Andes, Merida, Venezuela

Jennifer Yepez Alulema, MSc, Universidad Politécnica Salesiana, Ecuador.

Julio Zambrano Abad, MSc, Universidad Politécnica Salesiana, Ecuador.

Patricia Zapata Molina, MSc, Universidad Politécnica Salesiana, Ecuador.

Publications board

General Editor

Luis Álvarez-Rodas, PhD

Technical board

Dra. Marcia Peña, Style Reviewer,
Centro Gráfico Salesiano - Editorial Don Bosco
Marlon Quinde Abril, MSc, Diagramming and layout
Lcda. Esthefania Sarango Coello
Ángel Torres-Toukoumidis, PhD

Publications Service

Hernán Hermosa (Coordinación General)
Marco Gutiérrez (Soporte OJS)
Paulina Torres (Edición)
Raysa Andrade (Maquetación)
Martha Vinueza (Maquetación)

Editorial

Editorial Abya Yala (Quito-Ecuador),
Av. 12 de octubre N422 y Wilson,
Bloque A, UPS Quito, Ecuador.
Casilla 17-12-719 Teléfonos: (593-2) 3962800 ext. 2638
email: editorial@abyayala.org

Translator

Adriana Curiel

Tiraje: 800 ejemplares

Typographic system used in the composition of this document LaTeX.

INGENIUS

JOURNAL OF SCIENCE AND TECHNOLOGY

Número 21, january – june 2019

ISSN impreso 1390-650X / ISSN electrónico 1390-860X

The administration of the journal is done through the following parameters:

The journal uses the academic anti-plagiarism system

The articles have an identification code (Digital Object Identifier)

The editorial process is managed through the Open Journal System

It is an open access publication (Open Access) licensed Creative Commons

The politics copyright of use postprint,are published in the Self-Archive Policy Repository Sherpa/Romeo.

The articles of the present edition can be consulted in
http://revistas.ups.edu.ec/index.php/ingenius

UNIVERSIDAD POLITÉCNICA SALESIANA DEL ECUADOR

Ingenius Journal, is indexed in the following Databases and scientific information systems:

SELECTIVE DATABASES

INDEXED IN EMERGING SOURCES CITATION INDEX CLARIVATE ANALYTICS
Google scholar
SciELO Ecuador
BASE
Fuente Académica Plus EBSCOhost
INDEXED BY LatAm Estudios+
SIS Scientific Indexing Services
EuroPub

REVIEWS EVALUATION PLATFORMS

MIAR
Quality Open Access Market
I2OR

SELECTIVE DIRECTORIES

latindex
Journal Seeker Research Bible
AcademicKeys UNLOCKING ACADEMIC CAREERS
SCIENCE LIBRARY INDEX
ULRICHSWEB™ GLOBAL SERIALS DIRECTORY

SELECTIVE SERIAL LIBRARY

redalyc.org
REDIB Red Iberoamericana de Innovación y Conocimiento Científico
refseek*

SCIENTIFIC LITERATURE SEARCHERS OPEN ACCESS

DOAJ DIRECTORY OF OPEN ACCESS JOURNALS
EXALEAD
WorldWideScience.org
Journals for Free

OTHER BIBLIOGRAPHICAL DATABASES

Dialnet
Journal TOCs The latest Journal Tables of Contents
PKP|INDEX

CATALOG OF INTERNATIONAL UNIVERSITY LIBRARIES

UNIVERSITÄT PASSAU
Fakultät für Informatik und Mathematik

BSB Bayerische StaatsBibliothek
Information in erster Linie

Deutsches Museum

Hochschule Rosenheim
University of Applied Sciences

HOCHSCHULE LANDSHUT
HOCHSCHULE FÜR ANGEWANDTE WISSENSCHAFTEN

HOCHSCHULE FÜR ANGEWANDTE WISSENSCHAFTEN MÜNCHEN

HOCHSCHULE WEIHENSTEPHAN-TRIESDORF
UNIVERSITY OF APPLIED SCIENCES

TUM
Technische Universität München

Universität der Bundeswehr München

LMU LUDWIG-MAXIMILIANS-UNIVERSITÄT MÜNCHEN

Technische Hochschule Ingolstadt

Hochschule Augsburg
University of Applied Sciences

Hochschule Kempten
University of Applied Sciences

HNU HOCHSCHULE NEU-ULM
UNIVERSITY
OF APPLIED SCIENCES

OTH OSTBAYERISCHE
TECHNISCHE HOCHSCHULE
REGENSBURG

Ostbayerische Technische Hochschule
Amberg-Weiden

Staatliche Bibliothek
Neuburg an der Donau

Staatliche Bibliothek
Regensburg

STAATS- UND
STADTBIBLIOTHEK
AUGSBURG

GEORG-SIMON-OHM
HOCHSCHULE NÜRNBERG

Universitätsbibliothek Augsburg
UBA

KATHOLISCHE UNIVERSITÄT
EICHSTÄTT-INGOLSTADT

UR Universität
Regensburg

HOCHSCHULE
ANSBACH

COBURG UNIVERSITY
of applied sciences and arts

hochschule
hof
University of Applied Sciences

HOCHSCHULE
MERSEBURG (FH)
University of Applied Sciences

ThULB THÜRINGER UNIVERSITÄTS- UND
LANDESBIBLIOTHEK JENA

EZB
Elektronische
Zeitschriftenbibliothek

OTTO-FRIEDRICH-UNIVERSITÄT BAMBERG
UNIVERSITY OF BAMBERG

UNIVERSITÄT BAMBERG

UNIVERSITÄT
BAYREUTH

FAU FRIEDRICH-ALEXANDER
UNIVERSITÄT
ERLANGEN-NÜRNBERG

Bauhaus-
Universität
Weimar

UB
WÜ

Freie Universität Berlin

FHE FACHHOCHSCHULE ERFURT UNIVERSITY OF APPLIED SCIENCES

h2
Hochschule
Magdeburg • Stendal

htw
Hochschule für Technik
und Wirtschaft Berlin
University of Applied Sciences

UB Braunschweig

STIFTUNG TIERÄRZTLICHE HOCHSCHULE HANNOVER
1778

GOTTFRIED WILHELM LEIBNIZ BIBLIOTHEK
NIEDERSÄCHSISCHE LANDESBIBLIOTHEK

Editorial

Industry 4.0: the time of digitalization, production and integration of industrial knowledge

Dear readers:

Since the first industrial revolution, the technological progress has caused the growth of industrial productivity, and in recent years advances in mobile communication and information technology have placed us in the middle of a technological development that has led to the digital transformation of the industry: the connected industry or also called the industry 4.0.

In these times and beyond the classic conception of automated systems for serial production, sensors, machines and information systems need to be connected along the entire value chain, generating data that must be transformed in knowledge to achieve an intelligent industry focused on the product and the customer.

Therefore, the mere connection and generation of data is not enough, the digitalization of the industry is only an enabler of other analytical and reasoning processes. In this sense, the industry 4.0 paradigm is an interdisciplinary approach, where very recent areas of knowledge such as the Internet of things, cyber-physical systems, cloud computing, augmented reality, data analytics, among others, interact with better known domains such as automatic learning, business architecture, integration and business architecture and information and communication technologies to lead us to an integrated, efficient and flexible industry which allow the production of high quality goods at reduced costs.

Thus, the development of Industry 4.0 proposes challenges on how to apply and implement required processes along the value chain, based on the context and requirement of each industry, and it also offers opportunities to achieve sustainable manufacturing in different areas of the production process: in business models, value-creating networks, in the organization's model, in human resources as well as in processes and products.

These challenges and opportunities need to be understood in each context, since these also allow small and medium-sized industries to enter to industry 4.0. From the point of view of academic results, according to Muhuri et al. (2019), in the article titled Industry 4.0: A Bibliometric Analysis and detailed overview published in the journal Engineering applications of Artificial Intelligence, publications and analysis of citations about Industry 4.0 in Web of Science and Scopus have recent data; in 2012 emerged the first academic article, and by 2017 194 articles had already been reported in Web of Science and 1425 articles in Scopus, with an exponential growth in the number of citations regarding the number of publications. Thus, the new proposals to meet the challenges posed by industry 4.0 wait for all of us to provide information in this domain of knowledge.

Mariela Cerrada Lozada, PhD
Scientific Board Member

Table of Contents

Review

Scientific article

Review / Revisión bibliográfica

UNIVERSIDAD POLITÉCNICA SALESIANA ECUADOR
INGENIUS
Revista de Ciencia y Tecnología
https://doi.org/10.17163/ings.n21.2019.01
pISSN: 1390-650X / eISSN: 1390-860X

FUNCTIONALIZED ENAMEL OF CERAMIC TILES BY SOL GEL TECHNIQUE (REVIEW)

DEPOSICIÓN DE CAPAS FUNCIONALES SOBRE ESMALTES CERÁMICOS MEDIANTE LA TÉCNICA SOL-GEL (REVISIÓN)

Santiago Betancourt-Parra[1,*], Manuel A. Domínguez-Ortiz[1], Diana M. Mosquera-Palacio[1], Juliana Herrera-Guerra[1], Carlos M. Ríos-Rendón[2], Carlos E. Villa[3]

Abstract

The function of enamels for the ceramic tile industry has been a research topic for the past 15 years. Different researchers have focused their efforts on achieving surfaces with functional attributes that increase product value and provide solutions for the technological needs of our times. This article presents a review of the scientific literature dedicated to obtaining functional surfaces by means of the sol-gel technique, which provides a means for deposition and formation of thin layers on traditional ceramic enamels in order to provide functional characteristics. The document presents: typically used alcoxidic solutions, the different deposition techniques emphasizing the experimental findings obtained by the authors, and a synthesis of the functional effects obtained by means of the technique.

Keywords: Ceramic enamel - Functional enamel – sol gel - ceramic

Resumen

La funcionalización de esmaltes para la industria de las baldosas cerámicas ha sido un frente de investigación importante en los últimos 15 años. Diferentes investigadores han centrado sus esfuerzos en conseguir superficies con atributos funcionales que incrementen el valor agregado del producto y a su vez aporten respuestas a las necesidades tecnológicas de nuestros tiempos. El presente artículo se centra en hacer una revisión de la literatura científica dedicada a la obtención de superficies funcionales por medio de la técnica de sol-gel, la cual es apta para la fabricación de soluciones que se depositan formando capas finas sobre los esmaltes de cerámica tradicional con el fin de aportar características funcionales al mismo. El documento presenta las principales soluciones alcóxidicas usualmente empleadas, las diferentes técnicas de deposición haciendo énfasis en los hallazgos experimentales obtenidos por los diferentes autores, y presenta una síntesis de los efectos funcionales hasta la fecha obtenidos por medio de la técnica.

Palabras clave: esmaltes cerámicos, esmaltes funcionales, sol-gel, cerámica.

[1,*] Research Group of New Materials (GINUMA), Universidad Pontificia Bolivariana (UPB), Colombia. Corresponding author ✉: santiago.betancourt@upb.edu.co http://orcid.org/0000-0003-4474-2447, http://orcid.org/0000-0003-2167-7400, http://orcid.org/0000-0003-0401-3557, http://orcid.org/0000-0002-5636-7210

[2] Product development management, Eurocerámica, Colombia, http://orcid.org/0000-0001-6816-4296

[3] Plant technical management, SENCO, Colombia, http://orcid.org/0000-0002-4971-689X

Received: 16-11-2018, accepted after review: 13-12-2018

Suggested citation: Betancourt-Parra, S.; Domínguez-Ortiz, M. A.; Mosquera-Palacio, D. M.; Herrera-Guerra, J.; Ríos-Rendón, C. M. and Villa, C. E. (2019). «Functionalized enamel of ceramic tiles by sol gel technique (review)». INGENIUS. N.°21, (january-june). pp. 9-20. DOI: https://doi.org/10.17163/ings.n21.2019.01.

1. Introduction

The ceramic enamel is a layer of glassy nature that is deposited on the surface of different substrates, of ceramic nature in general, to provide beautiful attributes and protect the surface due to its physical properties. A vast field of enamel applications include ceramic tiles, which are used for flooring and facing in the construction sector [1, 2]. As shown in Figure 1, three clearly defined layers can be distinguished in the tiles: i) the bisque, which serves as support and has the highest thickness and body in the tile, ii) the engobe, which has a thickness between 100 and 200 µm, and joins the enamel and the bisque and iii) the enamel, which is a layer of very low porosity, with a thickness between 75 a 300 µm and the aforementioned characteristics [3].

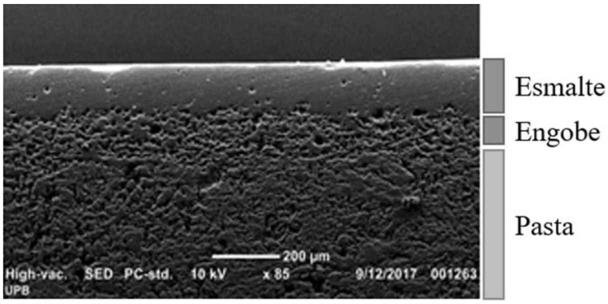

Figure 1. Cross section of a ceramic tile

Besides providing aesthetic and decorative characteristics, the enamels on such tiles can be used for other functional features. Some of the features that it is desired to improve or implement on these surfaces include: self-cleaning, energy storage, photocatalytic, antibacterial, fungicidal, high scratch resistance, inhibiting ice formation, absorb or emit substances, luminescent surfaces and even coating that can change properties when subject to a certain stimulus [4]. Nevertheless, many of the parameters which are necessary for an application at industrial scale are not sufficiently stable yet, and are still under research [5]. Therefore, this constitutes a big challenge for industry, since incorporating new technologies implies adaptation of production cycles and of routine manufacturing conditions which entails high economic investments.

To the best of our knowledge, there are various techniques available to provide functional attributes to the enamel, which include: i) modification of the enamel composition by means of incorporating substances in the enamel mix prior to the burning, ii) physical modification of the surface using plasma or chemical deposition means in vapor phase, and iii) chemical deposition of liquid solutions; the sol-gel technique is one of the most representatives of this family.

The sol-gel technique for material synthesis has been extensively proven for obtaining glassy and ceramic materials [6–10]. Wet chemistry reactions of hydrolysis and condensation produce the transformation of molecular precursors into oxide networks [11].

The following review is specifically focused in gathering scientific information, about the use of the sol-gel technique for deposition of chemical solutions in glassy enamels of ceramic tiles, in order to improve properties or provide functional attributes to the enameled surface. Figure 2 presents a graphical report of the yearly evolution of the publications about the subject, in online scientific databases and specialized books cited in the consulted literature, among which Google Scholar, Science Direct, Wiley Online Library, Springer Link, UN Institutional Repository, American Institute of Physics, Taylor & Francis Online, ACS Publications can be mentioned.

The review was carried out considering publications between 2000 and 2017, with the greater number of works being reported in the period 2009-2017. First. The report focuses on presenting the different types of alkoxides typically used. Then, it describes the different deposition techniques, emphasizing in the experimental findings obtained by different authors. At last, it presents a synthesis of the functional effects.

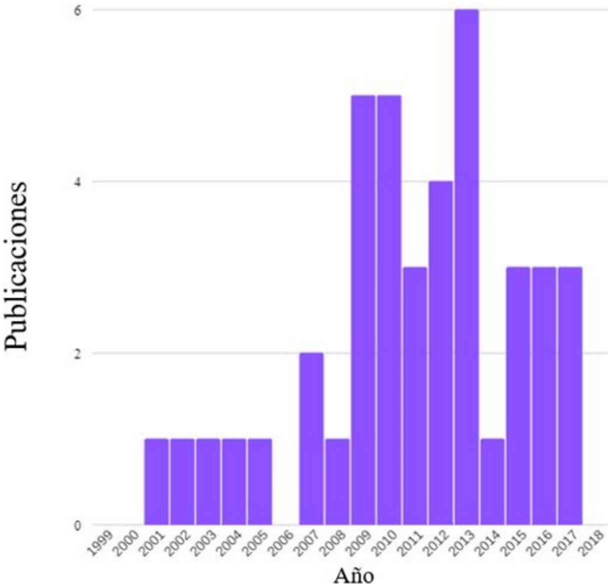

Figure 2. Report of publications per year.

2. Precursors

Table 1 presents the chemical precursors commonly employed for coating enamels using the sol-gel technique, and their corresponding structures. The precursors (starting reagent) are an alkoxide of typical chemical formula R-O-M, which are compounds that comprise a metallic ion (or another cation) represented by letter M, an oxygen molecule represented by letter O and an alkyl group R. The general reactions are expressed in Table 2, according to [12].

Table 1. Precursors

Name	Molecular formula
Titanium Isopropoxide	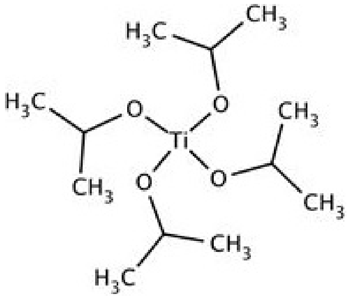
Titanium Ethoxide	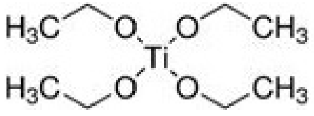
Zirconium propoxide	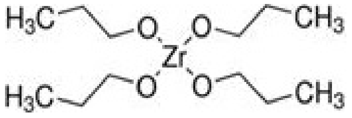
Tetra-ethyl-orthosilicates	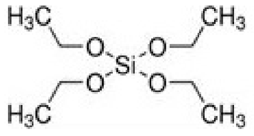

Table 2. General reactions of the sol-gel process

Hydrolisis
M-$(OR)_x$ + H-O-H → HO-$M(OR)_{x-1}$ + H-OR
Condensation
Alcoxolation $(OR)_{x-1}$ –M-OH+RO-Me-$(OR)_{x-1}$ → $(RO)_{x-1}$ –Me-O-M-$(OR)_{x-1}$ +ROH *Oxalation* $(RO)_{x-1}$ –M-OH+HO-M-$(OR)_{x-1}$ → $(RO)_{x-1}$ –M-O-M-$(OR)_{x-1}$ +HOH *Conventions:* M: Si, Ti, Zr, Hf, Ta, Nb, Al, Zn, etc. R: CH_3, C_2H_5, C_3H: 7, etc.

Once the reaction has occurred, the precursors form colloids, which are suspensions with a small dispersed phase (1-1000 nm), negligible gravitational forces and interactions being dominated by short range forces (Van der Waals attraction forces and surfaces loads). The sol is a colloidal suspension with solid particles inside a liquid.

The gel point is the moment in which the oxide bounded particles spread through the vessel that contains the colloid. During the gelation reaction, the viscosity increases until constituting a solid which adopts the form of the mold. At this point, the pore fluid mainly comprises alcohol and water, and the colloid becomes an alcogel, which can be removed from the container and can stand by itself [13].

Figure 3 is a schematic representation made by [6]. The aerogels are obtained when the liquid-filled pore is replaced by air, without altering the structure or the volume of the gel body.

In the sol-gel process, the reactions depend upon various parameters such as:

- Composition and concentration of the precursors (alkoxide and solvent)
- Amount of water added
- Type and concentration of the catalyst employed
- Additional additives such as desiccants
- Sequence in which the components are added
- Mixing time
- Aging time
- Mixing conditions (efficiency of the mixture, agitation by ultrasound, atmosphere)
- Temperature

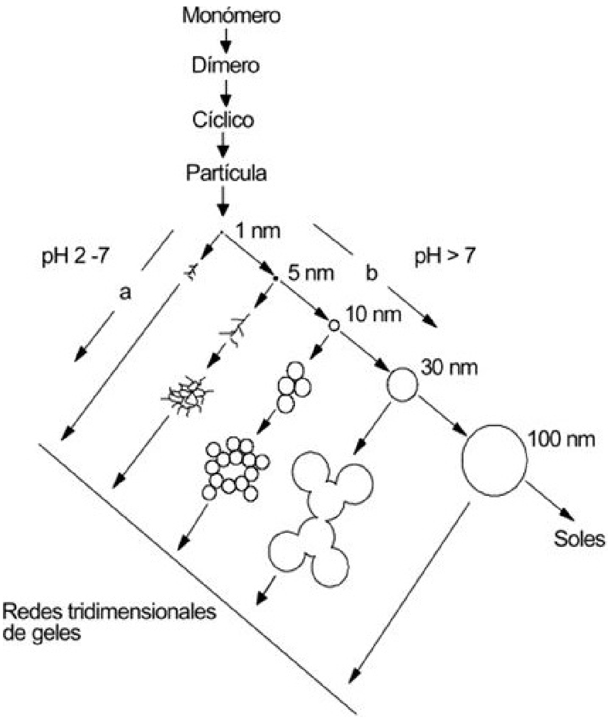

Figure 3. Schematic representation of the sol-gel process [6].

3. Deposition techniques

Regarding the deposition techniques, this sections presents the remarkable findings reported in the reviewed literature, which are complemented with the information presented in Table 3 that summarizes characteristics of the reported techniques.

3.1. Spin

This technique is based on the deposition of small amounts of solution on the surface of a substrate that spins at a high speed, such that the solution disperses due to the centrifugal force, forming a homogeneous liquid film. The solution quickly evaporates the solvent and the oxide molecules are deposited on the substrate. The thickness of the film directly depends on the following variables: speed of rotation, viscosity, contents of solvent and its properties when evaporating.

There are mathematical models of the variation of the thickness, which are described in detail in [12–17]. Thin layer coatings, with a thickness between 0,1 and 10 μm, can be obtained with this technique [18].

This technique has been extensively used in applications which require the formation of uniform films, namely with homogeneous thickness and low rugosity [19]. For this reason, it is employed in manufacturing electronic micro components and has been of interest to obtain highly glossy enamels for tiles, since a reduction of the rugosity of a surface increases its gloss [2].

3.2. Dip

The dip coating deposition technique involves totally immersing the substrate in the solution, and further removing it at a controlled speed [20, 21] under environmental conditions. According to some researchers, it is considered the simplest technique to deposit films on the surface of a substrate, which may be either flat or curved [11]. Indeed, they state that it can be implemented on surfaces with areas in the order of square meters.

The thickness of the film directly depends upon the velocity of substrate retraction and the viscosity of the solution; low velocities are appropriate to obtain thin films, with a thickness between 0.3 and 3 μm, and rugosity between 60 and 690 nm [18].

In 2007, Kuisma *et al.* [22] studied the cleaning capacity of ZrO_2 and TiO_2 thin films, deposited using the dip coating technique on the surface of enameled ceramic tiles of dimension 3.0 x 3.0 cm. Using topographic measurements, this work showed that for higher roughness of the ceramic enamel, more organic material gets adhered to the surface.

On the other hand, Piispanen *et al.* [23] characterized the effects of the resistance to a chemical attack (stained) and cleaning of two tiles, one with dull finish and the other with glossy finish, with TiO_2 and ZrO_2 films deposited using the dip coating technique. It was determined that the TiO_2 coating has greater cleaning and self-cleaning capacity after being exposed to UV light. The authors indicated that the cleaning capacity of glossy glassy surfaces was not steep, and the zirconium coatings could negatively affect the enamels self-cleaning capacity.

Hofer *et al.* [24] studied the thermal stability and the active photocatalytic property of titanium, deposited on ceramic surfaces (enameled substrates and non-enameled corundum substrates) with a coated area of dimension 2.5 × 4.0 cm, using a dip coating process. It was found that the thermal stability reduction depends on the composition of the substrate, thus making evident a slight variation on the electronic structure of the titanium, which indicated weak interactions between the silica and the titanium.

Similar results were reported in a study of the coating of ceramic tiles and window glasses with thin films of nano TiO_2, using dip and spray deposition techniques, showing a good self-cleaning performance of the coatings [25].

In addition, it has been used to obtain antibacterial effects on glassy substrates of ceramic tiles against *Escherichia coli* y *Staphylococcus aureus*, using solutions of Ag/SiO_2 [26] deposited on the enameled surface of the tiles by means of a dip coating technique. They achieved an excellent antibacterial performance against both types of bacteria related to a high synthetizing temperature of the deposited layer, since after this treatment the silver ions are constantly released, which generates variations in their concentrations thus inhibiting the growth of these bacteria.

Soares *et al.* [27] used the sol-gel technique for producing thick coatings of silica and silica/zirconium colloidal particles, on glassy-ceramic substrates of the system Li_2O-Al_2O_3-SiO_2, in order to increase if resistance to scratch and wear. The deposition was carried out at a retraction speed of 5 cm/min. Compared with the results obtained with the substrate without coating, it was found an improvement in the final look of the surface for the functional coatings; nevertheless, the resistance to wear kept constant compared with the samples without coating.

In addition, Zhang *et al.* [28] studied the effects of incorporating titanium nano particles to solutions of tetraethyl orthosilicate (TEOS) deposited on commercial white glassy ceramic tiles (25 × 25 × 5 mm), by means of a dip coating technique in which the substrates were submerged during 3 minutes and further removed at 1 mm/s. This research verified a better dispersion for the particles of P25-TiO_2/TEOS, with a greater surface area and rugosity, and a smaller particle size compared to the particles of P25-TiO_2, which produced a better hydrophilicity and a greater photocatalytic activity, under irradiation of visible light.

López *et al.* [29] examined the effect of different types of substrate, on the morphology of the surface and the photocatalysis of a great scale TiO_2 film. The impregnation was carried out by dip coating; specifically, for the cases of a glassy substrate of soda-lime ground with acid (12 × 21.5 cm), a SiO_2 barrier layer was deposited with a retraction velocity of 5 cm/min.

On the other hand, the substrates (12 × 21.5 cm) of sodium-lime glazed with acid, glassy soda-lime glazed with acid previously coated with a SiO_2 barrier layer, enameled ceramic tile and 6061 aluminum alloy, were impregnated with a TiO_2 film. These tests determined that the phase and microstructure of the TiO_2 film are exclusively anatase. Additionally, it was found a significant variation in the growth of the TiO_2 crystals and the morphology and thickness of the film with respect to the substrate being used, which in turn affects the photocatalytic activity.

The studies carried out by Hazmaliza *et al.* [30] showed the antibacterial performance of the anatase mixed with enamel applied on ceramic tiles, using two different sizes of anatase powder (micrometric and nano). For conducting these experiments, the concentration by weight of the anatase powder in microns was varied, while the size nano anatase was established on a fixed value. The results obtained show a slight variation in the color of the manufactured tile, which becomes more yellowish as the anatase composition increases. Similarly, it is evident that the antibacterial properties increase when the composition of nanometric anatase is greater compared to the micrometric, due to larger area of antibacterial agents on the tile. Likewise, as the composition of anatase powder is greater, the enamel viscosity will be larger.

It is important to note that research has been also conducted related to the application of this technique, in the TiO_2 self-cleaning coating of clay roof tiles (1 × 1 × 0.8 cm) [31]. The authors demonstrated that a TiO_2 photocatalytic coating in the anatase nanocrystalline phase applied under industrial conditions for thin film (0,399 mg of suspension/tile surface cm^2), has a better photocatalytic activity in the decomposition of methylene blue, hydrophilicity and antimicrobial activity, than a thick (0.885 mg suspension/ cm^2) photocatalytic coating.

3.3. Spray

This deposition technique consists of a process of spray or vertical atomization of a stationary liquid solution or in linear movement, where a fluid beam driven by compressed air is fragmented into disperse drops that collide on a substrate. There are many variables associated to the correct operation of the spray, namely flow of solution, pressure of the compressed air, type of nozzle and nozzle-substrate distance, among others [32]. Such variables influence on the size, shape, velocity and drop strength of collision; these are also related to fluid properties (surface tension, density and viscosity).

After the collision, a heat transfer occurs between the drops and the surrounding air, thus evaporating the solvent through the boundary layer around each drop. At the end of the evaporation, the drops adhere to the glassy surface creating a thin layer coating with a thickness between 0.1 and 3 μm [18].

This deposition technique does not have limitations in terms of the substrate size, since the aperture angle of the application gun can be adjusted. It requires a small amount of solution because the deposition is carried out only on the enameled surface, thus reducing costs and minimizing the environmental impact since it is not necessary to use a vacuum to eliminate the gases emerging from the process [33–35].

Bondioli *et al.* [36] studied the functionalization of the surfaces of industrial ceramic tiles by means of the sol-gel technique, to improve the cleaning capacity of non-enameled thin porcelain stoneware, preparing TiO_2-SiO_2 coatings with different concentration of titanium that were deposited using an airbrush. This work reports that films are transparent, they do not modify the stoneware gloss and show good adhesion. In addition, they yield a greater catalytic effect at high synthetizing temperatures, which produces a self-cleaning and self-sterilizing ceramic surface that may also degrade various organic contaminants in the surrounding environment.

Savvova *et al.* [37] developed TiO_2 coatings on ceramic enamels, determining the multi-functionality of this material by reporting its substantial (70-90 %) antibacterial and antifungal properties. Once again Bondioli *et al.* [38, 39] reported the functionalization of the surfaces of ceramic tiles, but this time focusing on soluble salts (alternative coloring processes of ceramic materials without enamel) to improve mechanical properties (resistance to scratch and wear) and the conductivity.

For that purpose, solutions with different concentrations of zirconium, titanium and silver were prepared, and 300 g/cm^2 were applied with airbrush on green unfired bisque. It was visualized that the addition of zirconium soluble salts increased the scratch resistance, while simultaneously maintaining the final aesthetic appearance of the ceramic tiles. The results obtained for titanium and silver were similar to the results already mentioned for zirconium, with the difference that a multi-functional layer is generated.

3.4. Screen

The serigraphy or screen imprinting enables the realization of two-dimensional designs, which makes it useful in industrial processes [40]. The serigraphic processes require a knitting material, that may be synthetic fiber of steel mesh tensioned and bonded to a frame, which is covered with an emulsion that is impermeable to the coating solution in the area in which no printing should appear.

It is a technique that virtually does not cause losses of the coating solution during printing, because the frame goes across the screen at a constant velocity, and after performing the application it goes backwards in order to repeat the procedure.

Due to its versatility, this method has been utilized for 50 years in the ceramic industry to deposit enamels and decorate tiles [18]. For this type of substrates, processes that generate a TiO_2 thin layer using the sol-gel technique, produce thicknesses between 5 and 35 µm, taking into account that both the thickness and the amount of applied material can vary according to the application percentage of the screen, which includes the volume between the screen threads and the thickness of the emulsion [40].

Since not all the material is deposited on the screen, the thickness of the wet layer also depends on the strength and the trawl speed of the frame, the screen-substrate distance, and the viscosity of the deposited solution [40].

In 2008, São Marcos *et al.* [41] studied the TiO_2 layers deposited by means of serigraphy (55 and 136 µm sifting) at 25 and 50 g/m2 on enameled single-pore tiles. They determined that the layers gave more than 90% efficiency 6 to 8 h after performing the Orange II discoloration, under visible artificial light without layer deactivation; this yielded acceptable levels of discoloration in reasonable periods of time.

In the following year, these researchers [42] characterized and determined the photocatalytic degradation of Orange II, for active ZnO layers deposited at 25 and 50 g/m^2 by means of different sifting screens (55 and 135 µm), using single-pore tiles with glossy enamel (20 × 10 cm from Revigrés, PT); in this case, results revealed a considerable discoloration performance of Orange II (more than 50% efficiency after 6 to 8 h, with a maximum attenuation degree of 72%), under artificial visible light or by direct exposure to sun light. For this effect, the TiO_2 and ZnO layers avoid the elimination of the photocatalyst at the end of the process.

For the same year, Rego *et al.* [43] used the materials previously described to determine the photocatalytic degradation of the Orange II coloring in aqueous solutions, under direct exposure to sun light. For this purpose, TiO_2 and ZnO layers were deposited with 50 g/m^2 on ceramic tiles of single-pore glossy commercial enamels (20 × 20 cm from Revigrés, PT) by means of a serigraphic process where sifting screens were used (136 µm).

This layers exhibited a greater performance for the TiO_2, besides a maximum degree of color attenuation of 90%. On the other hand, in 2011 Seabra *et al.* [44] evaluated the photocatalytic behavior of titanium layers deposited by spray and serigraphy, and the former gave a better coverage with small rugosity levels.

Table 3. Characteristics and publications per deposition technique

Technique	**SPIN**	**DIP**	**SPRAY**	**SCREEN**
Graphic representation	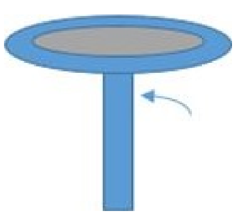	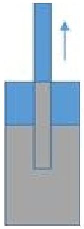		
Typical curve of behavior of thickness as a function of the process variables	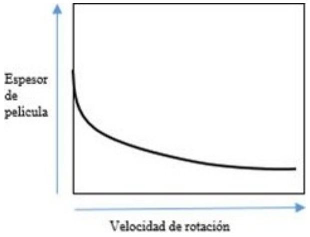	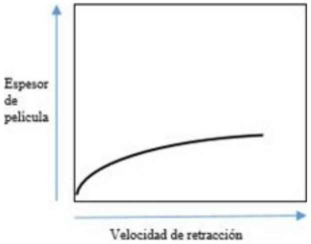	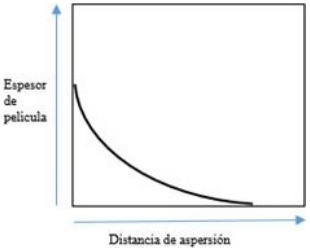	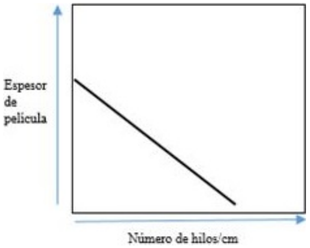
Thickness range	0,1-10 µm	0,3-3 µm	0,1-3 µm	5-55 µm
AntibacteriaL		[26, 30]	[45–47]	
Photocatalysis	[29]	[21–25, 28, 29, 31]	[25, 35, 36, 48–58]	[40–44, 48]
Scratch resistence		[27]	[36–39]	

4. Applications

Figure 4 illustrates the distribution of the consulted literature according to the desired application. It is clearly seen that the applications associated to photocatalysis and antibacterial effect have mainly received the attention. Less than 10% of these researches have focused in increasing the scratch resistance of the surfaces. A brief description of this type of applications is presented in the following.

4.1. Photocatalysis

The absorption of photons coming with light with enough energy (equal or greater than the energy band of the catalyst), promotes catalytic reactions in the surface of the material, generating excitons (pairs e^- – h^+). Such excitons can be used to produce redox reactions [59].

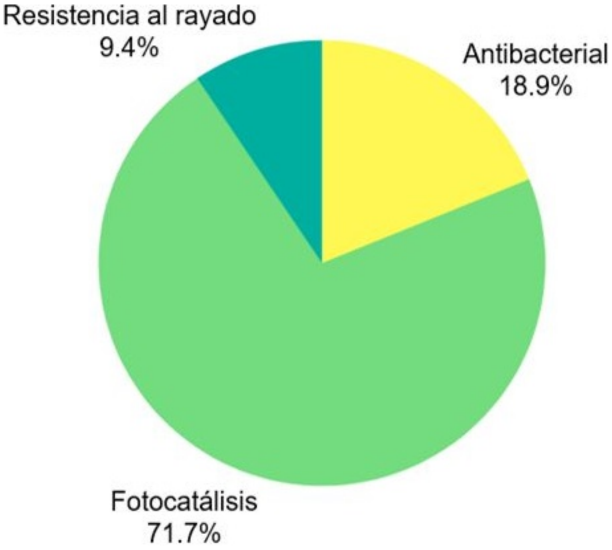

Figure 4. Distribution of research works according to applications.

The main purpose of obtaining coatings with catalytic functions using titanium and its variations on enameled ceramic surfaces, is the self-cleaning such as it is reported in the revision conducted by [18]. This characteristic is the combination of two phenomena: the catalyst action on particular substances (CO_2, COVs) and the superhydrophobicity of the titanium. Some authors also ensure the possible elimination of NO_x, CO, SO_x from the air [60, 61].

4.2. Antibacterial

One of the effects of the interactions between the free radicals (ions and excitons) deposited on the surfaces, is the significant reduction of the growth of microorganisms. The reduction mechanism is based in blocking the aerobic activity of the microorganism, due to the absence of oxygen in the medium.

This application has been of great interest in public places highly exposed to conditions of growth of microorganisms, such as health facilities (clinics, hospitals, surgery rooms), schools and colleges, as it has been proposed in [62].

4.3. Scratch resistence

Behind the improvement of this property, underlie aspects related with the improvement in other properties such as the useful life of the surfaces and their attributes, namely: gloss, color, texture, hardness, among others, which are affected by the wear due to friction phenomena to which the ceramic products are subjected.

The possibility of forming nano and micrometric ceramic layers with crystalline structure, instead of the amorphous structure typical of the glassy enamels, has demonstrated notorious increments in the response of the surface regarding scratch resistance [63].

5. Conclusions

After conducting this revision, it was found that the sol-gel technique has been employed for manufacturing solutions that are deposited in thin layers on traditional ceramic enamels, in order to provide it with functional characteristics. The reported literature mainly corresponds to researchers located in Italy, Brazil and Portugal. The surfaces with photocatalyst (self-cleaning) functional attributes have been a major axis that has motivated the research works in this area. In addition, the broad market and the potential positive effect have driven innovations for the industry.

Even though this is a research topic from 2000, with a strong boost from 2007, the researches in other functionalities seem to be susceptible of being studied, because it is possible to coat enamels with alkoxidic solutions using the sol-gel technique.

References

[1] O. J. Restrepo Baena, *Baldosas cerámicas y gres porcelánico: un mundo en permanente evolución*, C. E. F. de Minas, Ed. Universidad Nacional de Colombia, Sede Medellín, 2011. [Online]. Available: https://goo.gl/sSTprJ

[2] L. Fröberg and L. Hupa, "Topographic characterization of glazed surfaces," *Applied Surface Science*, vol. 254, no. 6, pp. 1622–1629, 2008. [Online]. Available: https://doi.org/10.1016/j.apsusc.2007.07.173

[3] R. Casasola, J. M. Rincón, and M. Romero, "Glass–ceramic glazes for ceramic tiles: a review," *Journal of Materials Science*, vol. 47, no. 2, pp. 553–582, Jan 2012. [Online]. Available: https://doi.org/10.1007/s10853-011-5981-y

[4] A. Moreno Berto, "Ceramic tiles: Above and beyond traditional applications," *Journal of the European Ceramic Society*, vol. 27, no. 2, pp. 1607–1613, 2007. [Online]. Available: https://doi.org/10.1016/j.jeurceramsoc.2006.04.146

[5] M. Raimondo, G. Guarini, C. Zanelli, F. Marani, L. Fossa, and M. Dondi, "Printing nano tio$_2$ on large-sized building materials: Technologies, surface modifications and functional behaviour," *Ceramics International*, vol. 38, no. 6, pp. 4685–4693, 2012. [Online]. Available: https://doi.org/10.1016/j.ceramint.2012.02.051

[6] J. González Hernández, J. Pérez Robles, F. Ruiz, and J. Martínez, "Vidrios SiO$_2$ nanocompuestos preparados por sol-gel: revisión," *Superficies y vacío*, no. 11, pp. 1–16, 2000. [Online]. Available: https://goo.gl/cVrCwj

[7] C. J. Brinker and G. W. Scherer, *Sol-Gel Science: The Physics and Chemistry of Sol–Gel Processing.* San Diego: Academic Press, 1990. [Online]. Available: https://doi.org/10.1016/B978-0-08-057103-4.50007-6

[8] M. Guglielmi and G. Carturan, "Precursors for sol-gel preparations," *Journal of Non-Crystalline Solids*, vol. 100, no. 1, pp. 16–30, 1988. [Online]. Available: https://doi.org/10.1016/0022-3093(88)90004-X

[9] J. Livage and D. Ganguli, "Sol-gel electrochromic coatings and devices: A review," *Solar Energy Materials and Solar Cells*, vol. 68, no. 3, pp. 365–381, 2001. [Online]. Available: https://doi.org/10.1016/S0927-0248(00)00369-X

[10] J. Livage, "Sol-gel processes," *Current Opinion in Solid State and Materials Science*, vol. 2, no. 2, pp. 132–138, 1997. [Online]. Available: https://doi.org/10.1016/S1359-0286(97)80057-5

[11] L. Znaidi, "Sol-gel-deposited zno thin films: A review," *Materials Science and Engineering: B*, vol. 174, no. 1, pp. 18–30, 2010. [Online]. Available: https://doi.org/10.1016/j.mseb.2010.07.001

[12] D. Chen, "Anti-reflection (ar) coatings made by sol-gel processes: A review," *Solar Energy Materials and Solar Cells*, vol. 68, no. 3, pp. 313–336, 2001. [Online]. Available: https://doi.org/10.1016/S0927-0248(00)00365-2

[13] S. Attia, J. Wang, G. Wu, J. Shen, and J. Ma, "Review on sol-gel derived coatings: Process, techniques and optical applications," *Journal of Materials Science & Technology*, vol. 18, no. 3, pp. 211–218, 2002. [Online]. Available: https://doi.org/10.3321/j.issn:1005-0302.2002.03.005

[14] D. Meyerhofer, "Characteristics of resist films produced by spinning," *Journal of Applied Physics*, vol. 49, no. 7, pp. 3993–3997, 1978. [Online]. Available: https://doi.org/10.1063/1.325357

[15] J. H. Lai, "An investigation of spin coating of electron resists," *Polymer Engineering & Science*, vol. 19, no. 15, pp. 1117–1121, 1979. [Online]. Available: https://doi.org/10.1002/pen.760191509

[16] J. Martín-Márquez, J. M. Rincón, and M. Romero, "Effect of firing temperature on sintering of porcelain stoneware tiles," *Ceramics International*, vol. 34, no. 8, pp. 1867–1873, 2008. [Online]. Available: https://doi.org/10.1016/j.ceramint.2007.06.006

[17] D. B. Hall, P. Underhill, and J. M. Torkelson, "Spin coating of thin and ultrathin polymer films," *Polymer Engineering & Science*, vol. 38, no. 12, pp. 2039–2045, 1998. [Online]. Available: https://doi.org/10.1002/pen.10373

[18] A. L. da Silva, M. Dondi, M. Raimondo, and D. Hotza, "Photocatalytic ceramic tiles: Challenges and technological solutions," *Journal of the European Ceramic Society*, vol. 38, no. 4, pp. 1002–1017, 2018. [Online]. Available: https://doi.org/10.1016/j.jeurceramsoc.2017.11.039

[19] C. A. Otálora Bastidas, "Desarrollo de materiales usados en la fabricación de celdas solares orgánicas," Master's thesis, Universidad Nacional de Colombia, Bogotá, Colombia, 2013. [Online]. Available: https://goo.gl/4kKihE

[20] C. Terrier, J. Chatelon, R. Berjoan, and J. Roger, "Sb-doped SnO$_2$ transparent conducting oxide from the sol-gel dip-coating technique," *Thin Solid Films*, vol. 263, no. 1, pp. 37–41, 1995. [Online]. Available: https://doi.org/10.1016/0040-6090(95)06543-1

[21] S. Kato, S. Kato, H. Taoda, and S. Katoh, "Thin film coating of photocatalytics on ultra light ceramic tile by use of supercritical fluid," *High Pressure Research*, vol. 20, no. 1-6, pp. 415–419, 2001. [Online]. Available: https://doi.org/10.1080/08957950108206189

[22] R. Kuisma, L. Fröberg, H.-R. Kymäläinen, E. Pesonen-Leinonen, M. Piispanen, P. Melamies, M. Hautala, A.-M. Sjöberg, and L. Hupa,

"Microstructure and cleanability of uncoated and fluoropolymer, zirconia and titania coated ceramic glazed surfaces," *Journal of the European Ceramic Society*, vol. 27, no. 1, pp. 101–108, 2007. [Online]. Available: https://doi.org/10.1016/j.jeurceramsoc.2006.02.035

[23] M. Piispanen, J. Määttä, S. Areva, A.-M. Sjöberg, M. Hupa, and L. Hupa, "Chemical resistance and cleaning properties of coated glazed surfaces," *Journal of the European Ceramic Society*, vol. 29, no. 10, pp. 1855–1860, 2009. [Online]. Available: https://doi.org/10.1016/j.jeurceramsoc.2008.11.007

[24] M. Hofer and D. Penner, "Thermally stable and photocatalytically active titania for ceramic surfaces," *Journal of the European Ceramic Society*, vol. 31, no. 15, pp. 2887–2896, 2011. [Online]. Available: https://doi.org/10.1016/j.jeurceramsoc.2011.07.016

[25] K. Murugan, R. Subasri, T. Rao, A. S. Gandhi, and B. Murty, "Synthesis, characterization and demonstration of self-cleaning tio2 coatings on glass and glazed ceramic tiles," *Progress in Organic Coatings*, vol. 76, no. 12, pp. 1756–1760, 2013. [Online]. Available: https://doi.org/10.1016/j.porgcoat.2013.05.012

[26] N. Baheiraei, F. Moztarzadeh, and M. Hedayati, "Preparation and antibacterial activity of Ag/SiO_2 thin film on glazed ceramic tiles by sol-gel method," *Ceramics International*, vol. 38, no. 4, pp. 2921–2925, 2012. [Online]. Available: https://doi.org/10.1016/j.ceramint.2011.11.068

[27] V. Soares, P. Soares, O. Peitl, E. Zanotto, A. Durán, and Y. Castro, "Resistencia al desgaste de recubrimientos sol-gel de SiO_2 y SiO_2 - ZrO_2 sobre materiales vitrocerámicos obtenidos por sinterización," *Boletín la Sociedad Española De Cerámica y Vidrio*, vol. 52, no. 5, pp. 225–230, 2013. [Online]. Available: https://doi.org/10.3989/cyv.272013

[28] P. Zhang, J. Tian, R. Xu, and G. Ma, "Hydrophilicity, photocatalytic activity and stability of tetraethyl orthosilicate modified tio2 film on glazed ceramic surface," *Applied Surface Science*, vol. 266, pp. 141–147, 2013. [Online]. Available: https://doi.org/10.1016/j.apsusc.2012.11.117

[29] L. Lopez, W. A. Daoud, D. Dutta, B. C. Panther, and T. W. Turney, "Effect of substrate on surface morphology and photocatalysis of large-scale TiO_2 films," *Applied Surface Science*, vol. 265, pp. 162–168, 2013. [Online]. Available: https://doi.org/10.1016/j.apsusc.2012.10.156

[30] M. Hasmaliza, H. Foo, and K. Mohd, "Anatase as antibacterial material in ceramic tiles," *Procedia Chemistry*, vol. 19, pp. 828–834, 2016. [Online]. Available: https://doi.org/10.1016/j.proche.2016.03.109

[31] M. Hadnadjev, J. Ranogajec, S. Petrovic, S. Markov, V. Ducman, and R. Marinkovic-Neducin, "Design of self-cleaning tio_2 coating on clay roofing tiles," *Philosophical Magazine*, vol. 90, no. 22, pp. 2989–3002, 2010. [Online]. Available: https://doi.org/10.1080/14786431003767017

[32] B. Yu, D. Vak, J. Jo, S. Na, S. Kim, M. Kim, and D. Kim, "Factors to be considered in bulk heterojunction polymer solar cells fabricated by the spray process," *IEEE Journal of Selected Topics in Quantum Electronics*, vol. 16, no. 6, pp. 1838–1846, Nov 2010. [Online]. Available: https://doi.org/10.1109/JSTQE.2010.2042282

[33] F. Aziz and A. Ismail, "Spray coating methods for polymer solar cells fabrication: A review," *Materials Science in Semiconductor Processing*, vol. 39, pp. 416–425, 2015. [Online]. Available: https://doi.org/10.1016/j.mssp.2015.05.019

[34] S. Colella, M. Mazzeo, G. Melcarne, S. Carallo, G. Ciccarella, and G. Gigli, "Spray coating fabrication of organic solar cells bypassing the limit of orthogonal solvents," *Applied Physics Letters*, vol. 102, no. 20, p. 203307, 2013. [Online]. Available: https://doi.org/10.1063/1.4807464

[35] C. Sciancalepore and F. Bondioli, "Durability of SiO_2-TiO_2 Photocatalytic Coatings on Ceramic Tiles," *International Journal of Applied Ceramic Technology*, vol. 12, no. 3, pp. 679–684, 2015. [Online]. Available: https://doi.org/10.1111/ijac.12240

[36] F. Bondioli, R. Taurino, and A. Ferrari, "Functionalization of ceramic tile surface by sol-gel technique," *Journal of Colloid and Interface Science*, vol. 334, no. 2, pp. 195–201, 2009. [Online]. Available: https://doi.org/10.1016/j.jcis.2009.02.054

[37] O. V. Savvova and L. L. Bragina, "Use of titanium dioxide for the development of antibacterial glass enamel coatings," *Glass and Ceramics*, vol. 67, no. 5, pp. 184–186, Nov 2010. [Online]. Available: https://doi.org/10.1007/s10717-010-9258-8

[38] F. Bondioli, T. Manfredini, M. Giorgi, and G. Vignali, "Functionalization of ceramic tile surface by soluble salts addition: Part i," *Journal of the European Ceramic Society*, vol. 30, no. 1, pp. 11–16, 2010. [Online]. Available: https://doi.org/10.1016/j.jeurceramsoc.2009.08.012

[39] F. Bondioli, M. Dinelli, R. Giovanardi, and M. Giorgi, "Functionalization of ceramic tile surface by soluble salts addition: Part ii. titanium and silver addition," *Journal of the European Ceramic Society*, vol. 30, no. 9, pp. 1873–1878, 2010. [Online]. Available: https://doi.org/10.1016/j.jeurceramsoc.2010.03.008

[40] F. C. Krebs, "Fabrication and processing of polymer solar cells: A review of printing and coating techniques," *Solar Energy Materials and Solar Cells*, vol. 93, no. 4, pp. 394–412, 2009. [Online]. Available: https://doi.org/10.1016/j.solmat.2008.10.004

[41] P. S. Marcos, J. Marto, T. Trindade, and J. Labrincha, "Screen-printing osol-g$_2$ photocatalytic layers on glazed ceramic tiles," *Journal of Photochemistry and Photobiology A: Chemistry*, vol. 197, no. 2, pp. 125–131, 2008. [Online]. Available: https://doi.org/10.1016/j.jphotochem.2007.12.017

[42] J. Marto, P. S. Marcos, T. Trindade, and J. Labrincha, "Photocatalytic decolouration of orange ii by zno active layers screen-printed on ceramic tiles," *Journal of Hazardous Materials*, vol. 163, no. 1, pp. 36–42, 2009. [Online]. Available: https://doi.org/10.1016/j.jhazmat.2008.06.056

[43] E. Rego, J. Marto, P. S. Marcos, and J. Labrincha, "Decolouration of orange ii solutions by tio2 and zno active layers screen-printed on ceramic tiles under sunlight irradiation," *Applied Catalysis A: General*, vol. 355, no. 1, pp. 109–114, 2009. [Online]. Available: https://doi.org/10.1016/j.apcata.2008.12.005

[44] M. Seabra, R. Pires, and J. Labrincha, "Ceramic tiles for photodegradation of orange ii solutions," *Chemical Engineering Journal*, vol. 171, no. 2, pp. 692–702, 2011. [Online]. Available: https://doi.org/10.1016/j.cej.2011.04.028

[45] A. Ghafari-Nazari, F. Moztarzadeh, S. M. Rabiee, T. Rajabloo, M. Mozafari, and L. Tayebi, "Antibacterial activity of silver photodeposited nepheline thin film coatings," *Ceramics International*, vol. 38, no. 7, pp. 5445–5451, 2012. [Online]. Available: https://doi.org/10.1016/j.ceramint.2012.03.055

[46] M. Machida, K. Norimoto, and T. Kimura, "Antibacterial activity of photocatalytic titanium dioxide thin films with photodeposited silver on the surface of sanitary ware," *Journal of the American Ceramic Society*, vol. 88, no. 1, pp. 95–100, 2005. [Online]. Available: https://doi.org/10.1111/j.1551-2916.2004.00006.x

[47] J. Szczawiński, H. Tomaszewski, A. Jackowska-Tracz, and M. Szczawińska, "Survival of Staphylococcus aureus exposed to UV radiation on the surface of ceramic tiles coated with TiO_2," *Polish Journal of Veterinary Sciences*, vol. 14, no. 1, pp. 41–46, 2011. [Online]. Available: https://doi.org/10.2478/v10181-011-0006-y

[48] C. L. Bianchi, B. Sacchi, S. Capelli, C. Pirola, G. Cerrato, S. Morandi, and V. Capucci, "Micro-sized tio$_2$ as photoactive catalyst coated on industrial porcelain grès tiles to photodegrade drugs in water," *Environmental Science and Pollution Research*, vol. 25, no. 21, pp. 20 348–20 353, Jul 2018. [Online]. Available: https://doi.org/10.1007/s11356-017-9066-6

[49] A. M. Buckley and M. Greenblatt, "The sol-gel preparation of silica gels," *Journal of Chemical Education*, vol. 71, no. 7, p. 599, 1994. [Online]. Available: https://doi.org/10.1021/ed071p599

[50] A. L. da Silva, M. Dondi, and D. Hotza, "Self-cleaning ceramic tiles coated with Nb_2O5-doped-TiO_2 nanoparticles," *Ceramics International*, vol. 43, no. 15, pp. 11 986–11 991, 2017. [Online]. Available: https://doi.org/10.1016/j.ceramint.2017.06.049

[51] A. L. da Silva, D. N. Muche, S. Dey, D. Hotza, and R. H. Castro, "Photocatalytic nb$_2$o$_5$-doped tio$_2$ nanoparticles for glazed ceramic tiles," *Ceramics International*, vol. 42, no. 4, pp. 5113–5122, 2016. [Online]. Available: https://doi.org/10.1016/j.ceramint.2015.12.029

[52] S. Niederhãusern, M. Bondi, and F. Bondioli, "Self-cleaning and antibacteric ceramic tile surface," *International Journal of Applied Ceramic Technology*, vol. 10, no. 6, pp. 949–956, 2013. [Online]. Available: https://doi.org/10.1111/j.1744-7402.2012.02801.x

[53] V. Ducman, V. Petrovič, and S. D. Škapin, "Photo-catalytic efficiency of laboratory made and commercially available ceramic building products," *Ceramics International*, vol. 39, no. 3, pp. 2981–2987, 2013. [Online]. Available: https://doi.org/10.1016/j.ceramint.2012.09.075

[54] S. Ke, X. Cheng, Q. Wang, Y. Wang, and Z. Pan, "Preparation of a photocatalytic $TiO_2/ZnTiO_3$ coating on glazed ceramic tiles," *Ceramics International*, vol. 40, no. 6, pp. 8891–8895, 2014. [Online]. Available: https://doi.org/10.1016/j.ceramint.2014.01.027

[55] V. Petrovič, V. Ducman, and S. D. Škapin, "Determination of the photocatalytic efficiency of TiO_2 coatings on ceramic tiles

by monitoring the photodegradation of organic dyes,” *Ceramics International*, vol. 38, no. 2, pp. 1611–1616, 2012. [Online]. Available: https://doi.org/10.1016/j.ceramint.2011.09.050

[56] P. Sooksaen, N. Saowaros, K. Ngamkaruhasereethorn, and A. Pringkasemchai, “Photocatalytic degradation study of titania sol-gel coated on commercial unglazed ceramic tiles,” *Key Engineering Materials*, vol. 751, pp. 819–824, 2017. [Online]. Available: https://doi.org/10.4028/www.scientific.net/KEM.751.819

[57] V. B. Tezza, M. Scarpato, L. F. S. Oliveira, and A. M. Bernardin, “Effect of firing temperature on the photocatalytic activity of anatase ceramic glazes,” *Powder Technology*, vol. 276, pp. 60–65, 2015. [Online]. Available: https://doi.org/10.1016/j.powtec.2015.01.076

[58] R. Taurino, L. Barbieri, and F. Bondioli, “Surface properties of new green building material after tio_2sio_2 coatings deposition,” *Ceramics International*, vol. 42, no. 4, pp. 4866–4874, 2016. [Online]. Available: https://doi.org/10.1016/j.ceramint.2015.12.002

[59] M. Nevárez-Martínez, P. Espinoza-Montero, F. Quiroz-Chávez, and B. Ohtani, “Fotocatálisis: inicio, actualidad y perspectivas a través del tio_2,” *Avances en Química*, vol. 12, no. 2–3, pp. 45–59, 2018. [Online]. Available: https://goo.gl/FtiWUw

[60] L. Liao, S. Heylen, S. P. Sree, B. Vallaey, M. Keulemans, S. Lenaerts, M. B. Roeffaers, and J. A. Martens, “Photocatalysis assisted simultaneous carbon oxidation and no_x reduction,” *Applied Catalysis B: Environmental*, vol. 202, pp. 381–387, 2017. [Online]. Available: https://doi.org/10.1016/j.apcatb.2016.09.042

[61] Y. Boyjoo, H. Sun, J. Liu, V. K. Pareek, and S. Wang, “A review on photocatalysis for air treatment: From catalyst development to reactor design,” *Chemical Engineering Journal*, vol. 310, pp. 537–559, 2017. [Online]. Available: https://doi.org/10.1016/j.cej.2016.06.090

[62] S. Q. Sun, B. Sun, W. Zhang, and D. Wang, “Preparation and antibacterial activity of ag-tio_2 composite film by liquid phase deposition (lpd) method,” *Bulletin of Materials Science*, vol. 31, no. 1, pp. 61–66, Feb 2008. [Online]. Available: https://doi.org/10.1007/s12034-008-0011-7

[63] F. Tana, M. Messori, D. Contini, A. Cigada, T. Valente, F. Variola, L. D. Nardo, and F. Bondioli, “Synthesis and characterization of scratch-resistant hybrid coatings based on non-hydrolytic sol-gel zro_2 nanoparticles,” *Progress in Organic Coatings*, vol. 103, pp. 60–68, 2017. [Online]. Available: https://doi.org/10.1016/j.porgcoat.2016.11.022

Scientific Paper / Artículo Científico

UNIVERSIDAD POLITÉCNICA SALESIANA ECUADOR
INGENIUS
Revista de Ciencia y Tecnología
https://doi.org/10.17163/ings.n21.2019.02
pISSN: 1390-650X / eISSN: 1390-860X

PHOTOVOLTAIC SIMULATION CONSIDERING BUILDING INTEGRATION PARAMETERS

SIMULACIÓN FOTOVOLTAICA CONSIDERANDO PARÁMETROS DE INTEGRACIÓN EN EDIFICACIONES

Ismael F. Izquierdo-Torres[1,*], Mario G. Pacheco-Portilla[1],
Luis G. González-Morales[2], Esteban F. Zalamea-León[3]

Abstract

This research calibrates and validates a model for monocrystalline photovoltaic systems in SAM (System Advisor Model) for power generation simulation, considering the meteorological characteristics of Cuenca, Ecuador, close to the equatorial line. The electrical performance is calculated by arranging photovoltaic systems with specific characteristics, with inclinations that respond to conventional local roofing and different orientations. Efficiency is calculated with *in situ* measurements over a period of 18 days. Meteorological data were used to calibrate a weather file for the year 2016. Annual yields are estimated according to inclination and orientation, and technical characteristics of the photovoltaic system. Losses are detected due to dirt accumulation and increase in temperature of the panels. The model is validated by linear regression, by comparing the simulated values with the data obtained from *in situ* measurements of a reference panel deployed horizontally. The results show an average efficiency loss of 2.77% for dirt conditions and up to 30% for temperature increases.

Resumen

Esta investigación calibra y valida un modelo de sistemas fotovoltaicos monocristalinos en la herramienta computacional System Advisor Model (SAM) para simulación de generación eléctrica, considerando las características meteorológicas en Cuenca (Ecuador), ciudad en altura próxima a la línea ecuatorial. Se obtiene el rendimiento eléctrico al desplegarse paneles fotovoltaicos de características específicas, con inclinaciones que responden a techumbres típicas locales y distintas orientaciones. Se calcula la eficiencia con mediciones *in situ* durante un período de 18 días, para que, con datos meteorológicos se calibre un archivo climático para el año 2016. Se estiman rendimientos anuales acorde a inclinación y orientación, y a características técnicas de los fotovoltaicos. Se detectan pérdidas por acumulación de suciedad e incremento de temperatura de las placas. Se valida el modelo mediante una regresión lineal, al comparar los valores simulados con los datos obtenidos de mediciones *in situ* de un panel en posición horizontal. Los resultados indican una pérdida promedio de eficiencia de 2,77 % por condiciones de suciedad y de hasta el 30 % por incremento de temperatura.

[1,*] Faculty of Chemical Sciences, Universidad de Cuenca, Ecuador. Corresponding author ✉:
ismael.izquierdo.torres@ucuenca.edu.ec, http://orcid.org/0000-0003-0728-8978,
http://orcid.org/0000-0003-4107-4594

[2] Department of Electrical, Electronics and Telecommunication Engineering, Universidad de Cuenca, Ecuador.
http://orcid.org/0000-0001-9992-3494

[3] Faculty of Architecture and Urbanisms, Universidad de Cuenca, Ecuador. http://orcid.org/0000-0001-5551-5026

Received: 06-07-2018, accepted after review: 05-11-2018

Suggested citation: Izquierdo-Torres, I. F.; Pacheco-Portilla, M. G; González-Morales, L. G. and Zalamea-León, E. F. (2019). «Photovoltaic simulation considering building integration parameters». INGENIUS. N.°21, (january-june). pp. 21-31. DOI: https://doi.org/10.17163/ings.n21.2019.02.

The validation of the model showed a determination coefficient R^2=0.996 and a normalized Root Mean Square Error (RMSE) of 8.16%. It is concluded that because of the particular latitude of the study site, unlike most of the planet, the provision of photovoltaic panels in any orientation considering low slopes does not significantly reduce the annual power generation performance.

Keywords: Monocrystalline, Photovoltaic Simulation, SAM, Renewable Energies

La validación del modelo mostró un coeficiente de determinación $R^2 = 0{,}996$ y un RMSE normalizado de 8,16 %. Se concluye además que, por la latitud particular del sitio en estudio, a diferencia de la mayor parte del planeta, la disposición de paneles fotovoltaicos en cualquier orientación considerando pendientes bajas, no reduce significativamente el rendimiento en la generación de energía eléctrica anual.

Palabras clave: energías renovables, monocristalino, SAM, simulación fotovoltaica.

1. Introduction

The increasing energy demand and the anthropogenic processes that cause the climatic change have made necessary to consider alternative sources of energy which are clean, renewable and of lower impact expansion potential [1]. In addition, it is also an ideal condition that they can be deployed in buildings and urban environments [2,3]. The photovoltaic (PV) solar technology is undoubtedly one of the main alternatives to face the global energy problematic, due to its existent potential for expansion and more convenient costs [4, 5].

Due to its geographic location, Ecuador is at a latitude with important solar potential [6, 7]. Ecuador is a developing country with increasing energy consumption and mostly invariant seasonality along the year [8, 9]. As a consequence, there exist relatively constant high levels of insolation [10] that provide a high potential for utilizing solar energy as an alternative for effectively reducing atmospheric contaminants and the global effects of climatic change [11–13].

Nevertheless, since each city has particular characteristics regarding resources and energy demand [11], [14], it is necessary to determine the variable potential for energy generation in every urban environment, prior to establishing urban [15] and infrastructure [16] regulations. The International Renewable Energy Agency (IRENA) suggests taking advantage of vast building surroundings and roof areas to locate energy capture systems as a complement to energetic efficiency measures in buildings, and for implementing distributed energy production schemes [12].

Some aspects with urban impact must be considered in the case of photovoltaic or thermal solar technologies. For instance, capture surfaces should be placed coplanar in the building, taking part of the architectural surroundings [17]. In addition, they should be deployed according to the consumption of each building [18].

There are currently being developed architectural constructive elements, such as cover slabs, glasses, solar filters and even tiles, which are photovoltaic (PV) panels, i.e. they have energy generation capacity. These elements preserve the geometry and take part of the surroundings, thus satisfying the concept of architectural integration [PV Building Integrated Photovoltaics (BIPV)] [19–21].

This work is intended to determine the electrical efficiency of PV monocrystalline solar panels as a function of the inclination and orientation, in order to provide a methodological foundation for the development of a model for predicting the performance of other PV technologies suitable for adaptation or integration to the building surroundings; this requires measuring the performance for different orientations and inclinations.

There are not clearly established criteria regarding optimal inclination and orientation of PV panels for cities such as Cuenca, and any inclination close to the horizontal and oriented opposite to its latitude is considered appropriate [22]. However, this empirical guideline does not take into account aspects such as the coplanar adaptation to the buildings, and the losses due to accumulation of dirt, which may vary between 5% [23] and 35% [24] and affect the performance of the system.

Besides the aforementioned issues, the surface temperature of the PV modules also affect the overall system efficiency in PV facilities [25–28]. In addition, it is necessary to consider economic aspects and energy demand, in order to maximize the production during periods of higher demand or cost [29].

This study proposes a methodology to build a simulation model in the software SAM (System Advisor Model) [30], to estimate the production of electricity of PV monocrystalline panels. The model is calibrated considering the impact of factors such as orientation, inclination, and efficiency losses due to the accumulation of dirt and temperature increments. The model and the corresponding climatic file are implemented in SAM. The resulting model is valid for simulating real values of production [31] and determining the PV performance, without requiring *in situ* measurements along periods of one year or longer, and preventing the use of models with more uncertainty and which are not freely available to the user. In this manner, the methodology for model calibration can be replicated in other locations.

2. Materials and methods

This study is focused in calibrating and validating a simulation model of a monocrystalline PV system, using short periods of *in situ* measurements. In addition, a local climatic file in readable format (SAM CSV) is generated by the software SAM. Performance losses due to parameters such as accumulation of dirt and increments of temperature as a function of weather and global irradiance, are also considered.

The *in situ* measurements were carried out during December 2016 and January 2017. Three monocrystalline PV panels were installed next to a meteorological station located at (-2.901691°S, -79.010151° E). Each panel has a nominal power of 100 W, 36 cells and dimensions 0.54 m wide and 1.2 m long (Figure 1), and is electrically connected to the HIOKI PW 3337-03 measurement equipment and to variable load resistances, which were adjusted between 1 and 100 Ω in order to obtain the maximum power (Figure 2) for a specific irradiance. Data of DC voltage, current and power were collected, with a sampling period of five minutes, which were further converted to hourly intervals.

In particular, the measurements were taken according to the inclination and orientation of the panels, along 12 days of December 2016 between the hours of 7:30 and 17:00. Data were obtained from the horizontal panel and panels with inclinations 14.00°, 18.26° and 26.56° (with all orientations: N, S, E, W), to validate the model in SAM. These inclinations correspond to typical roof pitches in low-rise buildings and residential housings in the city of Cuenca [32]. The methodology shown in Table 1 was used for measuring performance according to inclination and orientation.

Figure 1. Monocrystalline solar panels with different inclinations

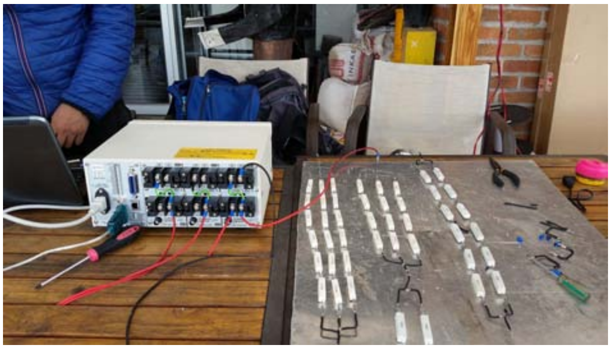

Figure 2. HIOKI PW 3337-03 equipment and load resistors

Then, the efficiency was calculated as:

$$\eta = \frac{P}{E \times Ac} \times 100 \quad (1)$$

where η is the efficiency of the panels, P is the output power, E is the irradiance of the sun, and Ac is the capture area or area of the panel. For each orientation, the inclination which resulted in the best performance (among the three proposed) was chosen, and additional measurements were taken along three days of January 2017 to determine the optimal configuration (both inclination and orientation) for this time of the year, according to the methodology shown in Table 2.

Table 1. Parametric variation for measuring the performance of monocrystalline panels according to their inclination and orientation

East			
Day	Panel 1	Panel 2	Panel 3
1	0°	14,00°	18,26°
2	0°	18,26°	26,56°
3	0°	26,56°	14,00°
South			
Day	Panel 1	Panel 2	Panel 3
4	0°	14,00°	18,26°
5	0°	18,26°	26,56°
6	0°	26,56°	14,00°
West			
Day	Panel 1	Panel 2	Panel 3
7	0°	14,00°	18,26°
8	0°	18,26°	26,56°
9	0°	26,56°	14,00°
North			
Day	Panel 1	Panel 2	Panel 3
10	0°	14,00°	18,26°
11	0°	18,26°	26,56°
12	0°	26,56°	14,00°

Table 2. Optimal configuration of monocrystalline panels for January 2017

Day	**Panel 1**	**Panel 2**	**Panel 3**
1	S 26,56°	E 14,00°	N 18,26°
2	S 26,56°	N 18,26°	W 18,26°
3	S 26,56°	W 18,26°	E 14,00°

Of the four analyzed configurations, the optimal was selected based on the average energy production during the days of measurement.

On the other hand, to estimate the energy losses due to accumulation of dirt, weekly measurements of the performance of the PV panel were carried out, from January 11th to February 1st 2017, using the optimal inclination and orientation. In this case, one of the panels was used for control purposes and was cleaned during the days of measurement, while the two remaining panels did not have any intervention; however, since precipitation events are frequent in Cuenca, the panels that did not receive any manual maintenance showed changes on the surface since such events cleaned them. It is necessary to consider that rainfall is high locally, with precipitations all year long such that no rain periods of more than one month are unusual [33].

In order to estimate the losses due to increments of temperature, the output power and the temperature on the surface of the monocrystalline panels were measured. Then, the efficiency was calculated by means of equation (1) using the irradiance data obtained from the meteorological station, and average values of efficiency losses were established by irradiance ranges. Then, the model was calibrated in SAM using data of average performance losses due to accumulation of dirt; the data was organized by irradiance ranges. The information was obtained from in situ measurements, and consisted of a climatic file generated during 2016, with hourly values of direct, diffuse and global radiation (all given in W/m^2), relative humidity (%), zenithal angle (°), precipitation (mm), wind direction and velocity (° and m/s, respectively). Thus, the climatic file of the site under study is not obtained by interpolating values of climatic variables between two locations, which results in greater degree of uncertainty in the predictions of the models, but by contrast results are validated through a real comparison between measurements of PV production and instantaneously detected climatic conditions.

In addition, technical data (in Table 3) of the utilized PV panels was incorporated to the software.

Table 3. Specifications of the simulated PV panel

Specifications			
Tipe of cell	Monocrystalline Silicium	Voc	21,6 V
Area of the module	0,645 m^2	Coefficient Voc Temperature	-0,38 %/°C
NOCT	46 °C	Coefficient Isc Temperature	0,1%/ °C
Vmp	17,3 V	Coefficient MPP Temperature	-0,41 %/°C
Imp	5,78 A	Number of cells in serie	36

Since this study defines aspects related to energy processing, the point of maximum power of the panel was considered in each estimation. The losses of the system were established based on *in situ* efficiency measures for irradiance intervals of 200 W/m^2 and for losses due to accumulation of dirt; for calculation purposes a base loss of 5% is established in the program by defect. With the simulated data of performance, a database was generated with values similar to the in situ measurements, and the following metrics were calculated: Determination coefficient R^2 (equation 2), root of the mean squared error (RMSE) (equation 3), mean bias error (MBE) (equation 4); at last, the 90% confidence interval was established (CI 90%) (equation 5), for time intervals suggested by some validation studies in SAM [34, 35], for this period of the year. The values of RMSE and MBE were normalized with respect to the maximum value among the *in situ* measurements.

$$R^2 = \frac{\sum_i^N (SAM_i - Measured_{avg})^2}{\sum_i^N (SAM_i - SAM_{avg})^2} \tag{2}$$

$$RMSE = \sqrt{\frac{\sum_i^N (SAM_i - Measured_i)^2}{N}} \tag{3}$$

$$MBE = \frac{\sum_i^N (SAM_i - Measured_i)^2}{N} \tag{4}$$

$$IC_{90\%} = 1.645 \times [Std(SAM_i - Measured_i)] \tag{5}$$

3. Results and discussion

After using the parameter variation for measuring the performance and calculating the efficiency in December, the results shown in Table 4 were obtained.

Table 4. Best inclination per orientation

Orientation	Best inclination
East	14,00°
South	26,56°
West	18,26°
North	18,26°

The results in Table 4 are due to the position of the sun this time of the year (close to the solstice), for which the south orientation is greater than the north orientation in any inclination; however, the east orientation of 14° results in a greater efficiency due to mornings of high irradiance and cloudy afternoons, and thus was selected for further analysis of the influence of dirt.

In this analysis, during the first week of measurements there were no performance losses due to the amount of weekly accumulated rainfall (41.8 mm); during the second week of monitoring there was a total rainfall of 6 mm, which resulted in dirt spots on the surface and a little significant reduction in the efficiency of the panels (0.7 %).

Since in the third week there were no rain events, the presence of material on the surface of the panels was evident; as a consequence, the corresponding measurements exhibited an average efficiency reduction of 2.77%, with a maximum of 3.68% and a minimum of 1.87%. A week later, the accumulated rainfall (13.4 mm) removed a significant amount of particles from the surface, thus resulting in negligible losses. Since this average value of efficiency loss was very small, the predefined value of 5 % was used for the simulation in SAM. As it was stated before, in this place long no rain periods are seldom, as it is for high Andean cities.

From the generated data it was possible to establish a comparative criterion for calibrating and validating the model in SAM, based on the parameters specified in the methodology. The results estimated by the model were compared with the horizontal panel *in situ* measurements, thus obtaining the statistical data shown in Table 5.

Table 5. Calculated metrics

Metric	Value	Unit
R^2	0,996	-
RMSE	5,263	W
NRMSE	8,156	%
MBE	-1,04	W
NMBE	-1,616	%
IC 90 %	8,522	%

The *in situ* and simulated data are compared graphically in Figure 3. There is an evident strong linear correlation, as confirmed by the calculated value of the R^2 coefficient. The RMSE and NRMSE values, which indicate the error of the data estimated by the model compared to the real measurements, are very acceptable in this case [36].

The MBE and its normalized value are employed to determine the model underestimation or overestimation; it was found that the model underestimates the system performance by 1.61%. Figure 4 shows the real behavior of the system and the estimated by the model in SAM for 12 days of measurement, considering as reference short-period validations carried out in TRNSYS by [36, 37], where the maximum generation values show a trend; a slight underestimation by the model could be observed. In addition, previous studies analyze the temporal resolution with intervals smaller than one hour [38], and compare simulated and *in situ* values for a two-day period [39].

The 90% CI (confidence interval) in Table 5 indicates that 90% of the simulated values are within ± 8.522% of the *in situ* measured values, which is really close to the ± 8% that has been obtained in the validation of seven baseline studies with SAM [34]. It is important to remark that this value is smaller in an annual simulation, exhibiting a better fit of the linear model and more validity.

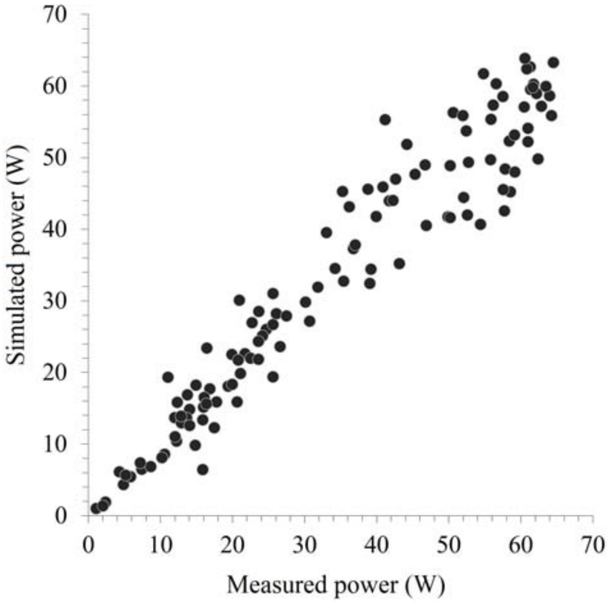

Figure 3. Scatter plot of measured vs. simulated power

In addition, the estimated values of temperature of the PV cells are different than the *in situ* measurements. Therefore, the average annual temperature from the model database was used instead for comparison purposes, since for the same levels of radiation the temperature seems to behave in a similar manner along the year, as opposed to the *in situ* measurements which are one-time values registered at the particular day of measurement. An important average difference of 13.33 °C can be observed in the data shown in Table 6, where the cells with no values indicate that during that day the radiation levels were not within those intervals. It is also assumed that the difference may be greater, since the model estimates the temperature of the cells, while the measurements were taken on the panel glass which is lower than the surface temperature of the cells [40]. This temperature variation can be also due to the intensity of the UV rays, since it is a high location [41]. Thus, it is recommended that measurements are taken in the lab to confirm the increment in the surface temperature of the cells.

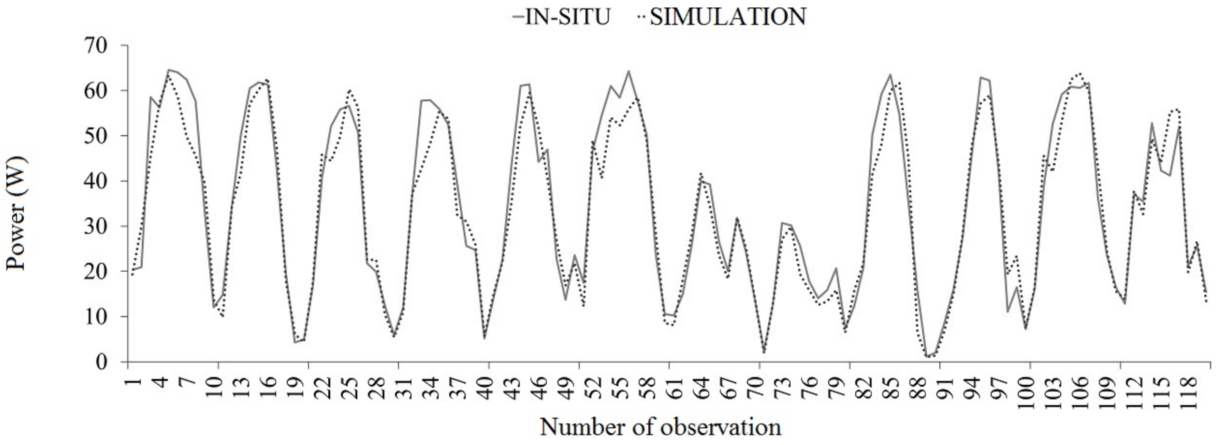

Figure 4. Performance comparison

Table 6. Comparison of the simulated and measured temperature

Irradiance (W/m^2)	Anual average temperature (°C)	Measured temperature (°C)
0-200	15,81	-
200-400	21,05	33,5
400-600	24,56	-
600-800	27,02	40
800-1000	30,33	43
1000-1200	34,08	49,33

Based on the values of these metrics, it was determined that the model is valid, and thus can be used to estimate the production of energy along longer periods, having available the climatic file. The values of performance in Table 7 were obtained after carrying out a simulation for one year (expressed in kWh/year) for a 100 W module, considering orientation and inclination parameters.

Thus, the horizontal is the configuration with the greater generation. However, such configuration cannot be deployed in inclined roofs and, in addition, it is does not take advantage of the cleaning due to the rainfall.

Table 7. Annual production of energy (kWh/year)

Angle	North	South	East	West
0°	119,16			
14°	116,5	116,94	117,21	116,24
18,26°	114,66	115,24	115,63	114,35
26,6°	109,76	110,64	111,35	109,5

An interesting distinctive feature is established in Table 7 with respect to the orientation and slope of the PV in the context of this study. The horizontal configuration effectively yields the maximum production, but it only exceeds by 8.8% the annual generation of the minimum production obtained in this work (West orientation with an inclination of 26.56°). Therefore, due to the aforementioned limitations, the horizontal layout is not recommended. In the comparison of the performance for the inclined and oriented cases, it was observed that a smaller slope effectively yields a better average production, 5.8% higher for the case of 14° with respect to the 26.56° case, and 4.2% more for 18° compared to 26.56°. Analyzing the one-time performances, the maximum production was obtained for the East orientation with 14°, and the minimum for the West orientation with 26.56°, with the former more efficient by 7 %. The losses measured in this study are smaller, considering for instance the PV performance estimations for a condition of moderate seasonal weather (36° of latitude), in which a deviation of 90° with respect to the optimal orientation results in a 17% reduction of the performance [42]. As expected, greater deviations opposite to the solar path and latitudes more distant to the Equator, should result in larger reductions in the PV performance. The better performance for the case of East orientation is because of morning with less clouds.

A more significant difference can be observed in monthly values, which vary between 7.33 kWh/month for July (month with minimum irradiance) and 12.19 kWh/month for November (month with maximum irradiance) (Figure 5). This is an indication of a uniform production along the year in this location, as opposed to PV supply studies carried out in moderate seasonal weather (38° south latitude) in which the generation during the summer months can be the triple of that for the winter months [43]; and in strong seasonal weather, such as Helsinki (Finland), in extreme latitude (60° north latitude), where the summer production can be more than ten times the winter production. This represents an obvious advantage of the equatorial zones, since it is more adaptable to face urban demands.

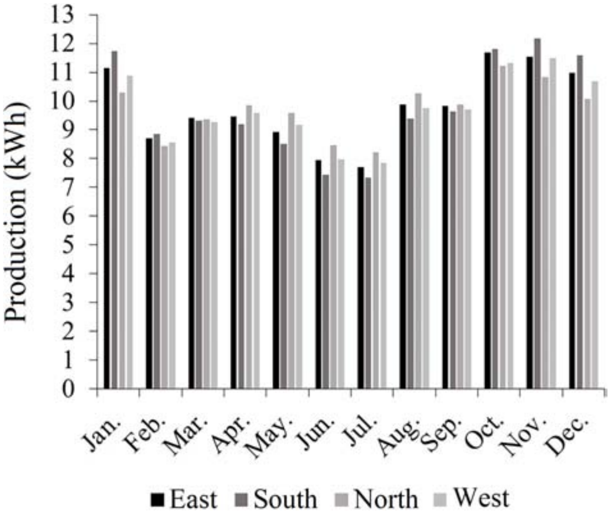

Figure 5. Estimated monthly production by simulation in SAM

4. Conclusions

An important step towards exploiting the potential of a particular city to generate renewable energy, is to validate tools that can be used to reduce the estimation and simulation uncertainties, of PV production in this case. This study showed that, by means of specific adjustments in different parameters, the SAM model can be used with low uncertainty in the city of Cuenca (Ecuador), this providing a reliable model for forecasting a possible PV electric generation. For other locations a similar calibration can be carried out, validating the model with *in situ* performance measurements.

Among the results of the study, the efficiency loss due to accumulation of dirt was measured, obtaining an average of 2.77%, which is not significant and indicate that a recurrent cleaning of the PV panels is not necessary, since the continuous rainfalls are enough to recover the efficiency. On the other hand, losses due to the temperature are important for high irradiance, which might be due to the constructive features of the cells or to elevated indices of UV rays. This became a relevant parameter during model calibration.

The estimation performance of the model was evaluated using statistical metrics, to compare the model estimates with in situ measurements. The values obtained were $R^2 = 0{,}996$, NRMSE = 8,156 y NMBE = -1,616%, which demonstrate that although the model underestimated such measurements, it is appropriate for forecasting future scenarios in annual simulations, since it exhibits a strong linear trend with respect to the *in situ* measurements. A methodology and a validated tool were delivered, which are useful for estimating the electric generation employing monocrystalline solar panels.

Regarding performances detected in the particular location, a higher annual generation can be obtained facing the PV systems to the East with a slope inclination close to the horizontal. However, no significant differences were found with respect to other orientations with similar inclinations, due to the geographic location of the area under study which results in mainly uniform levels of irradiance along the year. Likewise, although it was observed that, depending on inclination and orientation, the expected production during June-July (minimum irradiance) is 40% less than the production of November (maximum irradiance), the annual production is significantly more stable as compared to other latitudes. This results in an excellent potential of connection to a smart grid under a distributed generation scheme, or storage for self-supply.

References

[1] Z. A. Elum and A. S. Momodu, "Climate change mitigation and renewable energy for sustainable development in Nigeria: A discourse approach," *Renewable and Sustainable Energy Reviews*, vol. 76, pp. 72–80, 2017. [Online]. Available: https://doi.org/10.1016/j.rser.2017.03.040

[2] A. Grubler, X. Bai, T. Buettner, S. Dhakal, D. J. Fisk, T. Ichinose, J. E. Keirstead, G. Sammmer, D. Satterthwaite, N. B. Schulz *et al.*, *Global Energy Assessment - Toward a Sustainable Future*. International Institute for Applied Systems Analysis and Cambridge University., 2012, ch. Urban energy systems, pp. 1307–1400. [Online]. Available: https://goo.gl/rVdsU6

[3] A. Barragán-Escandón, J. Terrados-Cepeda, and E. Zalamea-León, "The role of renewable energy in the promotion of circular urban metabolism," *Sustainability*, vol. 9, no. 12, 2017. [Online]. Available: https://doi.org/10.3390/su9122341

[4] A. K. Shukla, K. Sudhakar, P. Baredar, and R. Mamat, "Solar PV and BIPV system: Barrier, challenges and policy recommendation in India," *Renewable and Sustainable Energy Reviews*, vol. 82, pp. 3314–3322, 2018. [Online]. Available: https://doi.org/10.1016/j.rser.2017.10.013

[5] J. Byrne, J. Taminiau, J. Seo, J. Lee, and S. Shin, "Are solar cities feasible? a review of current research," *International Journal of Urban Sciences*, vol. 21, no. 3, pp. 239–256, 2017. [Online]. Available: https://doi.org/10.1080/12265934.2017.1331750

[6] M. Nadim, M. R. H. Rashed, A. Muhury, and S. M. Mominuzzaman, "Estimation of optimum tilt angle for PV cell: A study in perspective of

bangladesh," in *2016 9th International Conference on Electrical and Computer Engineering (ICECE)*, Dec 2016, pp. 271–274. [Online]. Available: https://doi.org/10.1109/ICECE.2016.7853908

[7] P. Fitriaty and Z. Shen, "Predicting energy generation from residential building attached Photovoltaic Cells in a tropical area using 3D modeling analysis," *Journal of Cleaner Production*, vol. 195, pp. 1422–1436, 2018. [Online]. Available: https://doi.org/10.1016/j.jclepro.2018.02.133

[8] B. Trewin, *State of the tropics*. James Cook University, 2014, ch. The climates of the Tropics, and how they are changing, pp. 39–51. [Online]. Available: https://goo.gl/hH8pv1

[9] A. Bykerk-Kauffman. (2018) Seasons and why the equator is warmer than the poles. Pedagogy in Action the SERC portal for Educators. Science Education Resource Center. [Online]. Available: https://goo.gl/vsDCFB

[10] IRENA, *Global Atlas for Renewable Energy: A World of Renewables*. International Renewable Energy Agency, 2015. [Online]. Available: https://goo.gl/adpQop

[11] M. M. Riyahi Alam, A. Behfar, and R. Shahmoradi, "Potential application of solar power systems for residential buildings in high-density urban pattern: The case of the Eixample district, city of the Barcelona, in Spain," *Recent Researches in Environmental and Geological Sciences*, pp. 342–347, 2012. [Online]. Available: https://goo.gl/t6dSQZ

[12] IRENA, *Renewable Energy in Cities*. International Renewable Energy Agency, Abu Dhabi,, 2016. [Online]. Available: https://goo.gl/EN2Ufq

[13] T. Razykov, C. Ferekides, D. Morel, E. Stefanakos, H. Ullal, and H. Upadhyaya, "Solar photovoltaic electricity: Current status and future prospects," *Solar Energy*, vol. 85, no. 8, pp. 1580–1608, 2011. [Online]. Available: https://doi.org/10.1016/j.solener.2010.12.002

[14] A. Barragán-Escandón, J. Terrados-Cepeda, E. Zalamea-León, and P. Arias-Reyes, "Electricity production using renewable resources in urban centres," *Proceedings of the Institution of Civil Engineers - Energy*, vol. 171, no. 1, pp. 12–25, 2018. [Online]. Available: https://doi.org/10.1680/jener.17.00003

[15] A. Curreli, G. Serra-Coch, A. Isalgue, I. Crespo, and H. Coch, "Solar energy as a form giver for future cities," *Energies*, vol. 9, no. 7, 2016. [Online]. Available: https://doi.org/10.3390/en9070544

[16] P. Chen, R. Salcedo, Q. Zhu, F. de Leon, D. Czarkowski, Z. Jiang, V. Spitsa, Z. Zabar, and R. E. Uosef, "Analysis of voltage profile problems due to the penetration of distributed generation in low-voltage secondary distribution networks," *IEEE Transactions on Power Delivery*, vol. 27, no. 4, pp. 2020–2028, Oct 2012. [Online]. Available: https://doi.org/10.1109/TPWRD.2012.2209684

[17] M. Wall, M. C. M. Probst, C. Roecker, M.-C. Dubois, M. Horvat, O. B. Jørgensen, and K. Kappel, "Achieving solar energy in architecture-IEA SHC Task 41," *Energy Procedia*, vol. 30, pp. 1250–1260, 2012. [Online]. Available: https://doi.org/10.1016/j.egypro.2012.11.138

[18] K. Farkas, F. Frontini, L. Maturi, A. Scognamiglio, M. C. Munari Probst, and C. Roecker, *Designing photovoltaic systems for architectural integration. Criteria and guidelines for product and system developers*, Solar Heating & Cooling Programme- International Energy Agency, 2013. [Online]. Available: https://goo.gl/fj36VW

[19] B. P. Jelle, "Building integrated photovoltaics: A concise description of the current state of the art and possible research pathways," *Energies*, vol. 9, no. 1, 2016. [Online]. Available: https://doi.org/10.3390/en9010021

[20] M. C. Munari Probst, C. Roecker, F. Frontini, A. Scognamiglio, K. Farkas, L. Maturi, and I. Zanetti, "Solar energy systems in architecture - integration criteria and guidelines," *Infoscience EPFL scientific publications*, p. 214, 2013, report of International Energy Agency Solar Heating and Cooling Programme Task 41 Solar Energy & Architecture. [Online]. Available: https://goo.gl/4Rx7e5

[21] Eletrek. (2018) Tesla solar roof. [Online]. Available: https://goo.gl/Bnyduv

[22] A. Gharakhani Siraki and P. Pillay, "Comparison of PV system design software packages for urban applications," in *Word Energy Congress Montreal*, 2010. [Online]. Available: https://goo.gl/Vhuhyg

[23] G. Cáceres, S. Nasirov, H. Zhang, and G. Araya-Letelier, "Residential solar PV planning in Santiago, Chile: Incorporating the PM10 parameter," *Sustainability*, vol. 7, no. 1, pp. 722–440, 2015. [Online]. Available: https://doi.org/10.3390/su7010422

[24] S. C. S. Costa, A. S. A. C. Diniz, and L. L. Kazmerski, "Dust and soiling issues and impacts relating to solar energy systems: Literature review update for 2012–2015," *Renewable and Sustainable Energy Reviews*,

vol. 63, pp. 33–61, 2016. [Online]. Available: https://doi.org/10.1016/j.rser.2016.04.059

[25] B. V. Chikate and Y. Sadawarte, "The factors affecting the performance of solar cell," *International Journal of Computer Applications (0975-8887)*, 2015. [Online]. Available: https://goo.gl/d7txov

[26] M. E. Meral and F. Dinçer, "A review of the factors affecting operation and efficiency of photovoltaic based electricity generation systems," *Renewable and Sustainable Energy Reviews*, vol. 15, no. 5, pp. 2176–2184, 2011. [Online]. Available: https://doi.org/10.1016/j.rser.2011.01.010

[27] Y. Jia-Ying, D. Kun, T. Reindl, and A. G. Aberle, "Outdoor PV module performance under fluctuating irradiance conditions in tropical climates," *Energy Procedia*, vol. 33, pp. 238–247, 2013. [Online]. Available: https://doi.org/10.1016/j.egypro.2013.05.064

[28] A. Luque and S. Hegedus, *Handbook of photovoltaic science and engineering.* John Wiley & Sons, 2011. [Online]. Available: https://goo.gl/7D9UYk

[29] C. Hachem, A. Athienitis, and P. Fazio, "Parametric investigation of geometric form effects on solar potential of housing units," *Solar Energy*, vol. 85, no. 9, pp. 1864–1877, 2011. [Online]. Available: https://doi.org/10.1016/j.solener.2011.04.027

[30] NREL. (2017) System Advisor Model (SAM). National Renewable Energy Laboratory. [Online]. Available: https://goo.gl/WTktPn

[31] J. Freeman, J. Whitmore, N. Blair, and A. P. Dobos, "Validation of multiple tools for flat plate photovoltaic modeling against measured data," in *2014 IEEE 40th Photovoltaic Specialist Conference (PVSC)*, June 2014, pp. 1932–1937. [Online]. Available: https://doi.org/10.1109/PVSC.2014.6925304

[32] I. F. Izquierdo Torres and M. G. Pacheco Portilla, *Evaluación de la eficiencia de paneles solares como sistema de captación de energía para edificaciones del área urbana de Cuenca*, E. Universidad de Cuenca, Ed. Tesis de grado, 2017. [Online]. Available: https://goo.gl/wSEZ1X

[33] CLIMATE-DATA. (2017) Clima Cuenca. climate-data.org. [Online]. Available: https://goo.gl/SBnaa2

[34] J. Freeman, J. Whitmore, L. Kaffine, and A. P. Blair, Nate Dobos, "System Advisor Model: Flat plate photovoltaic performance modeling validation report," National Renewable Energy Laboratory (NREL), Tech. Rep., 2013. [Online]. Available: https://goo.gl/47cQ1r

[35] E. Rudié, A. Thornton, N. Rajendra, and S. Kerrigan, "System Advisor Model performance modeling validation report: Analysis of 100 sites," Locus Energy, National Renewable Energy Laboratory (NREL), Tech. Rep., 2014. [Online]. Available: https://goo.gl/zpfUZA

[36] D. F. Al Riza, S. Gilani, and M. Aris, "Measurement and simulation of standalone solar PV system for residential lighting in Malaysia," *Journal of Hydrocarbons Mines and Environmental Research*, vol. 2, no. 1, pp. 6–12, 2011. [Online]. Available: https://goo.gl/G8shmj

[37] K. Kanyarusoke, J. Gryzagoridis, and G. Oliver, "Validation of TRNSYS modelling for a fixed slope photovoltaic panel," *Turkish Journal of Electrical Engineering & Computer Sciences*, vol. 24, no. 6, pp. 4763–4772, 2016. [Online]. Available: https://www.doi.org/10.3906/elk-1502-38

[38] M. A. Meybodi, L. R. Santigosa, and A. C. Beath, "A study on the impact of time resolution in solar data on the performance modelling of CSP plants," *Renewable Energy*, vol. 109, pp. 551–563, 2017. [Online]. Available: https://doi.org/10.1016/j.renene.2017.03.024

[39] V. Håvard Breisnes, "Modelling of photovoltaic modules with battery energy storage in Simulink/MATLAB: With in-situ measurement comparisons," Master's thesis, Norwegian University of Science and Technology, 2014. [Online]. Available: https://goo.gl/13bxEy

[40] F. Chenlo Romero, "Cálculo de la temperatura de operación de células solares en un panel fotovoltaico plano," Centro de Investigaciones Energéticas, Medioambientales y Tecnológicas (CIEMAT). Madrid - España, Tech. Rep., 2002. [Online]. Available: https://goo.gl/SFrX4r

[41] M. Blumthaler, W. Ambach, and R. Ellinger, "Increase in solar UV radiation with altitude," *Journal of Photochemistry and Photobiology B: Biology*, vol. 39, no. 2, pp. 130–134, 1997. [Online]. Available: https://doi.org/10.1016/S1011-1344(96)00018-8

[42] E. F. Zalamea-León and R. H. García-Alvarado, "Integración de captación activa y pasiva en viviendas unifamiliares de emprendimientos inmobiliarios," *Ambiente Construído*, vol. 18, no. 1, pp. 445–461, 2018. [Online]. Available: https://dx.doi.org/10.1590/s1678-86212018000100231

[43] E. Zalamea and R. García Alvarado, "Roof characteristics for integrated solar collection in dwellings of Real-Estate developments in Concepcion, Chile," *Revista de la construcción*, vol. 13, no. 3, pp. 36–44, 12 2014. [Online]. Available: https://dx.doi.org/10.4067/S0718-915X2014000300005

Scientific Paper / Artículo Científico

UNIVERSIDAD POLITÉCNICA SALESIANA ECUADOR
INGENIUS
Revista de Ciencia y Tecnología
https://doi.org/10.17163/ings.n21.2019.03
pISSN: 1390-650X / eISSN: 1390-860X

APPLICATION OF FEED-FORWARD BACKPROPAGATION NEURAL NETWORK FOR THE DIAGNOSIS OF MECHANICAL FAILURES IN ENGINES PROVOKED IGNITION

APLICACIÓN DE UNA RED NEURONAL FEED-FORWARD BACKPROPAGATION PARA EL DIAGNÓSTICO DE FALLAS MECÁNICAS EN MOTORES DE ENCENDIDO PROVOCADO

Wilmer Contreras Urgilés[1,*], José Maldonado Ortega[1], Rogelio León Japa[1]

Abstract

This research explains the methodology for the creation of a diagnostic system applied to the detection of mechanical failures in vehicles with gasoline engines through artificial neural networks. The system is based on the study of the intake phase of the Otto cycle, which is recorded through the physical implementation of a MAP sensor (Manifold Absolute Pressure). A strict sampling protocol and its corresponding statistical analysis are applied. Statistical values of the MAP sensor signal such as, area, energy, entropy, maximum, mean, minimum, power and RMS, were selected according to the greater amount of information and significant difference. The data were obtained with the application of 3 statistical methods (ANOVA, correlation matrix and Random Forest) to create a database that allows the training of a neural network feed-forward backpropagation, with which a classification error of 1.89 e^{-11} was achieved. The validation of the diagnostic system was carried out by the generating supervised failures in different engines with provoked ignition.

Keywords: diagnosis, mechanical failures, network feed-forward backpropagation, ANOVA, correlation matrix, Random Forest.

Resumen

En la presente investigación se explica la metodología para la creación de un sistema de diagnóstico aplicado a la detección de fallas mecánicas en vehículos con motores a gasolina mediante redes neuronales artificiales, el sistema se basa en el estudio de la fase de admisión del ciclo Otto, el cual es registrado a través de la implementación física de un sensor MAP (*Manifold Absolute Pressure*). Se emplea un estricto protocolo de muestreo y su correspondiente análisis estadístico. Los valores estadísticos de la señal del sensor MAP: área, energía, entropía, máximo, media, mínimo, potencia y RMS se seleccionaron en función al mayor aporte de información y diferencia significativa. Los datos se obtuvieron con la aplicación de 3 métodos estadísticos (ANOVA, matriz de correlación y Random Forest) para tener una base de datos que permita el entrenamiento de una red neuronal *feed-forward backpropagation*, con la cual se obtiene un error de clasificación de 1.89e^{-11}. La validación del sistema de diagnóstico se llevó a cabo mediante la provocación de fallas supervisadas en diferentes motores de encendido provocado.

Palabras clave: diagnóstico, fallos mecánicos, red feed-forward backpropagation, ANOVA, matriz de correlación, Random Forest.

[1,*] Research Group of Transportation Engineering (GIIT), Mechanical Engineer, Universidad Politécnica Salesiana Cuenca – Ecuador. Autor para correspondencia ✉: rcontreras@ups.edu.ec
http://orcid.org/0000-0003-2300-9457, http://orcid.org/0000-0002-3846-2599,
http://orcid.org/0000-0003-2142-3769

Received: 21-08-2018, accepted after review: 09-11-2018

Suggested citation: Contreras Urgilés, W.; Maldonado Ortega, J. and León Japa, R. (2019). «Application of feed-forward backpropagation neural network for the diagnosis of mechanical failures in engines provoked ignition». INGENIUS. N.°21, (january-june). pp. 32-40. DOI: https://doi.org/10.17163/ings.n21.2019.03.

1. Introduction

Nowadays, operators and technicians in the area of automotive transportation use rudimentary diagrams for diagnosing and repairing engines with provoked ignition (EPI), which implies subjectivity in the diagnosis, longer periods for fault detection, lack of assertiveness and, as a consequence, high maintenance costs.

Therefore, it becomes necessary to apply new methodologies and specialized techniques for quicker diagnosis, thus optimizing resources for fault detection in engines of gasoline powered vehicles [1].

Due to the complexity for analyzing and interpreting the operational parameters of the EPI, it is necessary to use neural networks and computational mathematics for an efficient diagnosis of mechanical failures in Otto cycle engines. Howlett [2] shows that the EPI can be monitored for failure diagnosis or control, by analyzing the spark plug signal using artificial neural networks.

Similarly, Antory [3] suggests that it is possible to precisely determine different types of common failures in automobile diesel engines, by means of a diagnosis model that uses a variation of autoassociative neural networks (AANN).

Other neural networks have also been applied for fault diagnosis in the automotive area. Chen and Zhao [4] use radial basis functions neural networks (RBFNN) to diagnose failures of the engine fuel system.

Parallel strategies can be applied to train an artificial neural network (ANN), e.g. training of a modified Elman network for diagnosing engine failures. This recurrent network can be very effective and achieve a good diagnosing result, due to its dynamic input-output relationship [5]. Similarly, Lian *et al.* [6] present a method based in fuzzy logic and neural networks, for diagnosing faults in engines with provoked ignition.

Shah *et al.* [7] propose a system for failure recognition of internal combustion engines, applying the discrete wavelet transform (DWT) and RBF neural networks. Cay [8] developed an ANN model based on the backpropagation algorithm, for predicting specific brake fuel consumption, effective power and exhaust temperature of an EPI. Cay *et al.* [9] presented an ANN model for predicting the performance and the exhaust emissions of an EPI working with methanol and gasoline.

There have been diverse applications of neural networks in the calibration of spark ignited engines. R. F. Turkson *et al.* [10] have stated that ANN are capable of identifying the system for rapid prototyping, virtual detection, emerging control strategies and on board diagnostic (OBD) applications.

Another important application of ANN with kinetic models as activation functions of units in the hidden layer, was the study of the polyurethane degradation of an automotive intake manifold with isothermal treatment [11].

The proposed system for diagnosing engines with provoked ignition can detect faults that are not detected by the engine control unit (ECU). The system uses the signals from the manifold absolute pressure (MAP) and camshaft positioning (CMP) sensors, since they can enable minimizing the diagnosis time, in order to avoid employing intrusive techniques in the EPI such as using manometers for measuring the compression of the cylinders and the fuel pressure, vacuum meter, scanner, among others. The purpose of the aforementioned techniques is determining mechanical failure.

2. Materials and methods

This section discusses subjects such as the selection of the minimally invasive experimental unit and instrumentation, conditions for samples collection, methodology for data acquisition, obtaining the matrix of attributes, reduction of attributes and selection for ANN training, and Matlab algorithm for implementing the neural network.

2.1. Selection of the minimally invasive experimental unit and instrumentation

The main purpose is to avoid disassembling elements and pieces of the engine when diagnosing mechanical failures, for which a MAP sensor is installed in a vacuum outlet of the intake manifold to measure engine depression. The sensor will be placed after the acceleration butterfly, to prevent the connection from affecting the engine operation.

The identification of each cylinder is carried out using the registered signal from the CMP sensor. Figure 1 shows the experimental unit tested in the engine of a Hyundai Sonata 2.0 DOHC, a personal computer (PC), a tablet, the data acquisition tool NI DAQ-6009 and the interface of an automotive scanner. On the other hand, Figure 2 shows the connection of the MAP sensor, the vacuum outlet and the Ni DAQ-6009.

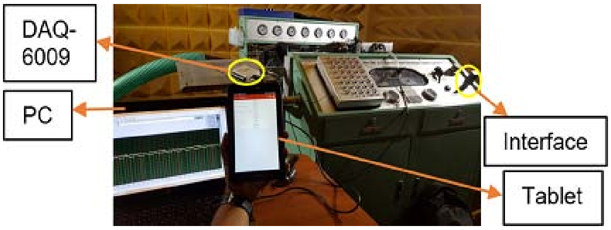

Figure 1. Engine instrumentation.

Figure 2. Connection of the MAP sensor.

2.2. Conditions for samples collection

The software LabView 2017 and the data acquisition card NI DAQ-6009 were used for collecting the samples. The samples are taken with the engine idle, at approximately 850 rpm, for a temperature range of the MAP sensor between 92 °C y 97 °C and 40 % load; these conditions were confirmed using the scanner.

In a preliminary experimental study it was found that the signal of the MAP sensor exhibits higher frequency peaks. As a consequence, each signal was sampled at a frequency of 10 KHz during a period of 5 seconds; such frequency exceeds Nyquist criterion (1.416 KHz).

2.3. Methodology for data acquisition

Figure 3 presents the physical elements required for sampling the signals.

Figure 3. Elements required for collecting the samples.

The flowchart shown in Figure 4 represents the procedure for obtaining the data from the signals of the MAP and CMP sensors, with the engine operating correctly (Figure 4(a)) or under a supervised failure (Figure 4(b)). Such procedure starts with the revision of the engine to determine its condition.

Then, the connection of the sensors is verified and the signal is recorded with the software LabView and saved to an Excel file.

Table 1 summarizes a total of 18 failures that can occur in the experimental unit, each with its corresponding identification code. The optimal operation of the engine is also included as a condition.

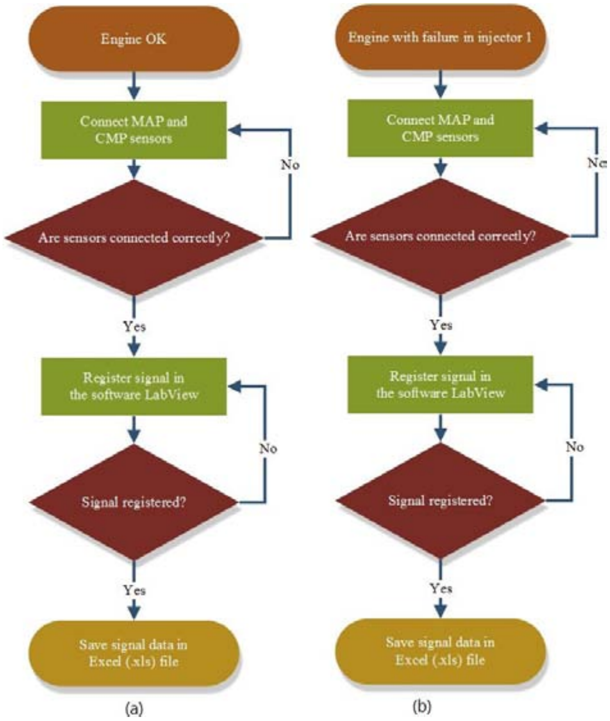

Figure 4. Flowchart of the procedure for data acquisition: (a) engine operating correctly, (b) engine with a failure

Table 1. Operational conditions of the experimental unit

N.°	Type of mechanical condition	Identification Code
1	Optimal operation	100
2	Failure in fuel injector 1	200
3	Failure in fuel injector 2	300
4	Failure in fuel injector 3	400
5	Failure in fuel injector 4	500
6	Failure in spark plug 1	600
7	Failure in spark plug 2	700
8	Failure in spark plug 3	800
9	Failure in spark plug 4	900
10	Failure in coil 1-4	1000
11	Failure in coil 2-3	1100
12	Low fuel pressure	1200
13	High fuel pressure	1300
14	Intake (+1) and exhaust (0) trees	1400
15	Intake (-1) and exhaust (0) trees	1500
16	Intake (0) ands exhaust (+1) tree	1600
17	Intake (0) and exhaust (-1) trees	1700
18	Intake (+1) and exhaust (+1) trees	1800
19	Intake (-1) and exhaust (-1) trees	1900

2.4. Obtaining the matrix of attributes

Once the signals have been acquired, an algorithm was coded in Matlab for reading and obtaining the matrix with general attributes, such as geometric mean, maximum, minimum, covariance, variance, standard deviation, mode, kurtosis factor, coefficient of asymmetry, energy, power, area under the curve, entropy, coefficient of variation, range, root mean square and crest factor.

Figure 5 illustrates a complete cycle of the engine (720° ±180°), with the tuning of the early intake opening (EIO) and late intake closing (LIC) distribution for each cylinder. Figure 6 shows windows of the MAP sensor signal for each cylinder; these signals are characterized.

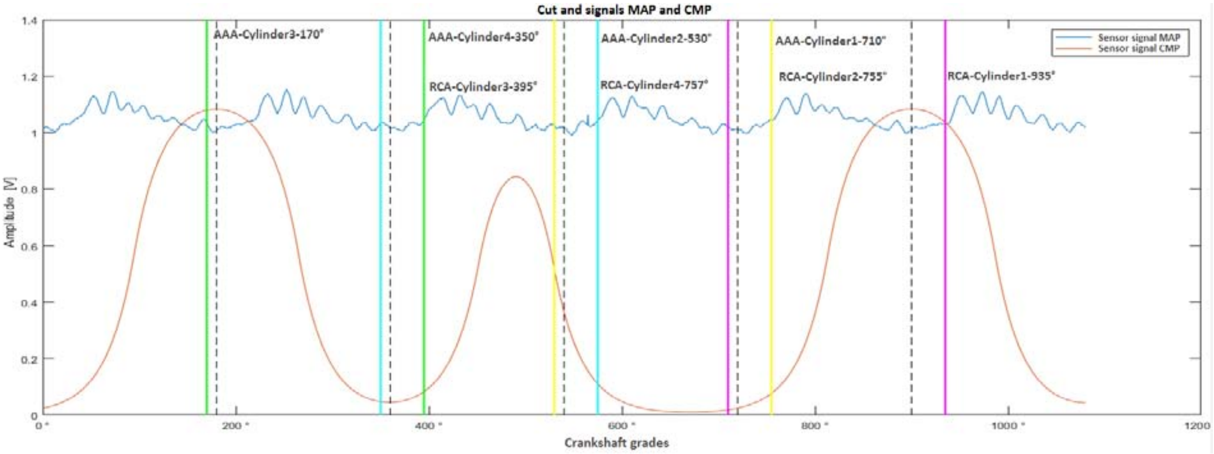

Figure 5. Signals of the MAP and CMP sensors.

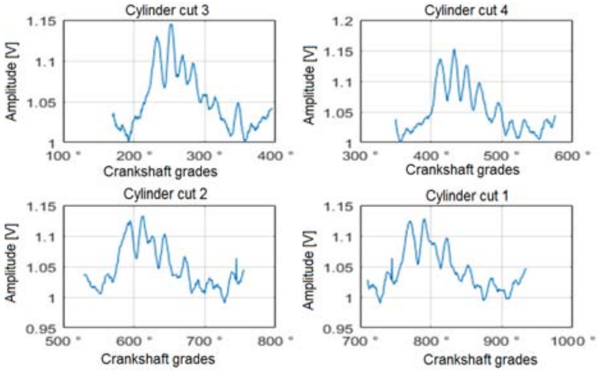

Figure 6. Windows of the MAP sensor signal for each cylinder.

2.5. Reduction of attributes

For selecting and reducing the number of attributes, the general matrix is analyzed using three statistical methods: analysis of variance (ANOVA), correlation matrix and Random Forest.

The application of a single factor ANOVA to all 18 attributes, helps to determine the best attributes that will be present in the general matrix. Since values of R^2 close to 100 % indicate a correct fit of the model to the data, greater values of this parameter are used to determine the variation among the attributes. In addition, values of p close to 0 determine if the attributes are statistically significant [12].

With respect to the correlation matrix, attributes with coefficients close to –1 o 1 were discarded, since such values indicate strong relationship between the variables, either negative (–1) or positive (1). In fact, attributes with coefficients close to zero were selected, because there does not exist strong correlation between the variables [13].

Regarding the Random Forest method, it was used to estimate the importance of the attributes by means of techniques such as Curvature test, Standard CART and Interaction test. Then, Pareto analysis was applied to select the attributes with the higher priority, considering only the first 95 % of the accumulated distribution [14].

Table 2 contains the results of the applied statistical methods, i.e. ANOVA, correlation matrix and Random Forest.

The general matrix contains the 18 attributes corresponding to the 19 conditions which were induced in the experimental unit.

2.6. Selection of attributes for training the ANN

The attributes selected for training the neural network were the most often repeated, which were determined by means of a coincidence analysis carried out to the results of Table 2. The selected attributes are shown in Table 3, thus confirming the effectiveness of each method.

Table 2. General matrix of attributes

Statiscal methods	**Most important attributes according to the statistical methods**									
Analyzed Correlation coefficients 342	Coeff. of variation Range/value $\leq \pm 0.1$ / 222	Area Range/value $\leq \pm 0.1$ / 212	RMS Range/value $\leq \pm 0.1$ / 216	Mean Range/value $\leq \pm 0.1$ / 212	Energy Range/value $\leq \pm 0.1$ / 220	Entropy Range/value $\leq \pm 0.1$ / 214	Mínimum Range/value $\leq \pm 0.1$ / 204	Median Range/value $\leq \pm 0.1$ / 214	Power Range/value $\leq \pm 0.1$ / 214
ANOVA R^2=100 % p=0,00	Median R^2=99,4 % p=0,00	Area R^2=99,39 % p=0,00	Mean R^2=99,39 % p=0,00	Minimum R^2=99,38 % p=0,00	Maximum R^2=99,38 % p=0,00	RMS R^2=99,26 % p=0,00	Power R^2=99,25 % p=0,00	Energy R^2=99,25 % p=0,00	Entropy R^2=99,16 % p=0,00
Forest Curvature % of Importance (0 a 2.5)	Energy % Imp. 2,4	RMS % Imp. 2,3	Entropy % Imp. 2,25	Maximum % Imp. 2,2	Area % Imp. 2,18	Mean % Imp. 2,15	Power % Imp. 2	Minimum % Imp. 1,9	Crest factor % Imp. 1,6
Forest Standard Cart % of Importance (0 a 3)	Energy % Imp. 2,85	Entropy % Imp. 2,7	RMS % Imp. 2,65	Mean % Imp. 2,64	Maximum % Imp. 2,63	Area % Imp. 2,6	Power % Imp. 2,55	Minimum % Imp. 2,46	Coeff. of variation % Imp. 2,4
Forest Robust % of Importance (0 a 12)	Standar Deviation % Imp. 10,15	Variance % Imp. 10,13	Energy % Imp. 10,11	Area % Imp. 10,09	RMS % Imp. 9,5	Mean % Imp. 9,1	Power % Imp. 8,7	Maximum % Imp. 8,5	Minimum % Imp. 8,4

Table 3. Attributes used to train the ANN

Statistical atributes	**Number of repetitions**
Area (v^2)	5
Energy (J)	5
Entropy (J)	4
Maximum (V)	4
Mean (V)	5
Minimum (V)	5
Power (mW)	5
RMS (V)	5

2.7. Matlab algorithm for implementing the neural network

Different network configurations were created and trained using the Matlab neural network toolbox, in the search for the network that exhibits good generalization ability.

Figure 7 shows the flow chart of the procedure for creating an ANN.

The procedure starts reading the matrix of inputs and target data for the ANN. Then, for better training performance, the data is normalized using the corresponding maximum values. At last, the ANN is created.

Figure 8 illustrates the structure of the feed-forward backpropagation ANN.

Once created, the neural network is trained considering the following training parameters:

1. Training algorithm
2. Number of epochs
3. Maximum error

Then, the classification performance of the trained neural network is tested. Is the classification error is greater than 5 %, the parameters are varied and the training is repeated.

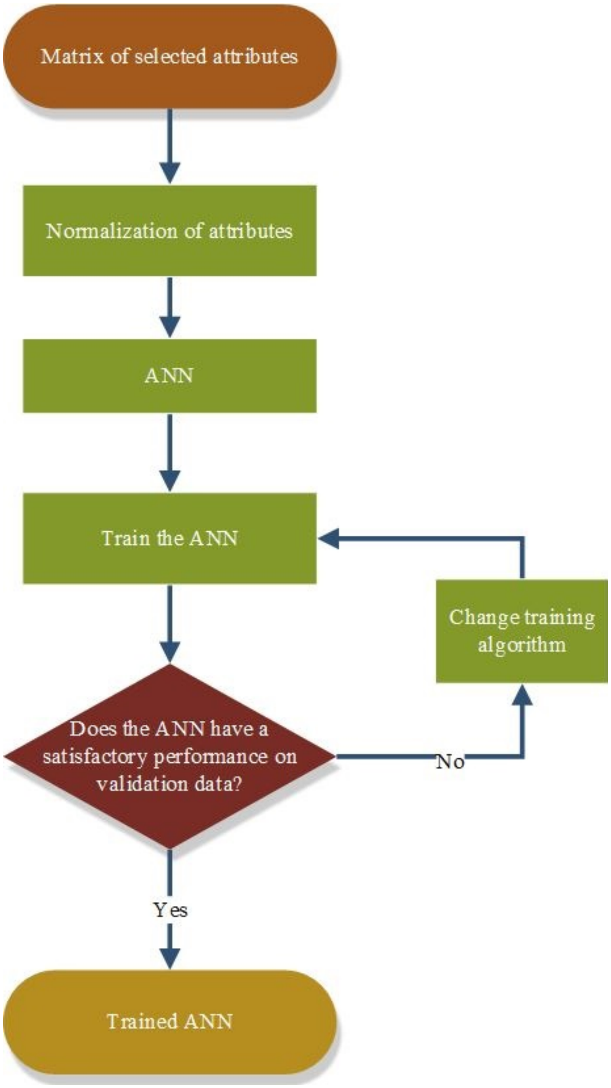

Figure 7. Flowchart of the procedure for ANN creation

Figure 9 shows the classification error of different training configurations, which were carried out searching for the neural network with the smallest possible error.

The neural network trained with the function trainscg had an error of 1.89e^{-11} %.

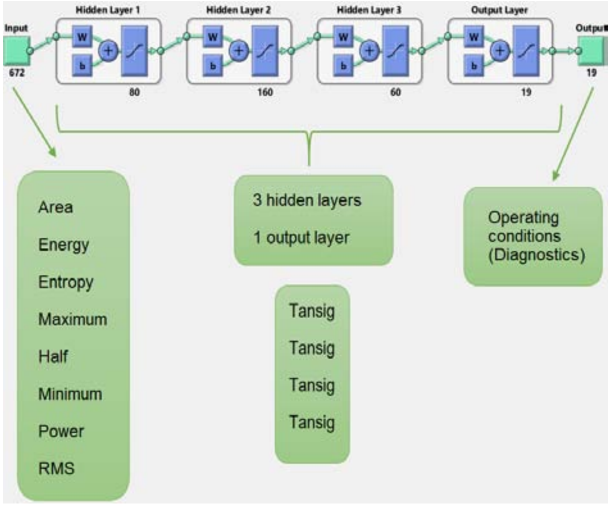

Figure 8. Structure of the neural network.

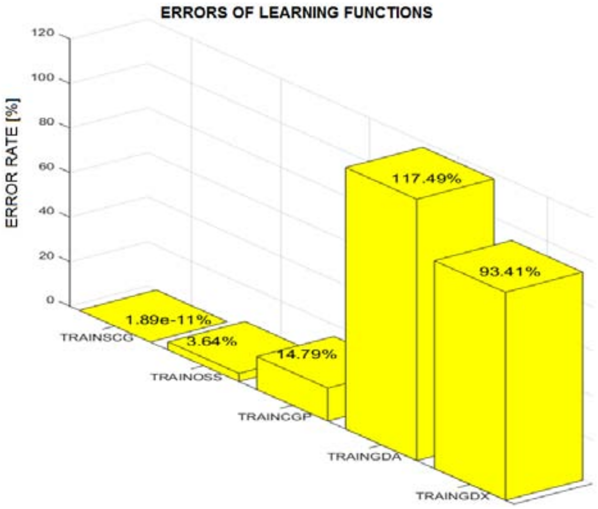

Figure 9. Errors for different training algorithms.

Figure 10 shows the Pearson correlation coefficient R of the created neural network, which is available in the Matlab string variable red.trainFcn = 'trainscg'.

The lines represent target values and the black circles the corresponding values estimated by the ANN. The neural network exhibits a good performance, since R=1 for training, validation and testing, which indicates a strong linear relationship between the real conditions of the EPI and the results given by the neural network [15].

On the other hand, Figure 11 shows a comparison between the output of the neural network and the target value, for the 19 mechanical conditions under consideration.

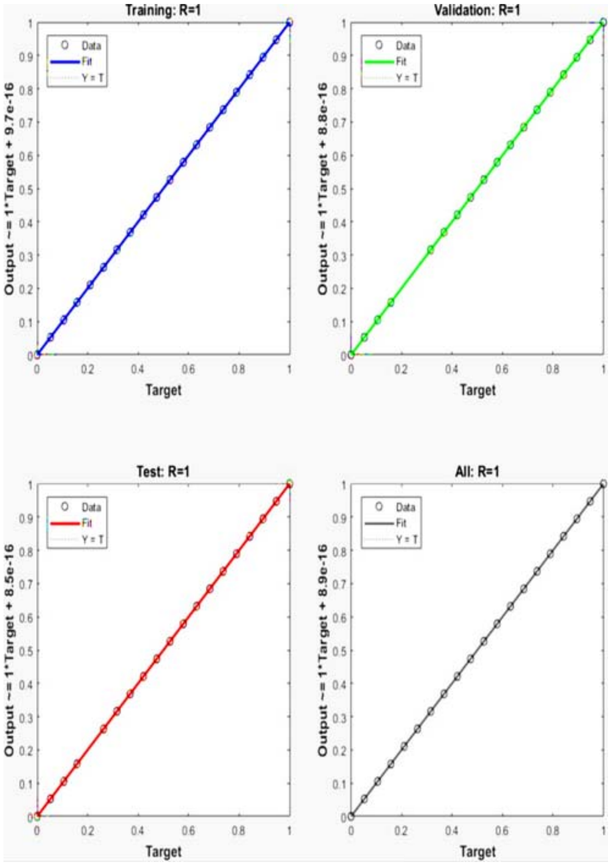

Figure 10. Correlation between the targets and the values estimated by the neural network.

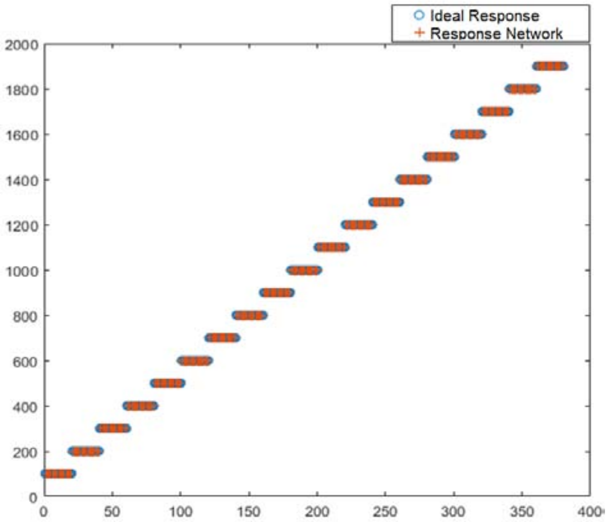

Figure 11. The Neural network trained with function «trainscg» achieved a percentage error of 1.89e^{-11}.

3. Results and discussion

Tests under different operating conditions were conducted to confirm that the proposed diagnosing system works correctly.

Specifically, two failure conditions were considered: injector 1 (200) and coil 2-3 (1100).

Figure 12 shows the results for a failure condition in injector 1. The average error between the target values and the outputs of the neural network was 0.0127.

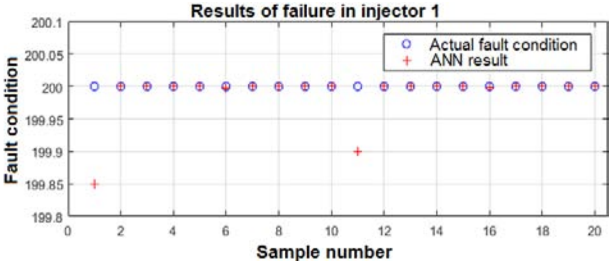

Figure 12. Results for a failure condition in injector 1.

On the other hand, Figure 13 shows the results for the failure condition in coil 2-3. The average error between the target values and the outputs of the neural network was 0.0060.

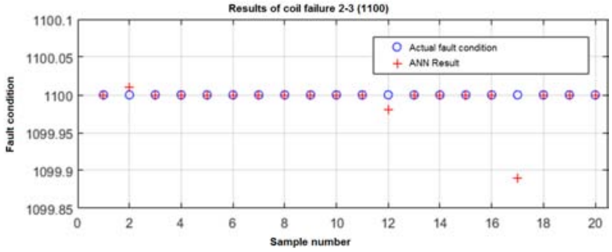

Figure 13. Results for a failure condition in the ignition coil 2-3.

Results show that the differences between the target values and the outputs of the ANN were very close to zero. Therefore, the proposed diagnosing system is capable of detecting a real failure condition.

In fact, Figure 14 shows that Tukey statistical method with a confidence interval of 95 %, determines that there is not significant statistical difference between the real condition of the engine and the responses of the ANN, since their means are equivalent.

In addition, the intervals shown in Figure 15 indicate that there is no difference between the average values of the tests in the different operating conditions of the engine.

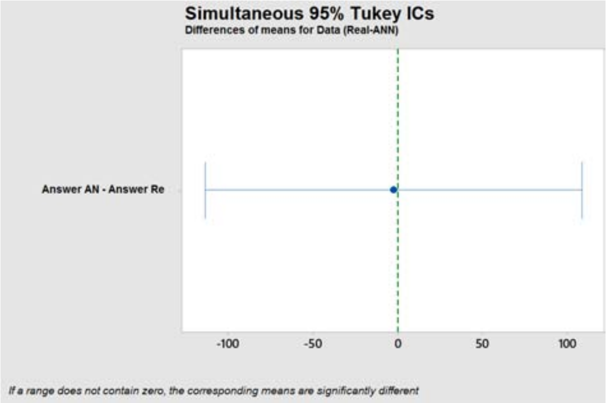

Figure 14. Difference between the means of the real data vs. ANN response.

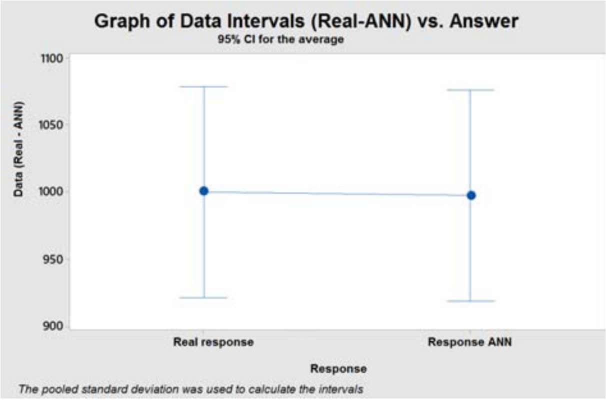

Figure 15. Intervals of real data vs. ANN response.

Similarly, Figure 16 confirms that there is relationship between the expected and neural network responses, since they share the same group letter (A) and the p-value is 0.965. This results in a confidence value of 96.5 %, which is very acceptable in the diagnosis of internal combustion engines with provoked ignition.

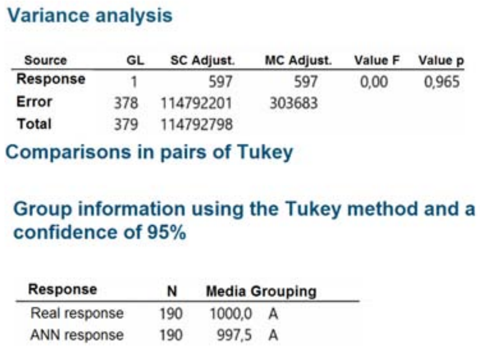

Variance analysis

Source	GL	SC Adjust.	MC Adjust.	Value F	Value p
Response	1	597	597	0,00	0,965
Error	378	114792201	303683		
Total	379	114792798			

Comparisons in pairs of Tukey

Group information using the Tukey method and a confidence of 95%

Response	N	Media	Grouping
Real response	190	1000,0	A
ANN response	190	997,5	A

Figure 16. Results of the analysis of variance and comparisons in Tukey pairs.

4. Conclusions

The developed neural network model had a classification error of 1.89e-11 with the training function trainscg, which yielded an accurate identification of the different types of mechanical conditions of the EPI. Therefore, such model constitutes a completely viable alternative to be integrated in a diagnosing system, due to the high computational speed offered by the artificial neural networks.

By means of a single factor analysis of variance, a p-value=0,965 was obtained, demonstrating that the targets and the ANN responses are equivalent since this p-value indicates that there is not a significant statistical difference between them. This work showed that feed-forward backpropagation neural networks are suitable for detecting mechanical failure conditions in engines with provoked ignition; in addition, the applied diagnosing technique has the advantage of avoiding disassembling elements and pieces of the engine, thus being a reliable and highly precise minimally invasive technique.

Statistical methods such as analysis of variance (ANOVA), correlation matrix and Random Forest, were applied to determine the best attributes for training the ANN. Then, the results were grouped in a general matrix, to help in the selection of the attributes with greater coincidence and importance for differentiating patterns of mechanical failures.

References

[1] W. Contreras, M. Arichávala, and C. Jerez, "Determinación de la presión máxima de compresión de un motor de encendido provocado basado en una red neuronal artificial recurrente," *INGENIUS*, no. 19, pp. 9–18, 2018. [Online]. Available: http://doi.org/10.17163/ings.n19.2018.01.

[2] R. J. Howlett, "Condition monitoring and fault diagnosis in a domestic car engine using a neural network," in *IEE Colloquium on Artificial Intelligence in Consumer and Domestic Products (Digest No. 1996/212)*, Oct 1996, pp. 5/1–5/4. [Online]. Available: https://doi.org/10.1049/ic:19961142

[3] D. Antory, "Fault diagnosis application in an automotive diesel engine using auto-associative neural networks," in *International Conference on Computational Intelligence for Modelling, Control and Automation and International Conference on Intelligent Agents, Web Technologies and Internet Commerce (CIMCA-IAWTIC'06)*, vol. 2, Nov 2005, pp. 109–116. [Online]. Available: https://doi.org/10.1109/CIMCA.2005.1631454

[4] D. Chen and P. Zhao, "Study of the fault diagnosis method based on rbf neural network," in *2011 2nd International Conference on Artificial Intelligence, Management Science and Electronic Commerce (AIMSEC)*, Aug 2011, pp. 4350–4353. [Online]. Available: https://doi.org/10.1109/AIMSEC.2011.6010128

[5] Y. G. Wu, C. Z. Song, and L. P. Shi, "Notice of retraction fault diagnosis of engine mission using modified elman neural network," in *2010 Sixth International Conference on Natural Computation*, vol. 2, Aug 2010, pp. 996–998. [Online]. Available: https://doi.org/10.1109/ICNC.2010.5582900

[6] P. Lian, T. Y. Bin, N. Ning, and C. Aiping, "Application of fuzzy neural network in fault diagnosis of gasoline engine," in *2009 9th International Conference on Electronic Measurement Instruments*, Aug 2009, pp. 4–602–4–605. [Online]. Available: https://doi.org/10.1109/ICEMI.2009.5274658

[7] M. Shah, V. Gaikwad, S. Lokhande, and S. Borhade, "Fault identification for i.c. engines using artificial neural network," in *2011 International Conference on Process Automation, Control and Computing*, July 2011, pp. 1–6. [Online]. Available: https://doi.org/10.1109/PACC.2011.5978891

[8] Y. Cay, "Prediction of a gasoline engine performance with artificial neural network," *Fuel*, vol. 111, pp. 324–331, 2013. [Online]. Available: https://doi.org/10.1016/j.fuel.2012.12.040

[9] Y. Çay, I. Korkmaz, A. ÇiÇek, and F. Kara, "Prediction of engine performance and exhaust emissions for gasoline and methanol using artificial neural network," *Energy*, vol. 50, pp. 177–186, 2013. [Online]. Available: https://doi.org/10.1016/j.energy.2012.10.052

[10] R. F. Turkson, F. Yan, M. K. A. Ali, and J. Hu, "Artificial neural network applications in the calibration of spark-ignition engines: An overview," *Engineering Science and Technology, an International Journal*, vol. 19, no. 3, pp. 1346–1359, 2016. [Online]. Available: https://doi.org/10.1016/j.jestch.2016.03.003

[11] B. D. de L. Ferreira, N. R. Araújo, R. F. Ligório, F. J. Pujatti, M. I. Yoshida, and R. C. Sebastião, "Comparative kinetic study of automotive polyurethane degradation in non-isothermal and isothermal conditions using artificial neural network," *Thermochimica Acta*, vol. 666, pp. 116–123, 2018. [Online]. Available: https://doi.org/10.1016/j.tca.2018.06.014

[12] Minitab. (2018) Minitab software. [Online]. Available: https://goo.gl/NDoMTo

[13] Incibe-cert. (2015) Incibe-cert. [Online]. Available: https://goo.gl/5h7696

[14] Mathworks. (2018) Mathworks. [Online]. Available: https://goo.gl/GVhckj

[15] J. Calderón, B. Castillo, and J. Moreno, "Diseño de una red neuronal para la predicción del coeficiente de pérdidas primarias en régimen de flujo turbulento," *INGENIUS*, vol. 20, pp. 21–27, 2018. [Online]. Available: https://doi.org/10.17163/ings.n20.2018.02.

Scientific Paper / Artículo Científico

UNIVERSIDAD POLITÉCNICA SALESIANA ECUADOR
INGENIUS
Revista de Ciencia y Tecnología
https://doi.org/10.17163/ings.n21.2019.04
pISSN: 1390-650X / eISSN: 1390-860X

THERMODYNAMIC ANALYSIS OF ONE AND TWO STAGES ABSORPTION CHILLER POWERED BY A COGENERATION PLANT

ANÁLISIS TERMODINÁMICO DE UN CHILLER DE ABSORCIÓN DE 1 Y 2 ETAPAS DE UNA PLANTA DE COGENERACIÓN

Hugo F. Zuñiga-Puebla[1,*], E.C. Vallejo-Coral[2], Jose Ramon Vega Galaz[3]

Abstract

Thermodynamics models of a single and a non-common double stage ammonia-water absorption chiller that use waste heat (from three reciprocating engines of 8.7 MW each one) are developed to analyze the performance of the chiller for different operative conditions. A comparison of a single stage refrigeration system with the two stages proposed system is performed in this paper. The coefficient of performance (COP) obtained for both systems are the same, but the heat flux removed from the cooling media with the two-stage system increase from 1.3MW (single stage) until 1.6 MW due to the heat recovered increased with the second generator. The heat recovered used by the chiller was 3.8 MW, and the utilization factor of the cogeneration plant was 58.11%, and the cooling capacity of the equipment was 1,623 kW. Finally, the estimated economics savings for electric power due to the implementation of the absorption chiller that uses exhaust gases in place of a common refrigeration system by vapor compression with the same cooling capacity was 142,000.00 USD/year.

Keywords: Absorption chiller, cogeneration, heat recovery refrigeration, waste energy, COP.

Resumen

Se han desarrollado modelos termodinámicos de enfriadores de agua por absorción de una etapa y ciclo no común de dos etapas que usan calor de desecho (de motores de combustión interna de 8.7 MW cada uno) para analizar las condiciones de operación de los equipos. Se ha realizado la comparación del sistema de una etapa con el sistema propuesto (2 etapas) en esta investigación. El coeficiente de desempeño (COP) obtenido para ambos sistemas fue el mismo pero el calor removido del espacio refrigerado aumento de 1.3 MW (una etapa) a 1.6 MW (dos etapas) debido a que se recupera más energía residual utilizando un segundo generador. El calor residual aprovechado por el equipo de refrigeración fue de 3.8 MW y el factor de planta del proceso de cogeneración fue de 58.11 % y la capacidad de refrigeración del equipo fue de 1,623 kW. Finalmente, los ahorros económicos estimados por concepto de energía eléctrica que se tienen por implementar el sistema de refrigeración por absorción que utiliza gases de escape como fuente de energía en lugar de un equipo común de refrigeración por compresión de la misma capacidad son 142,000.00 USD/año.

Palabras clave: Absorción, calor recuperado, cogeneración, COP, energía desperdiciada.

[1,*] Faculty of Mechanical Engineering, Escuela Politécnica Nacional, Ecuador. Corresponding author ✉: hugo.zuniga@epn.edu.ec http://orcid.org/0000-0003-0732-8108.

[2] National Institute of Energy Efficiency and Renewable Energy, Ecuador. http://orcid.org/0000-0003-2065-0484.

[3] Department of Electrical Engineering, Instituto Tecnológico y de Estudios Superiores de Monterrey ITESM, Mexico http://orcid.org/0000-0003-7630-2035.

Received: 14-03-2018, accepted after review: 03-12-2018

Suggested citation: Zuñiga-Puebla, H. F.; Vallejo Coral, E. C. and Vega Galaz, J. R. (2019). «Thermodynamic analysis of one and two stages absorption chiller powered by a cogeneration plant». INGENIUS. N.°21, (january-june). pp. 41-52. DOI: https://doi.org/10.17163/ings.n21.2019.04.

1. Introduction

The vapor compression refrigeration system is widely used in the refrigeration industry. In recent years, the scenario for energy demand in industrial cooling has undergone significant changes, the most significant among them, is the ban on chlorofluorocarbon (CFCs) as cooling agents because of their effect on the ozone layer. Thus, the use of alternative fluids for compression refrigeration systems were studied, and now the manufactures of refrigeration equipment use other types of fluids, for example isobutane (R600a) [1]. The disadvantages of the compression system are high electricity consumption, high operation costs and pollution. The absorption refrigeration systems (ARS), which are powered by heat instead of electricity, could be a good alternative to reduce electricity consumption and obtain economic revenues [2–4].

The absorption refrigeration systems (ARS) were developed to use thermal energy as a cycle input instead of electricity. Two-stage ARS have been developed to improve the operation of these systems [2, 5, 6]. Both systems work with two fluids: the refrigerant and the fluid to absorb the refrigerant in a solution to increase the pressure with a pump, the most common pair of fluids detailed in the bibliography are lithium bromide/water (H_2O as refrigerant and LiBr as transport medium) and ammonia/water (NH_3 as refrigerant and H_2O as transport medium). The ammonia/water systems are used to obtain low evaporation temperatures (for example freezing application) [7]. Hence, the ARS could be a good alternative to reduce the electricity consumption of industrial cooling and obtain economic revenues [2–4].

Colorado and Rivera [6] compared a vapor compression refrigeration system with a hybrid system (compression/absorption) with the first and second laws of thermodynamics. They used R134a and CO_2 as refrigerants of the compression systems and a solution of H_2O/LiBr in the absorption cycle. The hybrid system has a cascade heat exchanger where the condenser compression system is the evaporator of the absorption system. The main objective was to reduce the energy used in the compressor. The research results show that the hybrid system consumes 45% less electricity than the simple compressor cycle. Also, the coefficient of performance (COP) obtained in the hybrid system is higher with R134a.

One of the advantages of ARS is the possibility to use various heat sources as input for the generator. Said et al. [8] designed and built a solar powered absorption chiller with NH_3/H_2O to the Saudi Arabian climatic conditions. The system aim was to produce ice and cool a building's enclosed main hall which presents 10kW of cooling load. During the test, the chiller highest cooling capacity observed was of 10.1 kW, and it produced ice despite the high condensation temperature (45 °C) due to summer climatic conditions. Other authors as Wang *et al.* [9] studied the optimal heat sources for different applications of ARS.

The waste heat of exhaust gases of boilers, combustion engines, turbines can be used as heat source for an absorption system. Du *et al.* [10] built a prototype of a single stage ammonia/water refrigeration system that used waste heat from a diesel engine with an active open heat pipe method, designed to obtain stability of the available heat. The authors designed the heat exchanger to recover waste energy for a specific capacity, and they combined condensation and absorption process in one unit which was cooled by circulated precooled solution. The system had a COP of 0.53, and the cooling capacity was 33.8 kW for a temperature of exhaust gases of 567 °C.

Nowadays, manufacturers such as AGO are building absorption refrigeration systems that can be coupled with a heat exchanger to use solar collector or heat recovery hot water regenerator (HRHWG) with energy of exhaust gases [11]. This kind of systems presents different advantages compared with power generation systems such as: i) increasing energy efficiency with co/tri-generation, ii) reduction of CO_2 emissions, and iii) substitution of high-quality electric power with "low-grade" thermal energy in the form of waste heat. Moreover, among economic reasons are related to kind of systems such as: reduction of operating costs by using waste heat as the power source and minimal use of electricity.

The main objective of this work is to develop a thermodynamic model of a single stage and AGO's (non-conventional) two-stage system of ammonia/water absorption chiller designed and built by AGO [11] to analyze the performance of the chiller for different operation conditions. The absorption chiller uses waste energy recovered from the exhaust gases of reciprocating engines.

1.1. Description of complete cogeneration system

Figure 1 shows a scheme of the cogeneration power plant (CHP). In June 2017 the plant was installed by the "*Unión Energética del Noroeste SA de SV*" company, which sells electricity, and it is subsidiary of "*Negocio Agrícola San Enrique SA de SV*" company. The last one uses chillers to refrigerate its farm products. Both companies are in Agua Prieta in the federal state of Sonora, north-west in Mexico.

The CHP has three reciprocating engines with a total output of 26.1 MW (e) (each engine of 8.7 MW (e)) and 9.8 MW (t) is recovered from the exhaust gases and high-temperature refrigeration circuit. A heat recovery steam generator (HRSG) recovered 6 MW (t) producing vapor and a heat recovery hot water generator (HRHWG) recovered 3.8 MW(t).

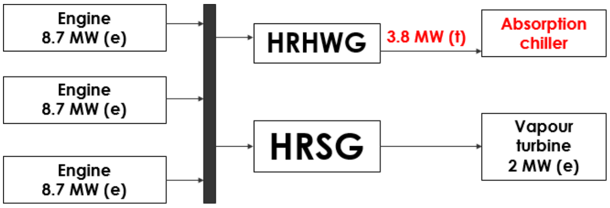

Figure 1. Powered cogeneration plant studied.

The vapor produced with the HRSG is used in a vapor turbine to produce 2 MW (e). The hot water produced in the HRHWG is used as an input of the absorption chillers to generate cold air for the refrigeration of warehouses where agricultural products from the hot Sonora area are conserved.

2. Theoretical Background

2.1. Compression versus absorption

Energy is required to transport heat from a low-temperature to a high-temperature bulb. A fluid refrigerant undergoes a series of thermodynamic transformations. Each refrigerant has a defined and different behavior, and as it is well known, the cycles prevent continuous replenishment of the refrigerant [12]. The main methods of industrial cooling are compression and absorption.

The compression cycle is based on the conventional refrigeration cycle. It transfers heat from the cooling space to the environment using electricity as its input. It works by increasing and lowering the pressure of the refrigerant, changing its saturation temperature. The compression system has a condenser (outdoor unit), an evaporator (inside the cooling space), an expansion valve and a compressor (transports the refrigerant) [13]. Its performance is high considering that the system input is electrical energy and the output is heat removed from the evaporator. These devices work by increasing and lowering the pressure of the refrigerant changing the saturation temperature.

The absorption cycle, uses a pump to increase the pressure of the system and not a compressor, which reduces its electricity consumption. However, it requires an additional heat flux in the generator, which makes the system performance lower than the compression system [3]. This additional heat flux may come from free or residual energy sources such as solar energy or waste heat, which could be economically advantageous [5, 14]. The most common pair of working fluids are: lithium bromide-water (refrigerant) or water- ammonia (refrigerant). This cycle uses only a pump to increase the pressure of the system and for this reason the electric energy used is lower than in the compression cycle. Also, in the absorption system it is necessary to provide a heat flux in the generator, which may come from solar energy or waste energy. The performance of the system is low, but it needs heat as the main input in the system instead of electricity [3].

In air-conditioning of spaces, the most used absorbent-refrigerant pair is lithium-water bromide. The absorption systems (single stage) require an external heat source at a temperature between 80 °C and 120 °C, and have a lower performance. The possibility of using free or residual energy sources is the advantage of absorption versus compression [5, 14].

Finally, another advantage that offers this type of devices compared to compression-type chillers is faint sound level and structure-borne sound propagation (low noise level, no vibrations).

2.2. Description of current absorption chiller products

2.2.1. Water/lithium bromide chillers

Water/lithium bromide is an absorption working fluid that has been used widely since the 1950s when the technology was pioneered by several manufacturers in the United States. This working fluid utilizes water as the refrigerant, and therefore, it is limited to refrigeration temperatures above 0°C. Absorption machines based on water/lithium bromide are typically configured as water chillers for air-conditioning systems in large buildings. They are available in sizes ranging from 35 to 5,000 kW.

The coefficient of performance (COP) of these machines, defined as the refrigeration capacity divided by the driving heat input, typically varies over the range 0.7<COP<1.2 as a function of the cycle configuration. The most used technology is vapor compression chillers, and the choice between the compression or absorption chillers depends strongly of economic factors [5].

2.2.2. Ammonia/water chillers

Ammonia/water is an absorption pair of fluids that have been used since the late 1800s, at which time it was used for ice production before the introduction of the vapor compression technology. The ammonia is the refrigerant, and water is the transport medium. Thus, the role of water is distinctly different between ammonia/water and the water/lithium bromide. One advantage of ammonia as refrigerant is that it permits to work with lower temperatures because the freezing point of ammonia is -77.7°C. However, the toxicity of ammonia is a factor that has limited its use to well-ventilated areas.

The ability to provide direct gas-fired and air-cooled air conditioning is the primary selling point of water-ammonia chillers technology. Machines are available in capacity ranging from 10-90 kW with COP typically around 0.5-1.5. These units have a niche market because there are few competing gas-fired technologies suitable for many applications. Custom ammonia/water applications in industry for waste heat or renewable energy utilization are an interesting application of this technology [5,12].

2.3. Single stage system

Figure 2 shows a single stage system (two working pressures and one generation & absorption stages) of absorption chiller that works with ammonia as refrigerant and water as solvent. The refrigerant ammonia allows to get lower evaporator temperatures than other substances and it is available for a wide variety of applications. Therefore it is one of the classic refrigerants [5,11].

The components of the absorption refrigeration system are:

- **Evaporator:** It removes heat from the cooling media from the chiller (solution of water and glycol). The heat flux removed ($\dot{Q}_{evap}$) evaporates the refrigerant (Ammonia-NH_3) at a low temperature and a low-pressure environment.
- **Dephlegmator:** It is a heat exchanger where a partial condensation of the vapor (rich in ammonia) that is coming from the generator occurs (1). The heat rejection in this process allows to obtain pure ammonia vapor that goes towards the condenser (2V), and the condensate liquid (2L) (rich in water) returns to the rectifier per gravity.

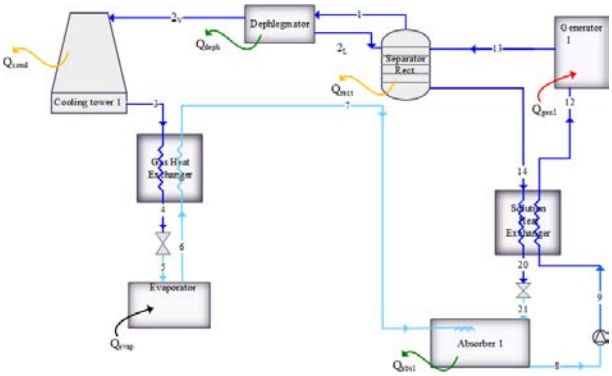

Figure 2. Single stage absorption system.

- **Condenser:** In the input of this component the ammonia vapor (2V) is at high pressure and it until condensate state when it passes through the heat exchanger (3).
- **Gas Heat Exchanger:** It is a heat recovered where the ammonia liquid that comes from the condenser (3) transfer heat to the ammonia vapor that goes to the absorber (6). It helps to subcooling the refrigerant and increase the system COP.
- **Expansion valves:** They reduce the pressure of liquid ammonia (4) and of the poor solution that goes to the absorber (20).
- **Absorber:** A dilute solution of ammonia water (21) absorbs the refrigerant vapor (7). The mixture must be simultaneously cooled down to dilute sufficient ammonia in the solution obtaining a rich solution at the output of this component (8). Therefore, to comply with this process, it is necessary to reject heat flux ($\dot{Q}_{abs}$).
- **Pump:** It transports the rich solution (8) increasing the pressure of the fluid which is an incompressible solution (liquid).
- **Solution Heat Exchanger:** It is a heat recovered where the poor solution (14) transfers heat to the rich solution (9) to be preheated.
- **Generator:** In this component, the rich solution (12) is heated, allowing to obtain vapor with a high concentration of ammonia (13V) and the solution is dilute respect to ammonia.
- **Rectifier:** It is a fractionating column required to condensate the partially vaporized water that is leaving from the generator and produce only very high purity ammonia vapor (1) that goes to the dephlegmator.

The COP of the single stage system is the relation of the heat flux removed in the evaporator respect to the input heat flux to the generator and the power consumed by the pump (Eq. (1)).

$$COP = \frac{\dot{Q}_{evap}}{\dot{Q}_{gen1} + \dot{W}_{pump1}} \tag{1}$$

Where:

COP - coefficient of performance
$\dot{Q}_{evap}$ - evaporator heat flux (kW)
$\dot{Q}_{gen1}$ - generator 1 heat flux (kW)
$\dot{W}_{pump1}$ mechanical power (kW)

2.4. Two-stage system (AGO equipment)

A scheme of the system studied in this project is shown in Figure 3. The information was obtained from the single line installation diagram of AGO project [11]. The principal components of the refrigeration system and the auxiliary systems are shown.

The refrigeration system studied is not a common two-stage absorption cycle described in the bibliography [1,5]. It has two stages of generation and absorption process where the vapor rich in ammonia is leaving only from the Generator 1 (13) to the dephlegmator. The liquid solution leaves from the rectifier (14), it goes to the Generator 2 where heat is added to the solution. As a result, after the separator 2, more quantity of ammonia is absorbed by the state (17). Also, a poor solution (20) is obtained and goes to the absorber 2 and absorber 1 respectively.

The main objective of this two-stage equipment is to recover more energy from the hot water to supply it to the working fluids of the refrigeration system. In this project, a comparison of a thermodynamic model for a single stage absorption refrigeration system (Figure 2) and a double stage system (Figure 3) is performed.

The COP of the double stage system is determined by Eq. (2), and it is the relation of the heat flux removed in the evaporator respect to the heat consumed in generators and the mechanical power required by the pumps.

$$COP = \frac{\dot{Q}_{evap}}{\dot{Q}_{gen1} + \dot{Q}_{gen2} + \dot{W}_{pump1} + \dot{W}_{pump2}} \qquad (2)$$

Where:

COP - coefficient of performance
$\dot{Q}_{evap}$ - evaporator heat flux (kW)
$\dot{Q}_{gen1}$ - generator 1 heat flux (kW)
$\dot{Q}_{gen2}$ - generator 2 heat flux (kW)
$\dot{W}_{pump1}$ - pump 1 mechanical power (kW)
$\dot{W}_{pump2}$ - pump 2 mechanical power (kW)

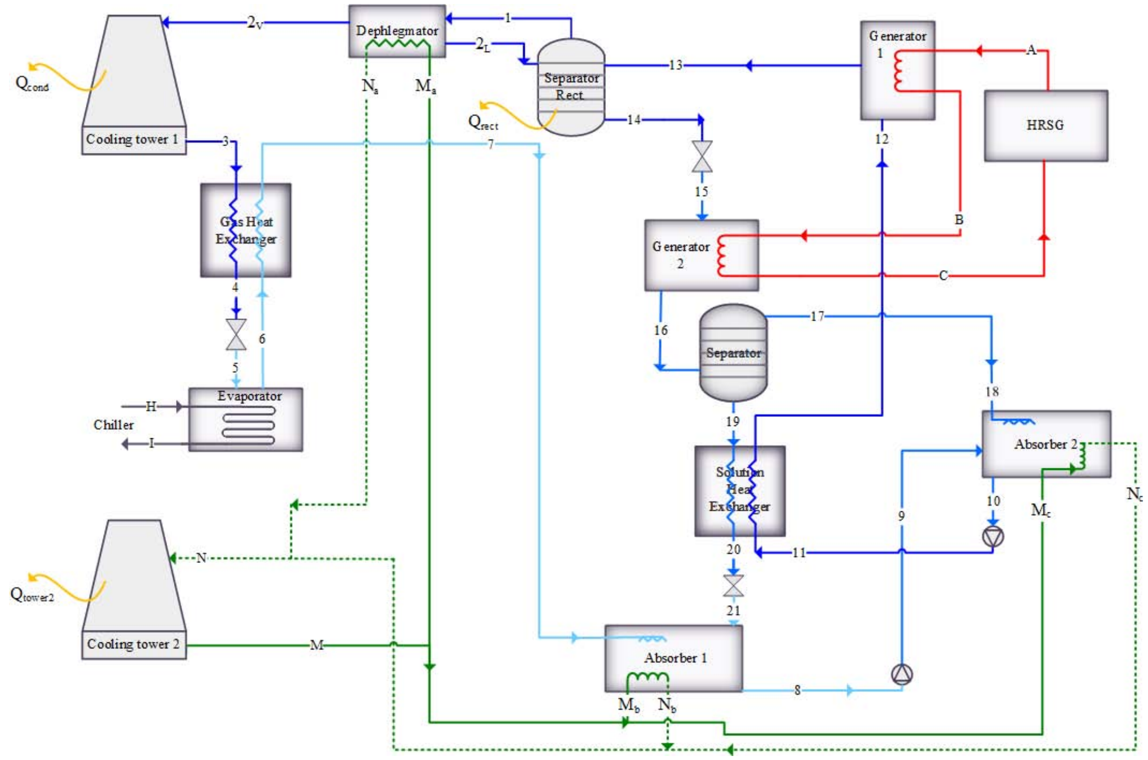

Figure 3. Double stage absorption equipment and auxiliary systems.

2.5. Auxiliary systems

In Figure 3, the auxiliary systems of the absorption system are included. They are interacting with different components of the absorption refrigeration system, and they are described below:

- **HRHWG:** It is a heat exchanger that uses the waste energy from the engine to produce hot water. In this case, the hot water (A) at 110 °C enters the Generator 1, deliveries heat to the ammonia-water solution and leaves (B) at 86 °C. This water continues to the Generator 2 where interchanges heat with the solution, and it goes out (C) at 80 °C. In normal operation conditions, the volumetric flow of water is 120 m_3/h.
- **The evaporator of the chiller:** The heat gained in the evaporator by the refrigerant (NH_3) is removed from a solution (glycol-water). In this system, the glycol enters (H) at -2 °C and it leaves (I) at -8 °C. The simulation developed in this project helps to determine the mass flow rate of glycol solution that can be cooled by this equipment.
- **Cooling tower 1:** In the condenser, the refrigerant needs to reject heat. This heat is rejected in a cooling tower cooled by water and air, with a capacity of 1250 kW.

- **Cooling tower 2:** The heat rejected from different components (absorber 1, absorber 2 and dephlegmator) evaporates the ammonia (M) and the vapor of ammonia (N) goes to the Cooling Tower 2 to condensate and continue the process. The capacity of this cooling tower is 3,750 kW.

The heat flux to be interchanged with the refrigeration system in the HRHWG and the evaporator chiller is calculated directly using the Eq. (3)

$$\dot{Q} = \dot{m} \times c_p \times \Delta T \tag{3}$$

Where:

$\dot{Q}$ - heat exchanger heat flux (kW)
$\dot{m}$ - water mass flow rate (kg/s)
C_p - water specific heat (kJ · kg/°C)
ΔT - temperature difference (°C)

The heat flux removed by the cooling towers are input data for the model of the refrigeration system developed in this project. The heat capacities of the cooling towers are used as a parameter for this model, and the thermodynamic and heat transfer process can be analyzed in detail in future work.

3. Model development

3.1. Thermodynamic analysis

The model was developed in EES (Engineering Equation Solver) [15] due to it has an external routine to know the ammonia water solution (liquid) and gas mixture properties. To address the thermodynamic study of the system presented in Figure 2 and Figure 3, we developed an appropriate methodology for each component as follows:

- **Generator:** The total mass, ammonia mass, and energy balances are expressed respectively in Eq. (4), Eq. (5), and Eq. (6).

$$\dot{m}_{12} = \dot{m}_{13V} + \dot{m}_{13L} \tag{4}$$

$$\dot{m}_{12} \times x_{12} = \dot{m}_{13V} \times x_{13v} + \dot{m}_{13L} \times h_{13V} \tag{5}$$

$$\dot{m}_{12} \times h_{12} + \dot{Q}_{gen1} = \dot{m}_{13V} \times h_{13V} + \dot{m}_{13L} \times h_{13V} \tag{6}$$

Where:

$\dot{m}_{12}$ - gas mixture mass flow rate (kg/s)
$\dot{m}_{13V}$ - gas mixture mass flow rate (kg/s)
$\dot{m}_{13L}$ - solution (liquid) mass flow rate (kg/s)
x_{12} - total ammonia mass fraction to generator 1
x_{13V} - ammonia steam mass fraction
h_{12} - gas mixture specific enthalpy of generator 1 (kJ/kg)
$\dot{Q}_{gen1}$ - generator 1 heat flux (kW)
h_{13V} - ammonia specific enthalpy of generator 1 (kJ/kg)

From this section, it is important to note that the amount of heat supplied to the ammonia-water solution flowing through the generator is equal to the heat delivered by the HRHWG defined by Eq. (7).

$$\dot{Q}gen1_{HRHWG} = \dot{m}_A \times c_p \times (T_A - T_B) \tag{7}$$

Where:

$\dot{Q}gen1_{HRHWG}$ - HRHWG heat flux (kW)
$\dot{m}_A$ - water (HRHWG) mass flow rate (kg/s)
C_p - water specific heat (kJ·kg/°C)
T_A - generator 1 inlet temperature (°C)
T_B - generator 1 outlet temperature (°C)

The mass and energy balances for generator 2 were performed under the same criteria.

- **Rectifier:** Mass and energy balances are developed, with the particularity that rectifier dissipates heat to the environment in response to its participation in the condensation of vaporized ammonia-water solution from the generator. This element performs the separation of the ammonia-water solution liquid and gaseous phases flowing through it. The rectifier is a fractionating column needed to condensate the partially vaporized water leaving from the generator and obtaining only ammonia-vapor of very high purity (1) which goes to the Dephlegmator.

- **Dephlegmator:** Heat is transferred to the auxiliary ammonia system to ensure that the refrigerant returns as vapor to the cooling tower 2, and the heat flux rejected is known with the Eq. (8).

$$\dot{Q}_{deph} = \dot{m}_{Ma} \times (h_{Na} - h_{Ma}) \tag{8}$$

Where:

$\dot{Q}_{deph}$ - dephlegmator heat flux (kW)
$\dot{m}_{Ma}$ - ammonia mass flow of dephlegmator rate (kg/s)
h_{Na} - outlet ammonia specific enthalpy (kJ/kg)
h_{Ma} - inlet ammonia specific enthalpy inlet (kJ/kg)

- **Condenser:** The heat removed from the ammonia vapor at the inlet is released into the atmosphere in the cooling tower.

- **Gas Heat Exchanger:** In the energy balance, to obtain the heat recovered by the ammonia vapor going to the absorber 1, the heat capacities of the incoming fluids to the heat exchanger are first determined using the ammonia's specific heat properties. Then, the minimum heat capacity is identified, as well as the largest temperature difference. In this way, the maximum heat flux that can be transferred will be equal the product of the minimum heat capacity and the largest temperature difference. Finally, the effectiveness of the heat exchanger is given in Eq. (9).

$$\varepsilon = \frac{\dot{Q}recov_{GHX}}{\dot{Q}_{max}} \tag{9}$$

Where:

ε - effectiveness of heat Exchanger
$\dot{Q}recov_{GHX}$ - gas heat exchanger flux (kW)
$\dot{Q}_{max}$ - maximum heat flux of GHX (kW)

The energy balance for solution heat exchanger was performed under the same criteria, where the only difference is that in SHX the heat is interchanged between the rich and poor solution.

- **Expansion valves:** For these components, mass flow and constant enthalpy are assumed.
- **Evaporator:** The heat lost by the glycol-water mixture (cooling media) is the same that the heat gained by the refrigerant (ammonia) circulated through the evaporator. The heat flux in the evaporator is calculated with the Eq. (10).

$$\dot{Q}_{evap} = \dot{m}_{glycol} \times c_{p-propylene} \times (T_H - T_I \tag{10}$$

Where:

$\dot{Q}_{evap}$ - chiller heat flux (kW)
$\dot{m}_{glycol}$ - glycol mass flow (kg/s)
T_H - inlet chiller temperature (°C)
T_I - outlet chiller temperature (°C)
$C_{p-propylene}$ - glycol-water specific heat (kJ · kg/°C)

- **Absorber:** The heat lost by the ammonia-water mixture in the absorber 1 is taken up by the auxiliary refrigerant system mentioned in the section corresponding to the dephlegmator and is the same process in the absorber 2. To know the heat flux lost in the absorbed the Eq. (11) is used.

$$\dot{Q}_{abs1} = \dot{m}_{Mb} \times (h_{Nb} - h_{Mb}) \tag{11}$$

Where:

$\dot{Q}_{abs1}$ - absorber 1 heat flux (kW)
$\dot{m}_{Mb}$ - ammonia mass flow rate of absorber 1 (kg/s)
h_{Nb} - ammonia specific enthalpy of absorber 1 outlet (kJ/kg)
h_{Mab} - ammonia specific enthalpy of absorber 1 inlet (kJ/kg)

The dephlegmator and both absorbers provide the heat used by the auxiliary refrigerant system.

- **Pump:** To calculate the energy required by the pump, we start with the formula that describes the power absorbed by a pump, where the specific volume and pressure difference are considered. This equals the work of a pump as a change of enthalpy as is shown in Eq. (12). The principle is the same for pump 2.

$$\dot{W}_{pump1} = \dot{m}_8 \times (h_9 - h_8) \tag{12}$$

Where:

$\dot{W}_{pump1}$ - pump 1 mechanical power (kW)
$\dot{m}_8$ - solution mass flow rate (kg/s)
h_9 - solution specific enthalpy pump 1 outlet (kJ/kg)
h_8 - solution specific enthalpy pump 1 inlet (kJ/kg)

The refrigeration system analyzed presents two absorption and generation stages that differ from the common cycle used by the industry (one stage). For this reason, two kinds of cycles were simulated in EES [15] with the same operational conditions defined as input data.

3.2. Model input data

The input data was defined based on operational design conditions. The high pressure of the equipment is 1,700 kPa, ammonia temperature in the evaporator is -12 °C. Consequently the system low pressure corresponds to saturation pressure (267.9 kPa).

The HRHWG deliveries 120 m^3/h of water to generators at 108 °C and the generation system decreases the water temperature down to 80 °C.

The chiller refrigerant (water and glycol) decreases its temperature by 6 °C in the evaporator.

The thermodynamic analysis has been developed focusing on the ammonia-water solution and gas mixture concentration. Common values of rich solution concentration is between 0.35-0.45 [14, 16]. The concentration of the solution at the input of the generator 2 corresponds to a medium concentration (x_{medium}), and it has been defined as a function of the cooling towers capacity (1,250 kW and 3,750 kW). The concentration of the medium solution is 0.36 as is shown in Figure 4.

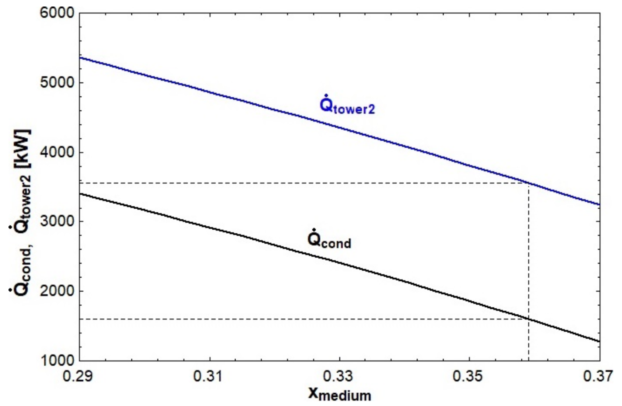

Figure 4. Condenser and Cooling tower 2 heat flux vs. concentration of medium solution.

3.3. Utilization factor of the CHP

The utilization factor of a cogeneration plant is the ratio of the power outputs (thermal energy to the chiller and electrical) respect to the total heat input as is show in Eq. (13).

$$\epsilon_u = \frac{\dot{Q}_{gen1} + \dot{Q}_{gen2} + \dot{W}_{net}}{\dot{Q}_{input}} \tag{13}$$

Where:

ϵ_u - CHP utilization factor
$\dot{Q}_{gen1}$ - generator 1 heat flux (kW)
$\dot{Q}_{gen2}$ - generator 2 heat flux (kW)
$\dot{Q}_{input}$ - CHP total heat input (kW)

The $\dot{Q}_{gen}$ is the thermal energy recovered to use as process heat in the chiller. The $\dot{W}_{net}$ is the net power obtained in gas and vapor turbines and $\dot{Q}_{input}$ is total heat input that corresponds to the heat energy consumed by the reciprocating engines.

3.4. Economics savings respect to a vapor compression refrigeration system.

The reduction of the electric power consumption with the ARS respect to a vapor compression refrigeration system allows obtaining economic savings. The savings have been calculated comparing with a vapor-compression refrigerator that has the same cooling capacity.

The cooling system works 24 hours per day, but according to its main characteristics, it can be assumed that the utilization factor is lower than one because the compressor starts working just when the temperature rises above a certain limit; therefore, as experimental field data, it can be set at 50%.

4. Results and analysis

4.1. Model results

The two-stage cycle lets to recover in a better way the energy from HRHWG water. For this reason, the solution temperature at the principal generator inlet increases and is possible to obtain a richer solution flow with the same available heat from the water.

Table 1. Comparison of one stage versus two stage cycles

	Units	Two stages	One stage
Heat recovered at GEN 1	[kW]	2,954	2,954
Heat recovered at GEN 2	[kW]	800	—
Solution temperature Generator 1 inlet	[°C]	75	65
Evaporator capacity	[kW]	1,6	1,3
COP	—	0.44	0.44

Adding a second absorption and generation stage to the simple absorption cycle increase 23% of refrigeration capacity as is shown in Table 1. The COP is similar for both systems (one and two-stage) but considering that the heat input of the two-stage refrigeration system was recovered from waste energy, it is more advantageous to include one stage more of generation and absorption to increase the cooling capacity.

The concentration of the solution at generator 2's input is the most influential variable in the model. When it presents lower values than 0.36 the COP system increase because of ammonia flow from the generator 2 increases, as is shown in Figure 5, and consequently the evaporator capacity enhances keeping constant the heat required at the ammonia generators.

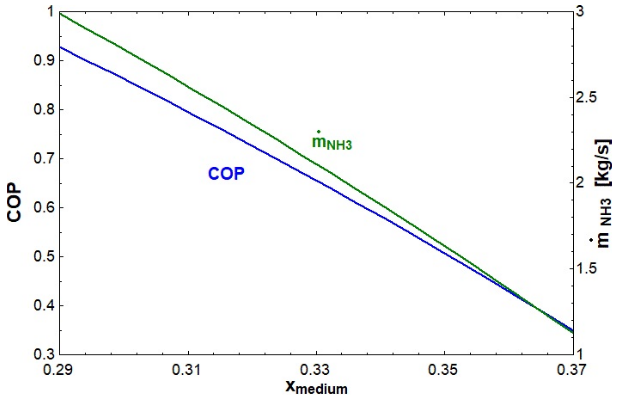

Figure 5. COP and mass flow rate of refrigerant respect to concentration of medium solution.

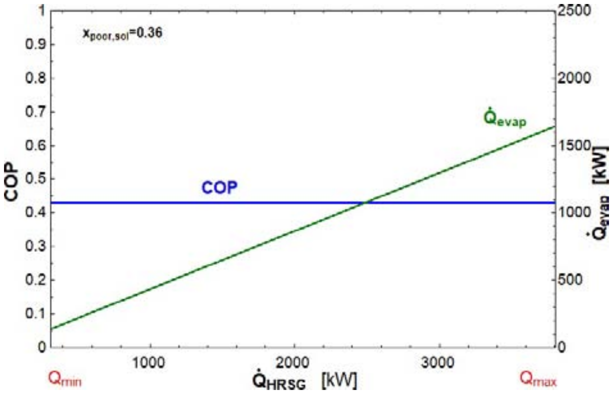

Figure 6. COP and evaporator heat flux respect to the heat recovery in the CHP.

The heat availability is a fundamental issue, and it depends of the engine operating conditions. If the engine is working at maximum load (maximum HRSG and HRHWG capacity), the generator 2 produces a greater ammonia flow and the refrigeration system reaches the maximum capacity (1,600 kW) and it presents 0.43 COP. The COP keeps constant despite heat recovered decreases and the evaporator capacity is reduced as is shown in Figure 6.

The high pressure of the system is an essential operational condition, and it is defined by the geography where the equipment is installed due to the altitude. If the absorption system operates at sea level the evaporator capacity increase and the COP enhance because the heat required by the ammonia generators remains constant as is shown in Figure 7. If the high pressure is higher, the cooling tower capacity (required to dissipate heat from the separators, absorbers, and dephlegmator) increases. For this reason, the cooling tower capacity must to be design based on in situ operational conditions.

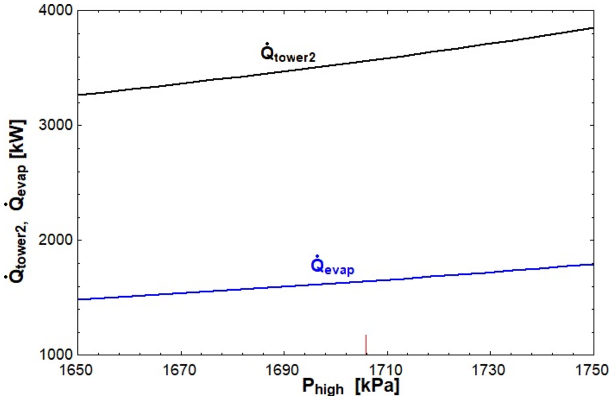

Figure 7. Heat flux in the cooling tower 2 and evaporator respect to high pressure system.

The heat exchangers effectiveness was considered as a constant value of 0.8 [17]. The solution heat exchanger lets to recover heat inside the cycle and increase the solution ammonia-water temperature before it enters to the principal generator. The effectiveness of SHX is directly proportional to the evaporator heat flux and the COP of the system, as is shown in Figure 8. Higher effectiveness SHX represents high investment cost, and it must be evaluated considering that the COP and the cooling capacity increase too.

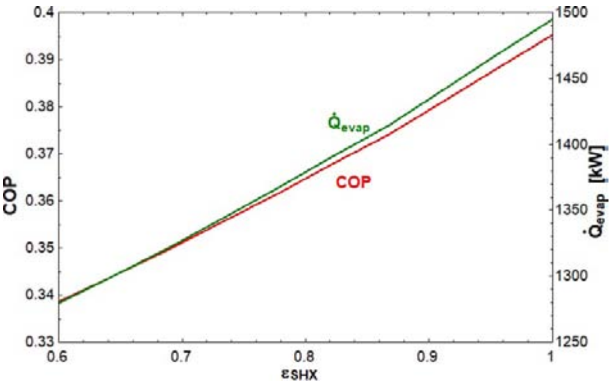

Figure 8. COP and heat flux in the evaporator respect to SHX effectiveness.

4.2. Utilization factor of CHP

The $\dot{Q}_{gen}$ is the heat recovered to use waste energy in the chiller and it is 3.8 MW (t) (obtained by the model). The $\dot{W}_{net}$ is 28.1 MW (e) and corresponds to the net power of the reciprocating engines (8.7 MW (e) per engine) and the vapor turbine (2 MW(e)). The $\dot{Q}_{input}$ is calculated in Eq. (14) with the data sheet information of the Roll Royce engines that reports 7,572 kJ/kWh of specific energy consumption. The utilization factor for the process is calculated with the Eq. (13) and the result is shown in Eq. (15). The input heat flux of CHP is known with kW(f) where f means fuel energy.

$$\dot{Q}_{input} = 3 \times 8,700kw(e)\left(\frac{7,572kJ(f)}{1kWh(e)}\right) \times \frac{1h}{3600s}$$
$$\dot{Q}_{input} = 54,897kW(f) \tag{14}$$

$$\epsilon_u = \frac{3,8MW + (2+8,7\times 3)MW}{54,897MW} = 0,5811 \tag{15}$$

The utilization factor of the cogeneration process is 58.11%, and it means that the process is using a high percentage of the fuel energy that is consumed by the reciprocating engines.

4.3. Estimation of economics savings

The cooling capacity of the two-stage absorption refrigeration (AGO) system obtained with our model is 1,623 kW (t). The electricity that would consume a common vapor compression chiller to obtain the same cooling capacity is calculated in this section to know the economics savings.

The market offers many kinds of machines performing refrigeration with vapor compression cycle. The average performance (COP) is 4.5 [18].

Therefore, it is possible to calculate the mechanical power required by the compressor ($\dot{W}_{comp}$) with Eq. (16).

$$\dot{W}_{comp} = \frac{\dot{Q}_{evap}}{COP} = \frac{1,623kW}{4,5} = 360,67kW(e) \quad (16)$$

The utilization factor for a compression chiller was defined as 50% in the section 3.4 and considering 24 hour per day and 365 days per year, the yearly electricity that would consume by the compression system is 1'579,734.60 kWh/year.

Considering an average energy unit cost (obtained from monthly electricity cost of the two to last year for an industrial rate for Agua Prieta / Mexico [19]) of 0.09 USD/kWh, the avoided electricity cost by the cogeneration system would be 142,000.00 USD/year approximately.

However, considering the possible savings and fixing a payback time of 5 years, the initial investment could be around 710,000.00 USD. It means that the investment is profitable. To obtain more accurate results, it is necessary to acquire specific data.

The efficient cogeneration has several fiscal incentives and preference energy dispatch in different countries (for example Mexico) due to the contribution of technology with the preservation of the environment.

5. Conclusions

It is convenient to use a two-stage absorption system since they allow to exploit better the heat discharged by the engines. Also, the COP of both systems (single and double stage) are similar.

The concentration of the solution at the exit of the generator 1 is the variable assumed to be most influent in the results of the cycle. For this reason, this variable has been chosen according to the capacity of the installed cooling towers. Moreover, it has been observed that if the concentration is close to 0.3 the system COP is close to 1 while it goes down for higher values of concentration.

The COP keeps constant independently from the amount of heat flux entering the system. If the generator is supplied with a higher amount of heat, the mass flow rate of ammonia going to the evaporator increases and consequently refrigeration capacity of the chiller goes up.

The cogeneration process using exhaust gases as heat source for an absorption refrigeration chiller can provide environmental conservation and economic revenues.

References

[1] ASHRAE, *Handbook - Fundamentals. 2009*, inch-pound ed., American Society of Heating, Refrigerating and Air-Conditioning Engineers, Inc., 2009. [Online]. Available: https://goo.gl/X11TGj

[2] C. Moné, D. Chau, and P. Phelan, "Economic feasibility of combined heat and power and absorption refrigeration with commercially available gas turbines," *Energy Conversion and Management*, vol. 42, no. 13, pp. 1559–1573, 2001. [Online]. Available: https://doi.org/10.1016/S0196-8904(00)00157-6

[3] J. Rodríguez-Muñoz and J. Belman-Flores, "Review of diffusion–absorption refrigeration technologies," *Renewable and Sustainable Energy Reviews*, vol. 30, pp. 145–153, 2014. [Online]. Available: https://doi.org/10.1016/j.rser.2013.09.019

[4] K. Ullah, R. Saidur, H. Ping, R. Akikur, and N. Shuvo, "A review of solar thermal refrigeration and cooling methods," *Renewable and Sustainable Energy Reviews*, vol. 24, pp. 499–513, 2013. [Online]. Available: https://doi.org/10.1016/j.rser.2013.03.024

[5] K. E. Herold, R. Radermacher, and S. A. Klein, *Absorption Chillers and Heat Pumps.* CRC Press, 2016, ch. 10. Two-Stage Ammonia/Water Systems, pp. 215–232. [Online]. Available: https://goo.gl/MrMG2m

[6] D. Colorado and W. Rivera, "Performance comparison between a conventional vapor compression and compression-absorption single-stage and double-stage systems used for refrigeration," *Applied Thermal Engineering*, vol. 87, pp. 273–285, 2015. [Online]. Available: https://doi.org/10.1016/j.applthermaleng.2015.05.029

[7] M. Conde, *Thermophysical properties of NH_3 + H_2O Solutions for the industrial design of absorption refrigeration equipment*, Formulation for industrial use. M. Conde Engineering. p. 11. 2004.

[8] S. Said, K. Spindler, M. El-Shaarawi, M. Siddiqui, F. Schmid, B. Bierling, and M. Khan, "Design, construction and operation of a solar powered ammonia–water absorption refrigeration system in saudi arabia," *International Journal of Refrigeration*, vol. 62, pp. 222–231, 2016. [Online]. Available: https://doi.org/10.1016/j.ijrefrig.2015.10.026

[9] Y. Wang, C. Wang, and X. Feng, "Optimal match between heat source and absorption refrigeration," *Computers & Chemical Engineering*, vol. 102, pp. 268–277, 2017. [Online]. Available: https://doi.org/10.1016/j.compchemeng.2016.11.003

[10] S. Du, R. Wang, and X. Chen, "Development and experimental study of an ammonia water absorption refrigeration prototype driven by diesel engine exhaust heat," *Energy*, vol. 130, pp. 420–432, 2017. [Online]. Available: https://doi.org/10.1016/j.energy.2017.05.006

[11] AGO AG. (2017) Cooling from waste heat: efficient energy supply – from small to large-scale industrial projects. AGO AG Energie + Anlage. [Online]. Available: https://goo.gl/id5TYk

[12] V. Chakravarthy, R. Shah, and G. Venkatarathnam, "A review of refrigeration methods in the temperature range 4–300 k." *ASME Journal of Thermal Science and Engineering Applications*, vol. 3, no. 2, pp. 020 801–020 819, 2011. [Online]. Available: http://doi.org/10.1115/1.4003701

[13] R. J. Dossat, *Principios de Refrigeración*. Compañía Editorial Continental, 1980. [Online]. Available: https://goo.gl/CG3Tbg

[14] P. Srikhirin, S. Aphornratana, and S. Chungpaibulpatana, "A review of absorption refrigeration technologies," *Renewable and Sustainable Energy Reviews*, vol. 5, no. 4, pp. 343–372, 2001. [Online]. Available: https://doi.org/10.1016/S1364-0321(01)00003-X

[15] F-chart software. (2016) Engineering Equation Solver (EES). [Online]. Available: https://goo.gl/sYqcRc

[16] Y. Fan, L. Luo, and B. Souyri, "Review of solar sorption refrigeration technologies: Development and applications," *Renewable and Sustainable Energy Reviews*, vol. 11, no. 8, pp. 1758–1775, 2007. [Online]. Available: https://doi.org/10.1016/j.rser.2006.01.007

[17] S. Steiu, D. Salavera, J. C. Bruno, and A. Coronas, "A basis for the development of new ammonia–water–sodium hydroxide absorption chillers," *International Journal of Refrigeration*, vol. 32, no. 4, pp. 577–587, 2009. [Online]. Available: https://doi.org/10.1016/j.ijrefrig.2009.02.017

[18] F. Kreith, S. Wang, and P. Norton, *Air conditioning and refrigeration engineering*. CRC Press, 1999. [Online]. Available: https://goo.gl/675PxJ

[19] SENER. (2017) Precios medios de energía eléctrica por tipo de tarifa. Secretaría de Energía. México. [Online]. Available: https://goo.gl/sz22NF

Scientific Paper / Artículo Científico

UNIVERSIDAD POLITÉCNICA SALESIANA ECUADOR
INGENIUS
Revista de Ciencia y Tecnología
https://doi.org/10.17163/ings.n21.2019.05
pISSN: 1390-650X / eISSN: 1390-860X

THE WATER-ENERGY NEXUS: ANALYSIS OF THE WATER FLOW OF THE COCA CODO SINCLAIR HYDROELECTRIC PROJECT

NEXO AGUA – ENERGÍA: ANÁLISIS DEL FLUJO HÍDRICO DEL PROYECTO HIDROELÉCTRICO COCA CODO SINCLAIR

Sebastián Jiménez-Mendoza[1], Francisco Terneus-Páez[1,2,*]

Abstract

This article analyzes the interrelation between water and energy, taking as a case the analysis of the water flow of the Coca Codo Sinclair Hydroelectric Project. It investigates the case of this emblematic project, where the water used for consumption would decrease the inflow to the driving tunnel, which would risk its power generation capacity. A bibliographic research is used for this purpose. It is concluded that the Chalpi Grande project and the subsequent phases of the Ríos Orientales; and the Cayambe Pedro Moncayo irrigation projects and the Pesillo Imbabura potable water would reduce the inflow rate by up to 11% and, therefore, their energy production, demonstrating the need to plan the use of these resources considering their nexus.

Keywords: Water-energy nexus, Coca Codo Sinclair Hydroelectric Project, consumptive use of water.

Resumen

Este artículo analiza la interrelación existente entre el agua y la energía, tomando como caso el análisis del flujo hídrico del Proyecto Hidroeléctrico Coca Codo Sinclair. Investiga el caso de este proyecto emblemático, donde los usos consuntivos del agua disminuirían el caudal de entrada al túnel de conducción, arriesgando con esto su capacidad de generación eléctrica. Se utiliza para ello una investigación de tipo bibliográfica. Se concluye que el proyecto Chalpi Grande y las fases siguientes de ríos orientales; y los proyectos de riego Cayambe-Pedro Moncayo y de agua potable Pesillo-Imbabura afectarían el caudal de entrada hasta en un 11 % y con ello su producción de energía, con lo cual queda en evidencia la necesidad de planificar el aprovechamiento de estos recursos considerando su nexo.

Palabras clave: Nexo agua – energía, Proyecto Hidroeléctrico Coca Codo Sinclair, uso consuntivo del agua.

[1,*] Department of Energy and Mechanics, Universidad de las Fuerzas Armadas ESPE, Sangolquí, Ecuador http://orcid.org/0000-0001-7031-5954

[2] Doctorate Program in Technological Management – Escuela Politécnica Nacional, Quito, Ecuador.
Autor para correspondencia ✉: cfterneus@espe.edu.ec http://orcid.org/0000-0001-5372-0288

Received: 02-10-2018, accepted after review: 30-11-2018

Suggested citation: Jiménez-Mendoza, S. y Terneus-Páez, F. (2019). «The water-energy nexus: Analysis of the water flow of the Coca Codo Sinclair Hydroelectric Project». INGENIUS. N.°21, (january-june). pp. 53-62. DOI: https://doi.org/10.17163/ings.n21.2019.05.

1. Introduction

The water-energy-food nexus has been under discussion since the Bonn Conference in 2011, in which it was recommended that these resources are considered in an integrated fashion, and concentrating in assuring that the interdependence between them is explicitly identified in decision making [1]. Three years later, during the Global Water Security & Sanitation Partnership (GWSP) conference, the research and political communities around the world issued a call to develop strategies to address this nexus in a comprehensive manner [2]. With the current growth rate of the world population, the agricultural sector faces the challenge of doubling the production of food for 2050 [3]. About 71% of worldwide water withdrawals are due to such sector [4]. Since for 2050 it will be required 55% more water to increase the generation of electricity and to meet consumption of households, it is projected that more than 40% of world population will live under severe hydrological stress [5]. Nevertheless, few authors have addressed the issue of how to turn the mainly theoretical concept of the water-energy-food nexus, into practical evaluation approaches. Albretch *et al.* [6] state that, despite the promising conceptual approach, the use of the aforementioned nexus to systematically evaluate the connection of the resources has been limited. Middleton *et al.* [7] mention that the water-energy-food nexus has not been practically integrated yet. Similarly, Leck *et al.* [8] ask for the practical application of such nexus in future scientific research work.

Denise Lofman *et al.* [9], regarding the nexus between water and energy, state that it will be difficult to simultaneously fulfill the needs of the users and protect these valuable resources, regarding agricultural, industrial and residential issues. Pittock Jamie *et al.* [10] showed the significant influence of the nexus between the supply of hydroelectric energy and food on the water basin. According to Fisher *et al.* [11], the water-energy nexus for the generation of electricity causes more severe problems such as pollution and CO_2 emission. Lubega *et al.* [12] state that it is possible to measure the water energy nexus using models that relate electric energy and municipal water consumption.

Various current trends raise the urgency to address the water-energy nexus in an integrated and proactive manner. In the first place, climate change has begun to affect precipitation and temperature patterns. Secondly, population growth and regional migration trends indicate that it is probable that there is an increase in the number of inhabitants in arid zones. At last, new technologies in the energy and water fields may change the demand of these resources [13].

According to the International Energy Agency [14], worldwide water consumption will increase 60% by 2040, thus affecting hydroelectric plants whose water withdrawals will raise less than 2%. Due to the population growth and the modifications in the feeding patterns, food consumption is increasing in almost all regions on earth. It is expected that for 2050 it will be necessary to produce 200 million tons of meat and 1 billion additional tons of cereal to fulfill the increasing food demand. For this reason, agriculture is responsible for 90% of the consumptive use of water [15].

As a consequence of the aforementioned global issues, Ecuador is in the need of addressing and planning the use of its hydrological resources. Article 30 of Ecuador's Law of Hydrological Resources states that: "The State and its institutions in the scope of their competences are responsible of the integrated administration of the hydrological resources in each basin. As a consequence, they are obligated to regulate the uses of water, and take actions to preserve its quantity and quality by means of a sustainable management based on technical regulations and quality parameters" [16].

On the other hand, article 313 of Ecuador's Constitution states that: "The State reserves the right to administer, regulate, control and manage strategic sectors; energy in all forms are considered strategic sectors. . . " [17]. The purpose of this paper is to analyze the case of the Coca Codo Sinclair Hydroelectric Project CCSHP), as an example of the nexus between water and energy, where the consumptive uses of water would reduce the inflow to the transmission tunnel, thus putting at risk electric generation capacity of this emblematic project.

The rest of the paper is structured as follows. Section 1.1 presents a historical overview of the CCSHP, and section 2 (methodology) discusses reports of feasibility and projects that make consumptive use of water. In addition, section 3 analyzes how such projects would affect the inflow to the CCSHP and, at last, section 4 concludes showing the need of planning the water-energy nexus in an integrated manner.

1.1. The Coca Codo Sinclair Hydrolectric Project

The CCSHP is a construction considered as emblematic by the Ecuadorian government. It was built in the origin of the Coca River, in the province on Napo [18]. It was named after the North American geologist Joseph Sinclair who, when going through the such river in the east of Ecuador, identified a sharp curve later called Codo (elbow) Sinclair by local people. This researcher stated that in this place the river had the potential to generate electric energy [19].

The CCSHP was one of the most important projects of the National Electrification Plan, in the basin of the Quijos and Coca Rivers, during the 1970s and 1980s. The Ecuadorian Institute of Electrification (INECEL, Instituto Ecuatoriano de Electrificación) was the company in charge of conducting the studies associated to the project. In particular, two studies were carried out in 1976: pre-feasibility by the Brazilian company Hidroservice, and total available capacity by the Italian consulting companies Electroconsult and Rodio, the Belgian Tractionel and the domestic Ingeconsult, Inelin, Astec y Caminos y Canales [20].

In order to optimize the selected alternative, a feasibility design was carried out between April 1990 and June 1992, corresponding to two continuous stages that would generate a power of 432 (MW) and 427 (MW), respectively, for a total of 859 (MW). This study included adjustments to the project because of an earthquake close to the volcano Reventador in March 1987, which significantly changed the face of the land. The State modified such study in 2007, and redesigned the project to reach a power of 1500 MW [18].

The CCSHP was announced in January 15 2007, being considered of high national interest, and it was included in the Master Plan of Electrification. In that year, two companies were in charge of managing the project: the National Council of Electricity (Conelec) during the first trimester, and the Minister of Electricity and Renewable Energies (MEER) in July. Nevertheless, it is important to remark that the company Termopichincha, of the Ecuadorian State, was designated as the operator of the project in September 2007. Later, Termopichincha and the Argentinian company ENARSA constituted the Consortium Coca Sinclair S.A. [20].

The studies were approved by Conelec in 2008. The hydroelectric company Coca Codo Sinclair S.A. from Quito, put the consulting company ELC-Electroconsult, from Milan, Italy, in charge of the conceptual redesign studies to reach 1500 MW. In 2009 ELC-Electroconsult presented the corresponding final feasibility study. Then, Coca Codo Sinclair S.A. hired SINOHYDRO to do the engineering, and it started the construction [20]. Six years later, on November 18 2016, the CCSHP was inaugurated.

Once the construction was finalized, the CCSHP is constituted by: a water catchment dam with a maximum height of 31.8 m; a spillway with a diversion dam of 13.5 m high and a net width of 160 m; a sand removal equipment with 8 chambers; a 24.8 km long transmission tunnel, with excavation and interior diameters of 9.1 m and 8.2 m, respectively, and a design diameter of 222 m^3/s; a compensating reservoir which comprises a rock-fill dam with a concrete wall of 58 m high, corresponding to a reservoir with a usable volume of 800000 m^3; two 1400 m long concrete pressure pipes with internal diameters of 5.8 and 5.2 m, respectively, a design flow of 139.25 m^3/s) each, and a steel coating in their final section, carry the water from the compensating reservoir to the powerhouse; the powerhouse is a cavern of dimensions 26 × 46.8 × 219.5 m excavated in rock, containing 8 vertical shaft Pelton turbines each with 6 injectors and a power of 187.5 MW, which turbinate the water of the Coca River, that forms where the Quijos and Salado Rivers meet, as can be seen in Figure 1 [21].

Figure 1. Location of the CCSHP [22].

The installed power of a hydroelectric plant, also known as effective nominal power is given by [23].

$$Pi = \eta t \times \eta g \times \eta tr \times \lambda \times Q \times H \tag{1}$$

Where:

Pi = Effective nominal power (W)
Q = Flow rate entering the pressure pipe (m^3/s)
H = Nominal net height (m)
ηt = Efficiency of the Pelton turbine
ηg = Efficiency of generator
ηtr = transformer efficiency

The data taken from appendix f of the feasibility report of the CCSHP by ELC-Electroconsult [24] are.

H = 604,1 (m)
P = 1500 (MW)
ηt = 91 %
ηg = 97,52 %
ηtr = 99,5 %

Substituting these values in equation (1) and solving for Q results in:

$$Pi = \eta t \times \eta g \times \eta tr \times 9,81 \times Q \times H \times 1000$$

$$Q = \frac{Pi}{\eta t \times \eta g \times \eta tr \times 9,81 \times H \times 1000}$$

$$Q = \frac{1500000000}{0,91 \times 0,9752 \times 0,995 \times 9,81 \times 604,1 \times 1000}$$

$$Q = 286,6 (m^3/s)$$

Since the CCSHP is a run-of-river plant with daily regulation [24], the turbinated flow to generate 1500 MW, i.e. the flow that should enter the two pressure pipes, is 286.6 m^3/s, i.e. 143.3 m^3/s each. According to Synohidro Corporation, (2009), the CCSHP only can generate this power during four hours daily, however, the design flow rate of the pressure pipes is 139.25 m^3/s, namely 278.5 m^3/s both [24].

In 2017, after one year of operation, the CCSHP had produced 66.7% of the expected energy. Between January and December, the plant contributed a total of 5838 GWh to the national interconnected system, below the expected average generation of 8734 GWh [25].

2. Materials and methods

This research is bibliographic, with a descriptive scope. The feasibility studies presented by Inecel in 1992, which shows the historic behavior of the Coca River flow, and by ELC-Electroconsult, which redesigns the study by Inecel, were analyzed. In addition, the projects that would affect the flow coming into the CCSHP, because of the consumptive uses of water, were examined.

2.1. Feasibility studies

In the following, two feasibility reports of the CCSHP will be analyzed. The first one was carried out by Inecel and approved in 1992, and the second was conducted by ELC-Electroconsult and approved in 2009.

2.1.1. Feasibility study of 1992

This feasibility study was carried out by Inecel. To calculate the flow rates of the project, historic data from 1972 to 1987 was considered for the San Rafael cascade and for the Coca River in the El Salado sector [18]. Since the study was conducted in the same river station for an interval of fifteen to twenty years, which include dry, typical and rainy periods, this methodology is widely accepted [26]. Figure 2 illustrates the curve obtained by Inecel, showing the general duration of daily flow rates in El Salado [19]. On the other hand, Figure 3 shows the monthly average flow rates recorded in the Coca River station, in the El Salado sector, along the aforementioned periods.

This way Inecel determined that the average flow rate in the El Salado sector is 292 m^3/s, after taking out 3 m^3/s that were used by the aqueduct Papallacta-Quito, which corresponds to a specific contribution greater than 80 $l/s/km^2$. The steady daily flow rate of 127 m^3/s is guaranteed 90% of the time [18].

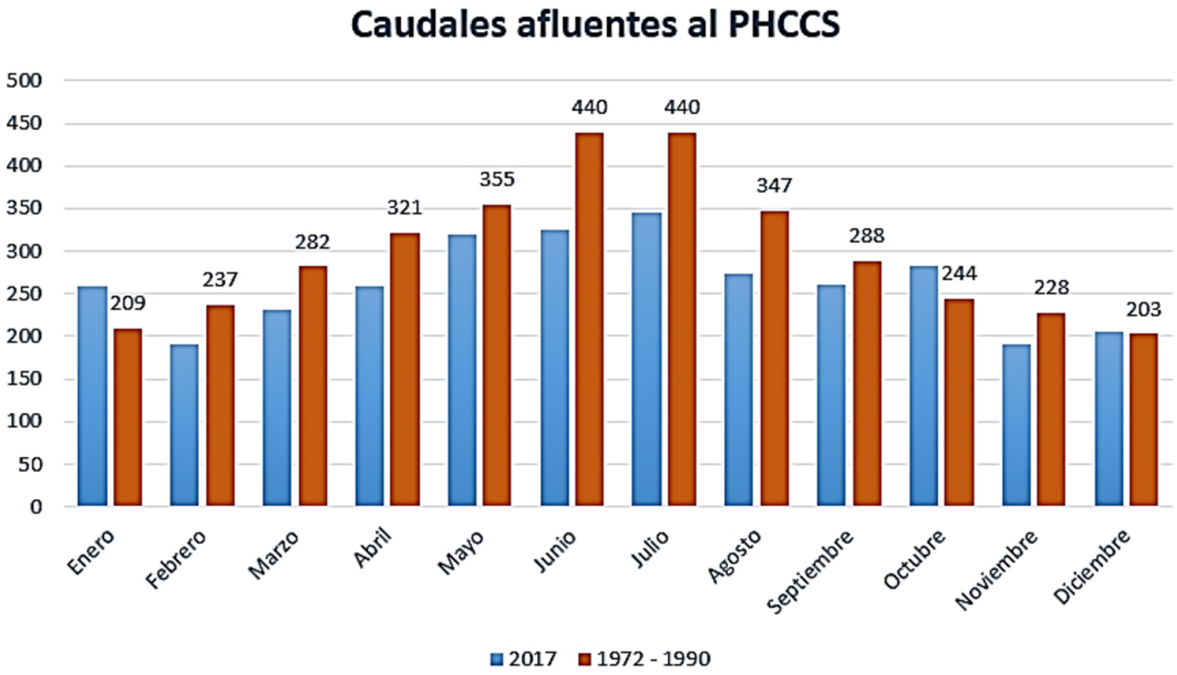

Figure 2. Comparison between the flow rates of the period 1972-1990 and 2017.

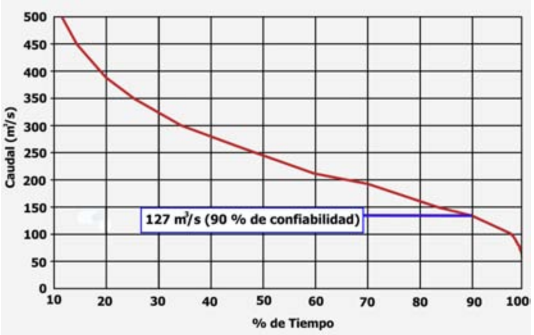

Figure 3. Curve of general duration of daily flow rates in El Salado [19].

The Inecel company decided that the flow rate should be captured in two stages, the first of 63.5 m^3/s and the second of another 63.5 m^3/s, thus reaching a total of 127 m^3/s. In both stages the plant capacity factor remained equal to 0.8 [21].

2.1.2. Current feasibility study of the CCSHP

The current feasibility study of the CCSHP was carried out by ELC-Electroconsult, and was based in the hydrological study conducted by Inecel in 1992, which recorded the historic flow rate of the Coca River [21].

ELC-Electroconsult pointed out that in order to generate the 1500 MW installed in the powerhouse, keeping the same losses of the feasibility study, a flow rate of 278.5 m^3/s is required in the pressure pipe, which corresponds to a flow rate of 222.7 m^3/s entering the compensating reservoir. Subtracting an average flow rate of 0.7 m^3/s from Granadilla creek, leaves a flow rate of 222 m^3/s, which will be directed from the El Salado site to the dam through the transmission tunnel [21].

In order to obtain a maximum flow rate of 278.5 m^3/s in the pressure pipe while maintaining a plant capacity factor of 0.8, it was required to increase from 460000 m^3 to 800000 m^3 the usable volume of the compensating reservoir, keeping the same minimum and maximum levels, i.e. 1229.50 y 1216 meters above mean sea level (mamsl), respectively [21].

On the other hand, CENACE has the information shown in Table 1, about the flow tributary to the compensating reservoir of the CCSHP. Figure 3 also shows the monthly average flow rates in the Coca River station corresponding to 2017; it can be seen that these rates are smaller than the historically obtained during the period 1972-1990.

It is important to consider the significant changes undergone by the face of the sector, mainly due to the construction of the road between Valle de Quijos and Lago Agrio handed in 1972, which promoted the colonization of the sector. This caused the transformation of the forest area into pastures and the wood exploitation, which surely affected the climatic conditions of this river basin and the flow of its rivers [27]. The latter were also affected by the consumptive uses of water.

Table 1. Flow rate tributary to the compensating reservoir of the CCSHPS [25]

Menths	Flow rate (m^3/s)	
	2016	**2017**
January	-	258,75
February	-	190,21
March	-	230,37
April	-	258,11
May	697,9	320,35
June	707,38	324,84
July	560,6	344,57
August	506,23	272,94
September	394,34	259,8
October	298,5	283,55
November	148,03	190,05
December	135,89	205,16

2.2. Consumptive uses of water

According to the Organic Law of Hydrological Resources and Water Utilization, a consumptive use is one in which the water is not returned to the site from which it was withdrawn, nor in the same way in which it was removed [16]. This kind of use can be identified in four projects as shown in Figure 4: one already existing, two under construction and one scheduled. These projects, which capture or will capture the water from the flow entering the CCSHP, are the following:

Existing:

- Papallacta Project from the Public Metropolitan Company of Potable Water and Sanitation, of Quito Metropolitan District (EPMAPS).

Under construction:

- Chalpi Grande Project or phase one of the Ríos Orientales Project (Proyecto Ríos Orientales, PRO) of the EPMAPS.
- Cayambe-Pedro Moncayo Irrigation and Pesillo-Imbabura Potable Water Project.

Scheduled:

- Future phases of the Ríos Orientales Project (PRO) of the EPMAPS.

Each of these projects is now described.

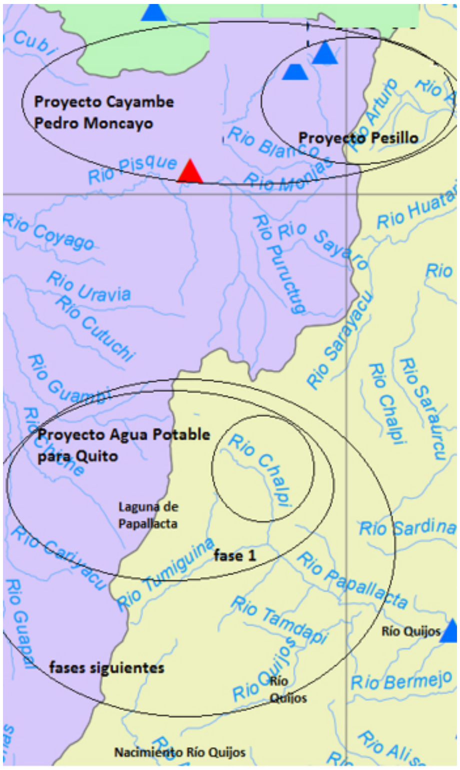

Figure 4. Location of the projects under construction [28].

2.2.1. Papallacta Project

This project was inaugurated in 1990 by the EPMAPS, and consisted of supplying potable water to the city of Quito, in the province of Pichincha. In a sentence on September 22 1987, by means of the concession under trial number 1503, the company obtained authorization to capture the flow from rivers Papallacta, Chalpi Grande, Tuminguina and Blanco Chico, with rates of 1.70 m^3/s, 3.20 m^3/s, 2.20 m^3/s and 0.90 m^3/s, respectively [29, 30].

For the feasibility studies of the CCSHP a value of 3 m^3/s was taken into account; however, the concession granted to EPMAPS considered 8 m^3/s [30].

2.2.2. Ríos Orientales Project (PRO)

The growing demand of potable water in the city of Quito was analyzed in the 1970s; fulfilling such demand required the implementation of new projects, as well as reducing unaccounted losses and per capita consumption. EPMAPS decided to design some projects, the most important of which was the Ríos Orientales Project (PRO) that would supply water to the Metropolitan District of Quito and to its 22 rural parishes beyond year 2055, by means of the capture, gravity transmission and treatment of 31 rivers. The PRO would use water from the hydrological basins of rivers Valle Vicioso, Antisana, Cosanga, Quijos and Papallacta, located along Quijos and Archidona cantons in the province of Napo [31]. On January 16 2002, by through concession under trial number 296-96-CTD [29], EPMAPS obtained authorization from former National Council of Hydrological Resources (CNRH), now Senagua, to capture the waters from the rivers that would feed the project, which are summarized in Table 2 [31].

Table 2. Flow rates approved by the CNRH to EPMAPS in January 2002 [31]

River	Flow rate (m^3/s)
Río Valle Vicioso	5,01
Río Tolda	0,74
Río Chuzalongo	0,3
Río Bajo	0,16
Río Antisana	4,49
Río Javas	0,71
Río Cosanga	1,13
Río Quijos Sur	2,14
Río Quijos Norte	1,36
Río Blanco Grande	1,19
Total	**17,23**

Based on technical, economic-financial and environmental aspects, construction of the Ríos Orientales Project (PRO) would be executed in phases as illustrated in Figure 5 [32]. The first phase would use the concession granted in 1987, while the second and future stages would use the concession of 2002, which was summarized in Table 2.

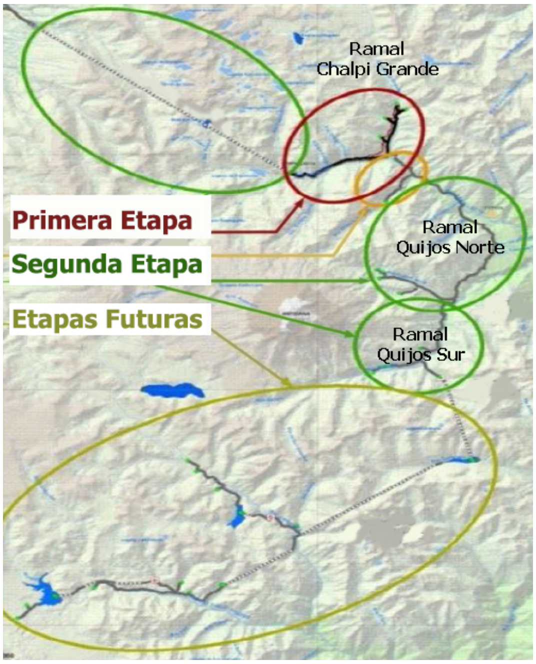

Figure 5. Phases of the Ríos Orientales Project [33]

The first phase, which is Ramal Chalpi Grande-Papallacta, comprises a canal that will capture a total flow of 2.21 m^3/s from tributaries Chalpi A (1.23 m^3/s), Encantado (0.64 m^3/s), Chalpi B (0.27 m^3/s) y Chalpi C (0.07 m^3/s), that constitute Chalpi Grande River, as shown in Figure 6, and transfers it to the reservoir in Papallacta [33].

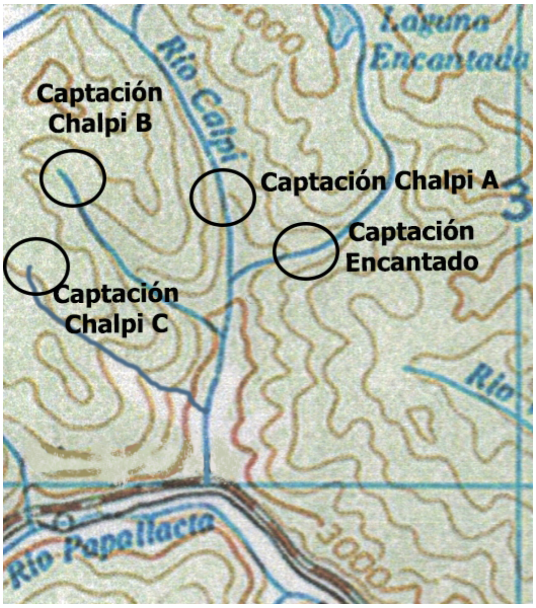

Figure 6. Phase 1 of PRO [34].

In July 2018, the manager of the EPMAPS pointed out that the project exhibited a progress of 26%, and will be finalized in 2021 [35].

The second phase, which is Ramal Quijos-Papallacta-Paluguillo, will start in 2040 and is intended to capture a total flow of 4691 m^3/s from rivers Quijos Norte, Tablón, Cristal, Pucalpa, Azufrado, Semiond, Quijos Sur and Blanco Grande [36].

The future phases will start in 2041, and are intended to obtain flow from rivers Cosanga, Antisana, Valle Viscoso and their tributaries [32].

2.2.3. Cayambe-Pedro Moncayo Irrigation and Pesillo-Imbabura Potable Water Project

The purpose of this project is to capture water from rivers Arturo, Boquerón, San Pedro, San Jerónimo and Montoneras, through the headrace tunnels that connect Arturo River with Boquerón River, Boquerón River with San Pedro River, and San Pedro River with La Rápida River, as shown in Figure 7 [37]. In the first trial, the 220-96, the Resolution enacted by Quito Water Agency in April 15 1999 favored the Pichincha Provincial Government, who got the right to use the waters from rivers Azuela, Arturo, Boquerón and San Pedro, for a total flow rate of 3325 m^3/s [38].

Figure 7. Location of the Cayambe-Pedro Moncayo and Pesillo-Imbabura Project ([33]).

In the second trial, the 1375-00, the Quito Water Agency granted the Pichincha Provincial Government the right to use the waters from rivers San Jerónimo, Montoneras, La Chimba and their tributaries. Among these rivers, only the first two affect the flow of Salado River that feeds CCSHP, with flow rates of 0.24 m^3/s and 0.08 m^3/s, respectively. In addition, Quito Water Agency granted the Imbabura Provincial Government the right to use the waters from rivers Montoneras and San Jerónimo, with flow rates of 0.1 m^3/s and 0.31 m^3/s, respectively [39]. Such flow rates together with the corresponding to rivers Arturo, Boquerón and San Pedro, which also flow into El Salado and were considered in the previous concession, add up to a total of 4.06 m^3/s [39].

On December 13 2017, the director of the Cayambe-Pedro Moncayo Irrigation and Pesillo-Imbabura Potable Water Project announced that it has a progress of 95.6 % [37].

3. Results and discussion

Figure 8 summarizes the past and future events that will affect the flow of the CCSHP.

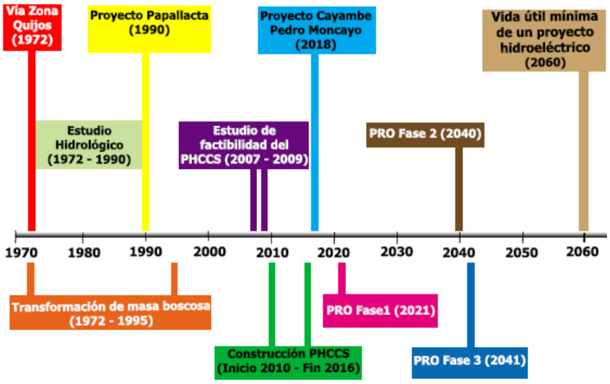

Figure 8. Chronology of events that affect the flow of the CCSHP.

From the analysis of the three projects, it follows that 20 m^3/s should be subtracted from the flow rate of Coca River in the El Salado Sector, due to the ecological flow (ELC-Electroconsult, 2009), and in the near future flow rates of 4.06 m^3/s from the Cayambe-Pedro Moncayo and Pesillo-Imbabura Project (for 2018) and of 2.21 m^3/s from Chalpi Grande Project, which correspond to phase one of PRO, should also be subtracted. Nevertheless, the concession of 1987 authorizes the use of up to 5 m^3/s, considering that 3 m^3/s have been already used in the Papallacta Project. At last, a total of 17.2 m^3/s corresponding to the second and third phases of PRO should be considered, which would initiate in 2040 and 2041, respectively. Table 3 explains in more detail the projects that would reduce the flow rate of the CCSHP. It should be considered that the service life of a hydroelectric project is generally 50 to 75 years [39].

Table 3. Projects that affect the flow of the CCSHP

Name	**Year**	**Flow rate (m^3/s)**
Ecological flow	2016	20
Irrigation project Cayambe-Pedro Moncayo and drinking water Pesillo-Imbabura	2018	4,06
Papallacta and PRO project (phase 1)	2021	≈ (2,21-5,00)
PRO (phase 2 and phase 3)	2040-2055	17,23
Total		≈ (23,5-26,29)

As it can be seen in Table 3, the inflow to the CCSHP would be reduced by a maximum of 26.29 m^3/s, which is equivalent to 11% of the design flow rate. Since the CCSHP is a run-of-river plant with daily regulation, such flow reduction would affect the generation of electricity in a similar percentage.

4. Conclusions

The energy generation capacity of the Coca Codo Sinclair Hydroelectric Project would be affected by the reduction of 222 m^3/s on the inflow, because of the future consumptive uses of water by the EPMAPS, due to the Chalpi Grande Project and the subsequent phases of the Ríos Orientales Project, which would take up to 2.2 m^3/s and 17.2 m^3/s, respectively. The flow utilized by the Cayambe-Pedro Moncayo Irrigation and Pesillo-Imbabura Potable Water Project, which is expected to finalize in 2018 and has a granted concession of 4.06 m^3/s, should be reduced as well. In the future, the flow entering the SSCHP would be reduced in up to 11%, thus affecting the generation of electricity. Therefore, it becomes evidently necessary to plan ahead the use of these resources considering their nexus.

References

[1] H. Hoff, "Understanding the nexus. background paper for the bonn2011 conference: The water, energy and food security nexus," in *Stockholm Environment Institute, Stockholm*, 2011. [Online]. Available: https://goo.gl/aiCG9J

[2] GWSP, "Sustainability in the water–energy–food nexus," in *International Conference. Global Water System Project*, 2014. [Online]. Available: https://goo.gl/CQjWTX

[3] OECD, *Sustainable Management of Water Resources in Agriculture*. Organisation for Economic Co-operation and Development, 2010. [Online]. Available: https://doi.org/https://doi.org/10.1787/9789264083578-en

[4] McKinsey&Company, "Charting our water future. economic frameworks to inform decision-making," 2030 Water Resources Group, Tech. Rep., 2009. [Online]. Available: https://goo.gl/XEWfc3

[5] WWAP (United Nations World Water Assessment Programme), "The united nations world water development report 2014: Water and energy," Paris, UNESCO., Tech. Rep., 2014. [Online]. Available: https://goo.gl/LFGg6d

[6] T. R. Albrecht, A. Crootof, and C. A. Scott, "The water-energy-food nexus: A systematic review of methods for nexus assessment," *Environmental Research Letters*, vol. 13, no. 4, pp. 1–26, 2018. [Online]. Available: https://doi.org/10.1088/1748-9326/aaa9c6

[7] C. Middleton, J. Allouche, D. Gyawali, and S. Allen, "The rise and implications of the water-energy-food nexus in southeast asia through an environmental justice lens," *Water Alternatives*, vol. 8, no. 1, pp. 627–654, 2015. [Online]. Available: https://goo.gl/JKikGy

[8] H. Leck, D. Conway, M. Bradshaw, and J. Rees, "Tracing the water–energy–food nexus: Description, theory and practice," *Geography Compass*, vol. 9, no. 8, pp. 445–460, 2015. [Online]. Available: https://doi.org/10.1111/gec3.12222

[9] IEA, *Water energy nexus*. International Energy Agency. Secure Sustainable Together, 2016. [Online]. Available: https://goo.gl/DGsKrf

[10] D. Lofman, M. Petersen, and A. Bower, "Water, energy and environment nexus: The california experience," *International Journal of Water Resources Development*, vol. 18, no. 1, pp. 73–85, 2002. [Online]. Available: https://doi.org/10.1080/07900620220121666

[11] J. Pittock, D. Dumaresq, and A. M. Bassi, "Modeling the hydropower–food nexus in large river basins: A mekong case study," *Water*, vol. 8, no. 10, p. 425, 2016. [Online]. Available: https://doi.org/10.3390/w8100425

[12] F. Ackerman and J. Fisher, "Is there a water–energy nexus in electricity generation? long-term scenarios for the western united states," *Energy Policy*, vol. 59, pp. 235–241, 2013. [Online]. Available: https://doi.org/10.1016/j.enpol.2013.03.027

[13] W. N. Lubega and A. M. Farid, "An engineering systems model for the quantitative analysis of the energy-water nexus," in *Complex Systems Design & Management*, M. Aiguier, F. Boulanger, D. Krob, and C. Marchal, Eds. Cham: Springer International Publishing, 2014, pp. 219–231. [Online]. Available: https://doi.org/10.1007/978-3-319-02812-5_16

[14] U.S. Department of Energy, "The water-energy nexus: Challenges and opportunities," Tech. Rep., 2014. [Online]. Available: https://goo.gl/Q8ABT5

[15] Asamblea Constituyente, *Capítulo quinto. Sectores estratégicos, servicios y empresas públicas. Art. 313.* República del Ecuador, 2008. [Online]. Available: https://goo.gl/hFdWQm

[16] ENTRIX, *Estudio de impacto ambiental preliminar del Proyecto Hidroeléctrico Coca Codo Sinclair.* ENTRIX. Consultora Ambiental, 2008. [Online]. Available: https://goo.gl/zvSdEZ

[17] Asamblea Nacional, *Ley Orgánica de Recursos Hídricos, Usos y Aprovechamiento del Agua.* República del Ecuador. Secretaría del Agua, 2014. [Online]. Available: https://goo.gl/idEuHH

[18] Y. Granda Paladines, *Estudio experimental en modelo hidraúlico físico sobre la optimización de la bocatoma del Proyecto Coca-Codo-Sinclair.* Tesis de Grado. Escuela Politécnica Nacional, 1992. [Online]. Available: https://goo.gl/q1RPsG

[19] V. López, "Implicaciones del proyecto Coca Codo Sinclair para la amazonía ecuatoriana," FLACSO, Tech. Rep., 2014. [Online]. Available: https://goo.gl/mP2PEx

[20] CENACE, *Informe anual 2017.* Operador Nacional de Electricidad. Ministerio de Electricidad y Energía Renovable., 2017. [Online]. Available: https://goo.gl/Hc9wsB

[21] G. Rodriguez. (2014) El proyecto coca codo sinclair: un lazo internacional hacia el desarrollo del ecuador. Blog Ecuador hacie el desarrollo. [Online]. Available: https://goo.gl/sC2mkt

[22] a. Robles and I. Fernández, *Centrales de Generación de Energía Eléctrica.* Universidad de Cantabria, 2012.

[23] Sinohydro Corporation, *Contrato para el desarrollo de ingeniería para el Proyecto Hidroeléctrico Coca Codo Sinclair*, 2009. [Online]. Available: https://goo.gl/JcQWea

[24] C. Mataix, *Mecánica de fluidos y máquinas hidráulicas.* Ediciones del Castillo S. A., 1986. [Online]. Available: https://goo.gl/4FZiEH

[25] CELEC, *Proyecto Hidroeléctrico Coca Codo Sinclair rediseño Conceptual para 1500 MW,.* Corporación Eléctrica del Ecuador. Coca Codo Sinclair, 2009.

[26] J. E. Grijalva, *Expansión y trayectorias de la ganadería en la Amazonía: estudio en el Valle de Quijos y Piedemonte, en Selva Alta. Ecuador*, 2004. [Online]. Available: https://goo.gl/gf9vZL

[27] INAMHI, *Mapa de ubicación de la red hidrológica en operación por cuencas hidrográficas del Ecuador.* Instituto Nacional de Meteorología e Hidrología. Ecuador., 2007. [Online]. Available: https://goo.gl/onJ7Qw

[28] GAD Papallacta, *Plan de desarrollo y ordenamiento territorial gobierno autónomo descentralizado parroquial de Papallacta*, 2015. [Online]. Available: https://goo.gl/EvKSKM

[29] Secretaría del Agua, *Resolución 2013-16-EPMAPS-Q.*, 2013. [Online]. Available: https://goo.gl/EhTFGG

[30] Ministerio del Ambiente, *Plan de Manejo Adaptativo de la parte alta de la Reserva Ecológica Antisana.* Ecuador, 2011. [Online]. Available: https://goo.gl/h1EXh1

[31] EPMAPS, *Primera etapa del proyecto de agua potable ríos orientales ramal Chalpi Grande – Papallacta. 2017.* Empresa Pública Metropolitana de Agua Poitable y Saneamiento. Alcaldía de Quito. Ecuador, 2017. [Online]. Available: https://goo.gl/D1RMZs

[32] ——, *Estudios de factibilidad y diseños definitivos del proyecto de agua potable ramal Chalpi grande – Papallacta y central hidroeléctrica Chalpi grande.* Empresa Pública Metropolitana de Agua Poitable y Saneamiento. Alcaldía de Quito. Ecuador, 2014.

[33] Alcaldía de Quito, *Quito tendrá abastecimiento de agua hasta el 2040 con el "Ramal Chalpi Grande – Papallacta"*, 2018. [Online]. Available: https://goo.gl/Be3Fg1

[34] L. Pachacama Oña and M. F. Cevallos López, *Análisis de riesgo, vulnerabilidad de los estudios de la segunda etapa del proyecto de agua potable Ríos Orientales Ramal Quijos-Papallacta-Paluguillo.* Tesis de Grado. Escuela Politécnica del Ejército, 2012. [Online]. Available: https://goo.gl/rjrmWD

[35] IGM, *Cartografía de Quito 1:25000.* Instituto Geográfico Militar. Ecuador, 1990.

[36] Gestión de Comunicación. (2017) Sistema de riego cayambe-pedro moncayo. Prefectura de Pichincha. Ecuador. [Online]. Available: https://goo.gl/ReqZjP

[37] SENAGUA, *Resolución de la Agencia de Aguas de Quito, proceso 220-96.* Quito. Ecuador., 1999.

[38] SE, *Resolución de la Agencia de Aguas de Quito, proceso 1375.* Quito. Ecuador., 2005.

[39] T. Ochoa Rubio, *Centrales hidroeléctricas tomo 1.* Ediciones Grancolombianas. Universidad la Gran Colombia., 2002.

Scientific Paper / Artículo Científico

UNIVERSIDAD POLITÉCNICA SALESIANA ECUADOR
INGENIUS
Revista de Ciencia y Tecnología
https://doi.org/10.17163/ings.n21.2019.06
pISSN: 1390-650X / eISSN: 1390-860X

EMPIRICAL ESTIMATION OF THE PRESTRESSED OF A V-BELT THROUGH THE SLIP OF THE PULLEYS

ESTIMACIÓN EMPÍRICA DEL PRETENSADO DE UNA BANDA TRAPEZOIDAL MEDIANTE EL DESLIZAMIENTO DE LAS POLEAS

Eduardo Hernández-Dávila[1,*], Luis Cacuango-Eugenio[2], Verónica López-Pérez[2],
Julio Cajamarca-Villa[1]

Abstract

Inspecting the pre-tension of belts is an essential preventive maintenance activity, which requires that the machine is powered off to be carried out. This generates an economic impact of lesser or greater degree depending on the operational context of each machine. The objective of this experimental investigation is to determine a mathematical model, for calculating the pre-tension of v-belts of classic profile and high performance as a function of the slip. To achieve this objective, a test module was built to establish the difference between the theoretical and real rotation frequencies of the driven pulley, as the pre-tension of the belt was increased. Then, an inverse exponential function was adjusted to the data obtained, resulting in two equations for v-belts of classic profile and of high throughput, respectively; these equations were validated using Pearson's r correlation coefficient. The proposed mathematical model can be used to minimize the economic impact of checking the pre-tension of the belts, since it allows carrying out this activity with the machine operating on full load, requiring only the measurement of the rotation frequencies of the pulleys.

Palabras clave: v-belt, slip, pulley, prestressed of the belt.

Resumen

La inspección de la pretensión de las bandas es una actividad de mantenimiento preventivo imprescindible; que, para poder ser realizada, requiere que la máquina esté apagada, generando un impacto económico en menor o mayor grado dependiendo del contexto operacional de cada máquina. El objetivo de esta investigación experimental es determinar un modelo matemático para el cálculo del pretensado de las bandas trapezoidales de perfil clásico y de alto rendimiento en función del deslizamiento; para lo cual se construyó un módulo de prueba, en el que se estableció la diferencia de las frecuencias de rotación entre la teórica y la real de la polea conducida, a medida que se incrementó el pretensado de la banda. Los datos arrojados se ajustaron a una función exponencial inversa, dando como resultado dos ecuaciones, una para las correas trapezoidales de perfil clásico y otra para las de alto rendimiento. La validación de estas ecuaciones se realizó mediante el coeficiente de correlación r de Pearson. Con la utilización del modelo matemático propuesto, se podrá minimizar el impacto económico de las actividades preventivas de revisión del pretensado de las bandas; puesto que, estas ecuaciones posibilitan la realización de esta actividad con la máquina encendida y a plena carga, requiriendo para ello únicamente la medición de las frecuencias de rotación de las poleas.

Keywords: banda trapezoidal, deslizamiento, polea, pretensión de bandas.

[1,*] Research Group of Maintenance Science (CIMANT), Escuela Superior Politécnica de Chimborazo, Ecuador. Corresponding author ✉: edhernandez@espoch.edu.ec
http://orcid.org/0000-0003-4899-2371, http://orcid.org/0000-0002-6568-6037.

[2] Faculty of mechanics. Escuela Superior Politécnica de Chimborazo, Ecuador
http://orcid.org/0000-0003-2075-3694, http://orcid.org/0000-0002-3488-7039.

Received: 21-11-2018, accepted after review: 17-12-2018

Suggested citation: Hernández-Dávila, E.; Cacuango-Eugenio, L.; López-Pérez, V. and Cajamarca-Villa, J. (2019). «Empirical Estimation of the Prestressed of a V-Belt Through the Slip of the Pulleys». INGENIUS. N.°21, (january-june). pp. 63-70. DOI: https://doi.org/10.17163/ings.n21.2019.06.

1. Introduction

Nowadays v-belts are extensively used to transmit power in industrial machines and vehicular applications, which do not require a precise velocity and where moderate power levels are sufficient. The cost of these belts is smaller compared to transmission by chains or gears, and its operation is relatively noiseless [1, 2]. In addition, they have the characteristic of absorbing shock loads and reducing the effects of vibration [3].

In the texts about the design of machine elements, the selection of v-belts considers that the power to be transmitted should be smaller than the power that the belt, or set of belts, are capable of sustaining. This process also includes determining the initial tension or prestressed to guarantee power transmission without slipping [4–6].

However, depending on the operating conditions, in these transmission systems a slip between the belt and the pulley always exist, thus the transmission ratio is not constant [7, 8].

The slip mechanism of flat and v-belts has been extensively studied, both analytically and experimentally. Reynolds [9] demonstrated that the velocity loss is due to the elastic slip of the belt.

Gerbert [10–12] developed two theories mainly related to bending and deflection due to shearing (classical creep theory); however, the slip is much greater than what is forecasted by this theory. Afterwards, he developed a new unified theory that fitted better the experimental observations, but fails at low tension.

Belofsky [13] proposed a model that takes into account the elasticity of the belt, the resistance to bending and the variation of the friction force along the contact arch, based on a linear slip regime. This work describes an experimental method for determining μ at any point of the contact arch of the belt.

Childs and Cowburn [14] analyzed the belt bending resistance, the radial adjustment, the distortion due to the diameter of the pulley and the prestressed of the belt, to describe the velocity and torsion loss in v-belts transmission.

Chen and Shieh [15] obtained the velocity loss in a flat belt transmission system, using a 3D finite elements model. Balta, Sonmez and Cengiz [16] analyzed a multi-ribbed belt transmission system, and determined that a smaller the pulley size results in a greater belt slip, and that below a certain level of the prestressed of the belt the slip values increase.

In the consulted bibliography it was observed that most of the studies in flexible transmission systems focus on the power loss, and for this purpose the factors that influence the slip and the effects of belt prestressed are analyzed.

The values of the variables in the proposed formulations can be obtained experimentally. However, according to the authors, such values should be determined for every combination of velocity, diameters, distance between centers and pulley materials [17, 18], thus creating multiple possibilities in which it will be very difficult to include particular transmission systems that have been already built, and that take part in an industrial environment where experimental tests cannot be carried out.

Once the belts have been assembled in the transmission system and start operating, they undergo a considerable lengthening in a short period of time, thus causing the reduction of the initial tension; due to this, belt manufacturers recommend doing a prestressed in a period of time not longer than 24 hours. In subsequent days, this lengthening will appear after a much longer undefined period of time [19]. Therefore, it is required to plan a preventive activity at fixed intervals between three and six months, to verify and, is necessary, correct the prestressed [20].

There are methods with and without contact to measure the prestressed belt, which requires the machine is turned off. This requirement does not assume any problem when the machine has an operation regime of five days a week, because any preventive activity is reserved to be carried out in resting days, where the production is not interrupted, but the overtime should indeed be assumed.

In the case of machines with an operating regime of 24 hours a day, 7 days a week, the preventive maintenance activities will cause a system operational downtime and, therefore, a cost associated with non-production [21]; thus, the intervention time must be the minimum possible.

The objective of this work is finding a mathematical model based on experimentation, which may estimate the prestressed belt from direct measurement, with laser tachometers, of the velocities of the driving and driven pulleys, without requiring to turn off the machine nor requiring parameters which are difficult to obtain. Therefore, this will facilitate the work of maintenance technicians.

The main contribution is minimizing the economic impact of the inspection of prestressed belts, because with the aid of the proposed mathematical model, this activity can be conducted without interrupting the normal operation of the machine.

For carrying out this study, a test module was utilized in which the prestressed of the belt can be progressively modified while registering the variation of the produced slip. Then, a mathematical function can be fitted to describe the existing relationship between slip and prestressed.

2. Materials and methods

2.1. Experimental configuration

The configuration is shown in Figure 1 and outlined in Figure 2 it was constructed to investigate the effects of the belt tension on the velocity loss of the driven pulley, in flexible transmission systems with v-belts of classic and high performance profile. The components of the system are firmly supported on an AISI 1020 steel base, with a thickness of 10 mm. In this system, the driving pulley with diameter of 125 mm, rotates due to the mechanical energy supplied by a 373 W asynchronous squirrel cage electric motor, with four magnetic poles; thus, the frequency of rotation of the magnetic field is 30 Hz.

Figure 1. Configuration of the test module.

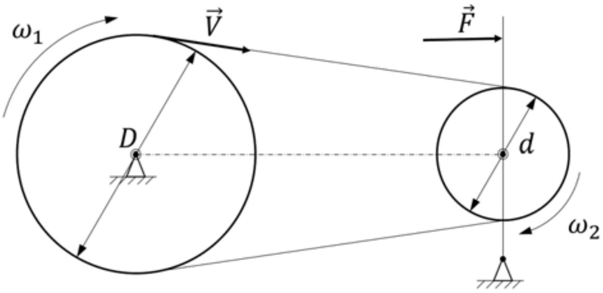

Figure 2. Outline of the belt transmission system.

The driven pulley with a diameter of 70 mm, rotates mounted on an alternator of 12 V, 35 A and a frequency of rotation of 50 Hz. A resistive load is connected to the alternator such that the electric motor supplies 80% of its nominal power.

Considering that the efficiency of the motor is 78.2%, the resistance connected to the alternator was set to the value in which the electric power supplied in the motor was:

$$P = \frac{373W \times 0,80}{0,782} \approx 382W \tag{1}$$

In order to generate tension in the belt, the alternator was attached to the base plate my means of a bolt which lets it turn around its axis, while a hardener was placed in the upper part. A digital weighing scale was inserted to work as a load cell, i.e. to measure the tension in the belt as the hardener is tighten.

This hardener is kept at a constant height, and is attached to the base plate by means of two parallel tension bars of 5 mm thickness. As can be seen in Figure 3, these bars reach a maximum static deformation of 0.9418 mm when subjected to a force of 500 N, the maximum value that can be measured with the scale. This deformation is not considered a value that can influence on the measurements during the tests, thus guaranteeing that it works correctly.

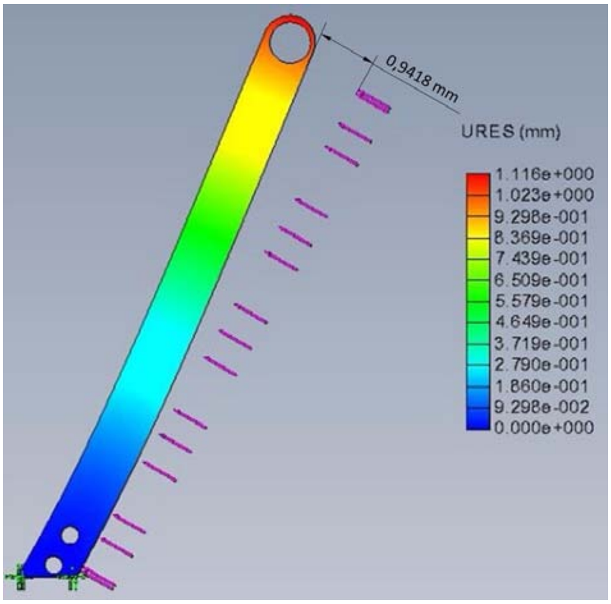

Figure 3. Maximum deformation of the parallel tension bars, obtained using the finite element method in the software Solidworks, version 2016.

Two photo tachometers are used to measure the rotation frequency of the pulleys. Such photo tachometers directly point to 10 mm x 20 pieces of reflective tape stuck away from the center on the outer side of the pulleys.

The tested v-belts included the classic profile A-23 and the high performance SPA-23, both with a length of 584.2 mm and manufactured by Dongil.

2.2. Calculation of slip

The slip produced in the belt transmission system is the ratio of the difference between the theoretical and real (measured) angular velocities of the driven pulley, to the theoretical angular velocity. Hence, this can be mathematically expressed as:

$$Dz = \frac{\omega_{t2} - \omega_2}{\omega_{t2}} \tag{2}$$

where Dz is the slip, ω_{t2} is the theoretical angular velocity of the driven pulley calculated using the equations that describe the uniform circular motion, and ω_2 is the real (measured) angular velocity of the pulley.

Considering that the angular velocity can be expressed in terms of the frequency as:

$$\omega = 2 \times \pi \times f \tag{3}$$

and that, for the uniform circular motion, the theoretical angular velocity of the driven pulley is given by:

$$\omega_{t2} = \omega_1 \times \frac{D}{d} \tag{4}$$

where ω_1 is the real angular velocity of the driving pulley and D and d are, respectively, the diameters of the driving (bigger) and driven (smaller) pulleys given in meters (m), equation (2) can be equivalently expressed as

$$Dz = 1 - \frac{f_2 \times d}{f_1 \times D} \tag{5}$$

where f_1 and f_2 are, respectively, the real rotation frequencies of the driving and driven pulleys, given in Hertz (Hz) or revolutions per minute (rpm).

2.3. Calculation of the belt tension

In order to calculate the belt tension from the scale measurements, a static analysis of the module tensioning system is carried out. Figure 4 illustrates the configuration of such tensioning system, while Figures 4 y 5 shows its equilibrium diagram.

Since the force measured by the scale acts on point H (Figure 4) and the alternator is centered in G, a summation moment in the latter results in:

$$\begin{aligned} &\overline{GA} \times \vec{T_2} \times sen(\beta - \varphi) + \overline{GB} \times W \times cos(\beta) + \\ &+ \overline{GC} \times \vec{t_1} \times sen(\beta + \varphi) - \overline{GH} \times \vec{F} \times sen(\beta) = 0 \end{aligned} \tag{6}$$

If the machine is at rest (off, without any rotational movement), the tensions T_1 and T_2 on the belt are equal. Substituting the values of distance (Table 1) yields:

$$T = \frac{3 \times (2F \times sen(\beta) - W \times cos(\beta))}{2 \times (2 \times sen(\beta + \varphi) + sen(\beta - \varphi))} \tag{7}$$

In this rest condition, the tension T calculated using equation (7) is known as prestressed. At this point it should be clarified that once the pulleys start rotating, tensions 1 and 2 become different [3]. This case has not been considered, since the belt prestressed in maintenance operations is carried with the machine at rest (off, i.e. with no motion).

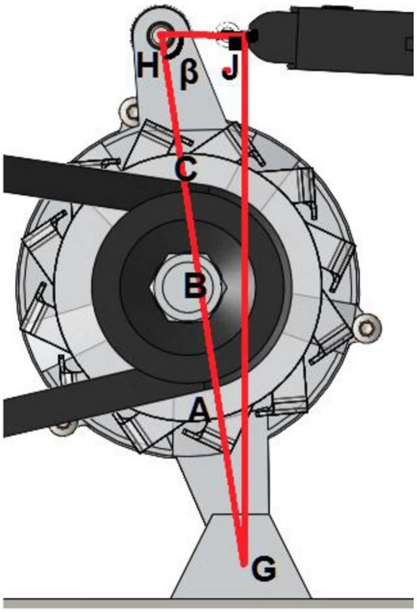

Figure 4. Tension system of the module band.

Table 1. Distances in Figure 4, given in mm

$\overline{GA}$	$\overline{GB}$	$\overline{GC}$	$\overline{GH}$
60	90	120	180

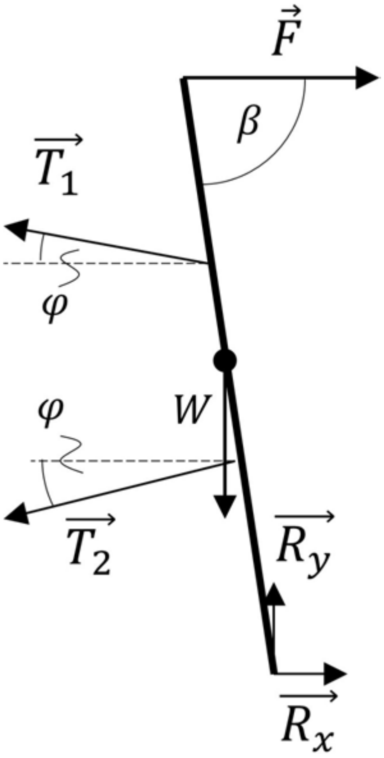

Figure 5. Equilibrium diagram of the tensioning system of the belt in the module.

3. Results and discussion

The results are shown in Tables 2 and 3 for v-belts of classic profile and high performance, respectively, were obtained using the average of five measurements of the pulleys rotation frequencies, and the applied force by the tensioning system at increasing intervals of 50 N. In such tables, the tension T and the slip Dz were calculated by means of equations (5) and (7), respectively.

Table 2. Slip and tension of the v-belt of classic profile

F (N)	*T* (N)	*f1* (Hz)	*f2* (Hz)	Dz
49,05	39,7	29,17	50,43	3,17
98,1	88,22	29,08	50,45	2,86
147,15	136,51	29	50,47	2,55
196,2	185,14	28,92	50,48	2,23
245,25	233,47	28,83	50,5	1,92
294,3	281,79	28,77	50,48	1,72
343,35	330,12	28,63	50,27	1,69
392,4	378,45	28,5	50,05	1,66
441,45	426,77	28,37	49,83	1,62
490,5	475,1	28,23	49,62	1,59

Table 3. Slip and tension of the v-belt of high performance

F (N)	*T* (N)	*f1* (Hz)	*f2* (Hz)	Dz
49,05	39,7	29,3	51,43	1,7
98,1	88,22	29,22	51,38	1,51
147,15	136,51	29,15	51,33	1,38
196,2	185,14	29,08	51,28	1,25
245,25	233,47	29,02	51,25	1,09
294,3	281,79	28,95	51,18	0,99
343,35	330,12	28,92	51,13	0,98
392,4	378,45	28,85	51,03	0,94
441,45	426,77	28,78	50,93	0,91
490,5	475,1	28,72	50,83	0,87

On the other hand, Table 4 indicates the tension of the v-belts of classic profile and of high performance, and the calculated theoretically according to design books, by means of the equation [3].

$$T = \frac{280159.39 \times Hd \times (e^{f\varphi}+1)}{n \times d \times (e^{f\varphi}-1)} \tag{8}$$

where, *Hd* is the maximum transmitted mechanical power in horsepower (hp), calculated as the product of the measured electric consumption of the motor and the efficiency (0.782 in this case) with an increase of 20% due to the service factor, n is the rotation frequency of the driven pulley in revolutions per minute (rpm), d is the diameter of the same pulley in inches, f is the friction coefficient for v-belts (which is equal to 0,5123 [3]), and φ is the contact angle given by.

$$\varphi = \pi - 2 \times sen^{-1}\frac{D-d}{2 \times C} \tag{9}$$

where D and d are given in mm, and C is the distance between the centers of both pulleys, also in mm.

Table 4. Theoretical and experimentally induced tensions in the v-belts of classic profile and of high performance

***T* teórica de the v-belt of classic profile (N)**	**Theoretical *T* the v-belt of high performance (N)**	**Theoretical *T* of induced *T* (N)**
31,1	27,11	39,7
32,82	28,83	88,22
34,52	30,55	136,51
36,23	31,42	185,14
38,8	33,13	233,47
41,39	34,87	281,79
44,16	36,6	330,12
45,21	38,37	378,45
48,02	40,15	426,77
49,1	41,93	475,1

It can be seen in Table 4 that the theoretical tensions are smaller than the experimentally induced; hence, no slip should exist. Nevertheless, Tables 2 and 3 indicate that it indeed existed, confirming the observations on [7, 8]. Therefore, this research is applicable to any design condition of this type of systems.

Figure 6 is a plot of the slip values as a function of the prestressed for both classic profile and high performance v-belts, from data in Tables 2 and 3.

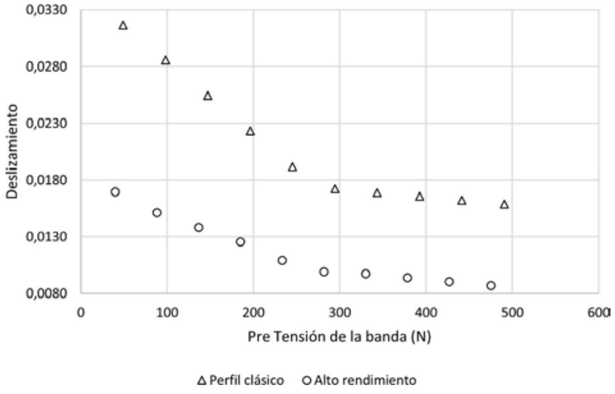

Figure 6. Slip as a function of prestressed for the v-belts.

In order to obtain the mathematical model, the following conditions were considered:

The slip is an index whose value is between zero and 1. As the prestressed increases, the slip decreases toward zero, but it can never take negative values. This means that as the prestressed T goes to infinity, the slip goes to zero, i.e.

$$\lim_{T \to \infty} Dz(T) = 0 \tag{10}$$

If there is not prestressed (it is equal to zero) there is not power transfer between the driving and driven pulleys, thus the latter will not move at all. In this case the slip takes it maximum value of one, which means that the belt totally slips on the driven pulley without transmitting any motion, i.e.

$$Dz(T=0)=1 \tag{11}$$

These conditions are satisfied by inverse exponential models. In particular, a distribution of the type:

$$Dz=e^{-(\alpha T)^{\beta}} \tag{12}$$

was chosen due to its flexibility, where α y β are, respectively, the scale and shape parameters of the model.

In order to obtain the parameters of the model using least squares, it is suggested to linearize Equation (12) through the application of logarithms, to obtain

$$ln\left(ln\left(\frac{1}{Dz}\right)\right)=\beta ln(T)+\beta ln(\alpha) \tag{13}$$

which is used to generate the plot of Figure 7. These data points fit straight lines, with Pearson correlation coefficients r of 0.9767 and 0.9809 for the classic profile and high performance v-belts.

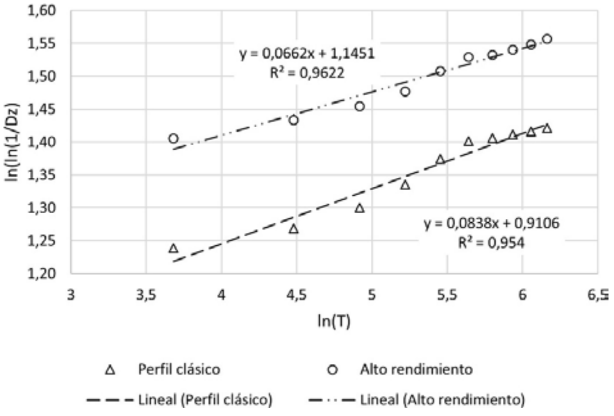

Figure 7. Linearization of the slip curve as a function of the prestressed of the belts.

Then, Table 5 shows the parameters of the linearized models (13) identified using least squares, which result in the mathematical models

Table 5. Parameters of the linearized equations of slip as a function of belt tension

Tipe of band	Slope	Intersection	α	β
Classic profile	0,0838	0,9106	$5{,}27E^{+04}$	0,0838
High performance	0,0662	1,1451	$3{,}19E^{+07}$	0,0663

$$Dz=e^{-(5{,}27E^{+04}T)^{0{,}0838}} \tag{14}$$

$$Dz=e^{-(3{,}19E^{+07}T)^{0{,}0663}} \tag{15}$$

In order to validate the fit of equations (14) and (15) to the experimental data, the following hypotheses are stated:

H_0: The slip is not an inverse exponential function of the prestressed of the belts.

H_1: The slip is an inverse exponential function of the prestressed of the belts.

It can be seen that the obtained Pearson correlation coefficients r, 0.9767 for the v-belt of classic profile and 0.9809 for the v-belt of high performance, are both greater than 0.765 for a set of ten data. Therefore, the null hypothesis is rejected, and the alternative hypothesis is accepted which states that the slip is an inverse exponential function of the prestressed of the belts, with a 99% confidence [22].

Solving equations (14) and (15) for the prestressed T, yields the mathematical models (16) and (17).

$$T=1{,}91E^{-0.5}\times\left[ln\left(\frac{1}{Dz}\right)\right]^{\frac{1}{0{,}0838}} \tag{16}$$

$$T=3{,}13E^{-0.8}\times\left[ln\left(\frac{1}{Dz}\right)\right]^{\frac{1}{0{,}0663}} \tag{17}$$

which constitute the purpose of this research.

4. Conclusions

As it is observed in Tables 2 and 3, and in Figure 6, the slip produced by the same tension is different for the classic profile and high performance v-belts; however, they exhibit the same trend. This is confirmed by the shape parameter β in Table 5, which are similar.

The slip in power transmission systems that employ belts and pulleys, fits an inverse exponential model with 99% confidence; thus, it is reliable to use equations (14) and (15) to estimate the prestressed in belts from direct measurement of the slip, without requiring to turn off the machine.

According to the observations in Figure 6, the transmission systems with high performance v-belts are more efficient than the systems with v-belts of classic profile, because they exhibit a smaller slip.

References

[1] R. L. Norton, *Diseño de maquinaria: síntesis y análisis de máquinas y mecanismos.* McGraw-Hill, México, 2013. [Online]. Available: https://goo.gl/fGK4tx

[2] A. J. Nieto Quijorna, *Elementos de máquinas.* Área de Ingeniería Mecánica, Universidad de Castilla-La Mancha, España, 2007. [Online]. Available: https://goo.gl/4wkZpd

[3] Budynas, R. G, N. J. Keith, and J. E. Shigley, *Mechanical Engineering Design.* McGraw-Hill Education, New York, USA, 2015. [Online]. Available: https://goo.gl/1TivVq

[4] R. L. Mott, *Diseño de elementos de máquinas.* Pearson Education,, 2006. [Online]. Available: https://goo.gl/buKXz3

[5] R. C. Juvinall, *Diseño de elementos de máquinas.* Limusa Wiley, 2013. [Online]. Available: https://goo.gl/xtrD3K

[6] V. B. Bhandari, *Design of Machine Elements.* McGraw-Hill Education, India, 2016.

[7] A. D. Almeida and S. Greenberg, "Technology assessment: energy-efficient belt transmissions," *Energy and Buildings*, vol. 22, no. 3, pp. 245–253, 1995. [Online]. Available: https://doi.org/10.1016/0378-7788(95)00926-O

[8] C. A. Silva, M.-A. Andrianoely, L. Manin, S. Ayasamy, C. Santini, E. Besnier, and D. Remond, "Optimization of power losses in poly-v belt transmissions via genetic algorithm and dynamic programming," *Mechanism and Machine Theory*, vol. 128, pp. 169–190, 2018. [Online]. Available: https://doi.org/10.1016/j.mechmachtheory.2018.05.016

[9] O. Reynolds, "On the efficiency of belts or straps as communicators of work," *Journal of the Franklin Institute*, vol. 99, no. 2, pp. 142–145, 1875. [Online]. Available: https://doi.org/10.1016/0016-0032(75)90662-6

[10] G. Gerbert, "A note on slip in v-belt drives," *Journal of Engineering for Industry*, vol. 98, no. 4, pp. 1366–1368, 1976. [Online]. Available: https://doi.org/10.1115/1.3439115

[11] ——, "Paper xii (i) on flat belt slip," in *Vehicle Tribology*, ser. Tribology Series, D. Dowson, C. Taylor, and M. Godet, Eds. Elsevier, 1991, vol. 18, pp. 333–340. [Online]. Available: https://doi.org/10.1016/S0167-8922(08)70149-4

[12] ——, "Belt slip-a unified approach," *Journal of Mechanical Design*, vol. 118, no. 3, pp. 432–438, 1996. [Online]. Available: https://doi.org/10.1115/1.2826904

[13] H. Belofsky, "On the theory of power transmission by v-belts," *Wear*, vol. 39, no. 2, pp. 263–275, 1976. [Online]. Available: https://doi.org/10.1016/0043-1648(76)90054-5

[14] T. H. C. Childs and D. Cowburn, "Power transmission losses in v-belt drives part 2: Effects of small pulley radii," *Proceedings of the Institution of Mechanical Engineers, Part D: Transport Engineering*, vol. 201, no. 1, pp. 41–53, 1987. [Online]. Available: https://doi.org/10.1243/PIME_PROC_1987_201_156_02

[15] W.-H. Chen and C.-J. Shieh, "On angular speed loss analysis of flat belt transmission system by finite element method," *International Journal of Computational Engineering Science*, vol. 04, no. 01, pp. 1–18, 2003. [Online]. Available: https://doi.org/10.1142/S1465876303000752

[16] B. Balta, F. O. Sonmez, and A. Cengiz, "Speed losses in v-ribbed belt drives," *Mechanism and Machine Theory*, vol. 86, pp. 1–14, 2015. [Online]. Available: https://doi.org/10.1016/j.mechmachtheory.2014.11.016

[17] G. Čepon, L. Manin, and M. Boltežar, "Experimental identification of the contact parameters between a v-ribbed belt and a pulley," *Mechanism and Machine Theory*, vol. 45, no. 10, pp. 1424–1433, 2010. [Online]. Available: https://doi.org/10.1016/j.mechmachtheory.2010.05.006

[18] L. Bertini, L. Carmignani, and F. Frendo, "Analytical model for the power losses in rubber v-belt continuously variable transmission (cvt)," *Mechanism and Machine Theory*, vol. 78, pp. 289–306, 2014. [Online]. Available: https://doi.org/10.1016/j.mechmachtheory.2014.03.016

[19] Optibelt, "Manual técnico para transmisiones por correas trapeciales," Optibelt Power Transmission, Tech. Rep., 2008.

[20] Gates, "Mantenimiento preventivo de correas y transmisiones," Gates Corporation, Tech. Rep., 2009.

[21] E. Hernández, B. Angulo, P. Fiallos, and V. Chávez, "Método para el cálculo del costo de la indisponibilidad en procesos productivos," *Perfiles,*, vol. 1, pp. 90–98, 2017.

[22] M. F. Triola, *Estadística.* Pearson Education, 2013. [Online]. Available: https://goo.gl/Zfkisc

Scientific Paper / Artículo Científico

UNIVERSIDAD POLITÉCNICA SALESIANA ECUADOR
INGENIUS
Revista de Ciencia y Tecnología
https://doi.org/10.17163/ings.n21.2019.07
pISSN: 1390-650X / eISSN: 1390-860X

ANALYSIS AND COMPARATION OF ISDB-T USING MODULATIONS OFDM AND CC-OFDCM

ANÁLISIS Y COMPARACIÓN DE ISDB-T UTILIZANDO MODULACIONES OFDM Y CC-OFDCM

José Gómez[1], Holger Lapo[1], Luis Oñate[1,*]

Abstract

Digital Terrestrial Television (DTT) is focused on replacing analog television transmissions, using OFDM (orthogonal frequency division multiplexing) modulation, which enables transmitting to both fixed and mobile equipment. Nevertheless, in the case of mobile digital television receivers, such as smartphones, laptops and other devices there are reception problems due to the multipath effect. In this project, the OFDM and CC-OFDM (Orthogonal Frequency Division Multiplexing by Convolution Coding) modulation schemes are simulated for the ISDB-T (Integrated Services Digital Television Broadcasting) standard. By means of the Simulink graphical programming environment, from Matlab, the block diagrams of both schemes were implemented and the data transmission was simulated, further measuring the BER (Bit Error Rate), the delay and the number of carriers, for three types of channels, namely: AWGN (Additive White Gaussian Noise), Type A land (rural land) and Type C land (urban land). The results obtained indicate that CC-OFDM modulation has a higher efficiency, due to higher BER and reduction in the reception delay.

Keywords: CC-OFDM, ISDB-T, Multiway, OFDM, Simulink.

Resumen

La Televisión Digital Terrestre está orientada a sustituir las transmisiones de televisión analógica, al utilizar la modulación OFDM (multiplexación por división de frecuencias ortogonales), con esta modulación se puede realizar transmisiones para equipos fijos y móviles. Sin embargo, en el caso de sistemas de recepción de televisión digital como teléfonos inteligentes, portátiles y otros dispositivos móviles tienen problemas en la recepción causados por el efecto multicamino. En este proyecto se realiza la simulación de las modulaciones OFDM y CC-OFDM (Multiplexación por División de Frecuencias Ortogonales mediante Codificación por Convolución) para el estándar de televisión ISDB-T (Radiodifusión Digital de Servicios Integrado para Televisión). Por medio de Simulink del entorno Matlab, se simuló los diagramas de bloques de ambas arquitecturas para observar los resultados al transmitir datos, midiendo el BER (Tasa de Bit Errado), el retardo y el número de portadoras, bajo los siguientes canales: AWGN (Ruido Gaussiano Blanco Aditivo), Terreno tipo A (terreno rural) y Terreno tipo C (terreno urbano). De los resultados obtenidos se muestra que la modulación CC-OFDM tiene una mayor eficiencia, debido a que presenta un BER mayor y reducción en el retardo en la recepción.

Palabras clave: CC-OFDM, ISDB-T, Multicamino, OFDM, Simulink

[1,*] Electronic Engineering, Universidad Politécnica Salesiana, Ecuador. Corresponding author ✉: lonate@ups.edu.ec. http://orcid.org/0000-0003-0741-2115, http://orcid.org/0000-0002-4885-4414, http://orcid.org/0000-0002-1323-1858

Received: 22-10-2018, accepted after review: 12-12-2018

Suggested citation: Gómez, J.; Lapo, H. y Oñate, L. (2019). «Analysis and comparation of ISDB-T using modulations OFDM and CC-OFDCM». INGENIUS. N.°21, (january-june). pp. 71-77. DOI: https://doi.org/10.17163/ings.n21.2019.07.

1. Introduction

The digital television is geared towards substituting analog television, because it has the advantage of including interactive applications, such as surveys, programming times and emergency signals, among others, as well as different types of signal quality in high definition (HD) and standard definition (SD) [1].

When digital television signals are received in mobile devices, such as smartphones and laptops, among others, there are impulsive noise issues due to multipath in the ISDB-T standard, when the usual OFDM modulation is employed [2].

The ISDB-T (Integrated Services Digital Broadcasting-Terrestrial) standard had its origin in Japan, being developed in the late 1990s. The main objective of this standard was to enable the simultaneous transmission of HDTV (High Definition Television) and SDTV (Standard Definition Television). ISDB-T was designed to operate in channels of bandwidth 6.7 and 8 MHz, respectively. In Ecuador this standard should operate in a channel of 6 MHz [3].

In the last decade, the orthogonal frequency division multiplexing (OFDM) has become the basis of telecommunication systems, and it is a technique utilized in wireless transmission [4] and fiber optic systems [5]. The advantages of OFDM are the management of multipath interference, mitigation of intersymbol interference (ISI) caused by the bit error rate (BER) in frequency selective fading [6]. On the other hand, the orthogonal frequency division multiple access (OFDMA) is a multicarrier transmission technique, which is considered as one of the best for bidirectional wireless networks is communication systems and for broadcasting digital television, especially in the ISDB-T television system being used in Ecuador; besides, it is used in satellite and space communications, reducing the errors. The BER, defined as the number of bit errors divided by the total number of transferred bits during a time interval, is the quality criterion utilized in digital transmission and data storage.

The broadcasts of digital terrestrial television tend to be reflected on buildings and mountains; as a consequence, the multipath phenomenon appears in the propagation. In order to avoid the interference, the digital television ISDB-T utilized in Ecuador is based on the Japanese system with the Brazilian patch, and employs OFDM as modulation scheme. This technique is not robust, and shows long delays in multipath transmissions which may exceed the guard interval (GI) or produce high peaks in the transmission power [7], particularly in the time-domain because many subcarrier components are added when the inverse fast Fourier transform (IFFT) is used [8]. But beyond that, OFDM systems have a high peak-to-average power ratio (PAPR) with respect to systems with one carrier. When signals with a high PAPR pass through a nonlinear element, such as a high power amplifier (HPA) [9], it is produced a signal out of the range of the spectrum of the carriers that will interfere with adjacent channels and in the carrier spectrum, thus causing distortion, attenuation and an offset in the received signal. A HPA with a big dynamic range will produce high losses in the communication system. This can be reduced using systems with low losses, but the cost will increase. The fading effect can be compensated using CC-OFDM [10].

The convolution coding based orthogonal frequency division multiplexing (CC-OFDM) modulation in orthogonal frequency division multiplexing (OFDM) systems, has become a very used tool in the current technology. Similarly, in other communication systems the OFDM system needs to use channel codification to decrease the VER, such as CC-OFDM [11]. Figure 1 shows the block diagram of the CC-OFDM modulation [12].

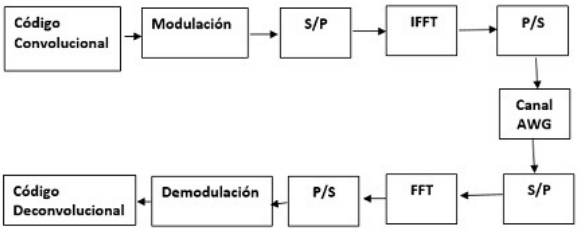

Figure 1. OFDM with convolution code.

In this paper, the CC-OFDM modulation is analyzed and simulated in ISDB-T architectures, to determine how the efficiency is improved in environments with multipath, as well as to observe the behavior of parameters such as BER, delay and number of carriers.

The block diagram in Figure 1 is constituted by: generator of the convolution code, which is a type of error correction code; modulation, which in this case is 64 QAM, even though other types of modulation such as QPSK, QAM, 16 QAM, 32 QAM can be used; a serial to parallel (P/S) converter; inverse fast Fourier transform (IFFT); AWG channel, which is the data transmission medium where attenuation, noise and signal fading will be introduced; parallel to serial (S/P) converter; fast Fourier transform (FFT); a second P/S converter, demodulation and, at last, the convolutional code decoding [13].

2. Materials and methods

Configurable parameters and values of the ISDB-T standard must be taken into account in the corresponding model, since they will completely define the operating mode of the system blocks as described in [14]. Figure 2 shows the block diagram of transmission and reception for the ISDB-T standard with OFDM modulation, created in Matlab Simulink. This block diagram is now described.

The image generator employs a Signal From Workspace block, which is in charge of importing the image data from the Matlab Workspace [15].

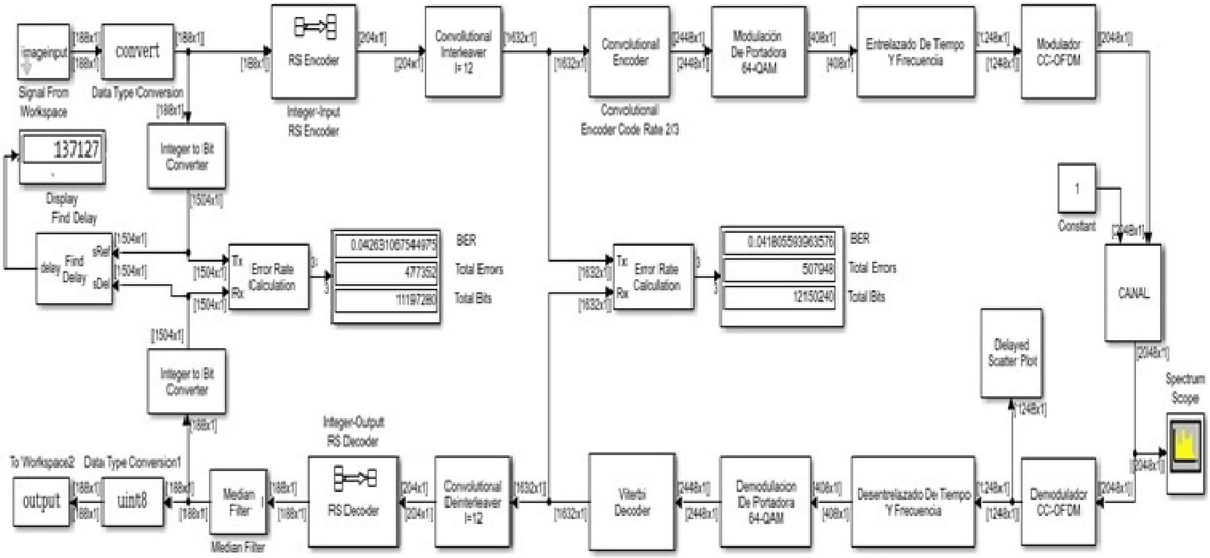

Figure 2. Block diagram of the ISDB-T standard with OFDM modulation, created in Matlab Simulink.

The Reed Salomon encoder carries out a block-based error correction process, for block processing a certain amount of data symbols. A code of the form k/n = 188/204 is employed in this case [16].

The integer to bit converter uses a value of 8, to obtain a total value of 1632 bits, as required by the norm [17]. The carrier modulation employs a block known as matrix interleaver, which will do the process of bits interleaving. Then, a mapping process is carried out; this process comprises two blocks, namely a bit to integer converter and a rectangular QAM modulator. In order to obtain a 64-QAM modulation, it is necessary to enter a value of 6 in the bit to integer converter, and also a value of 64 in the QAM modulator [18].

The time and frequency interleaving comprises a buffer, in which the number of rows and columns indicated by the standard (96 × 204) are entered, to further carry out the serial to parallel conversion. The matrix interleaver block contains the aforementioned rows and columns in order to correctly transmit the data. At last, a second buffer stores the 1248 data that belong to the standard [19].

In the OFDM modulation, the total number of carrier (2048) is assigned, and then the parameter number of guard bands [400;400] is entered which will enable obtaining the 1248 used by the simulator. Figure 3 shows the block diagram of transmission and reception for CC-OFDM [20].

In addition, a 3 taps line was implemented in the AWGN channel, known as Stanford University Interim (SUI) channels, to incorporate the effect of multipath; besides an AGWN block was added to introduce additive white Gaussian noise. The selected radio frequency communication model can be used in Wimax, digital television, and long distance wireless communication [21]. The OFDM demodulator performs the inverse process of the OFDM modulation. In the time and frequency deinterleaving an inverse process is conducted, in which the obtained output vector of [272×1] should be equal to the indicated in the transmission process, in order to proceed with the following stage [22].

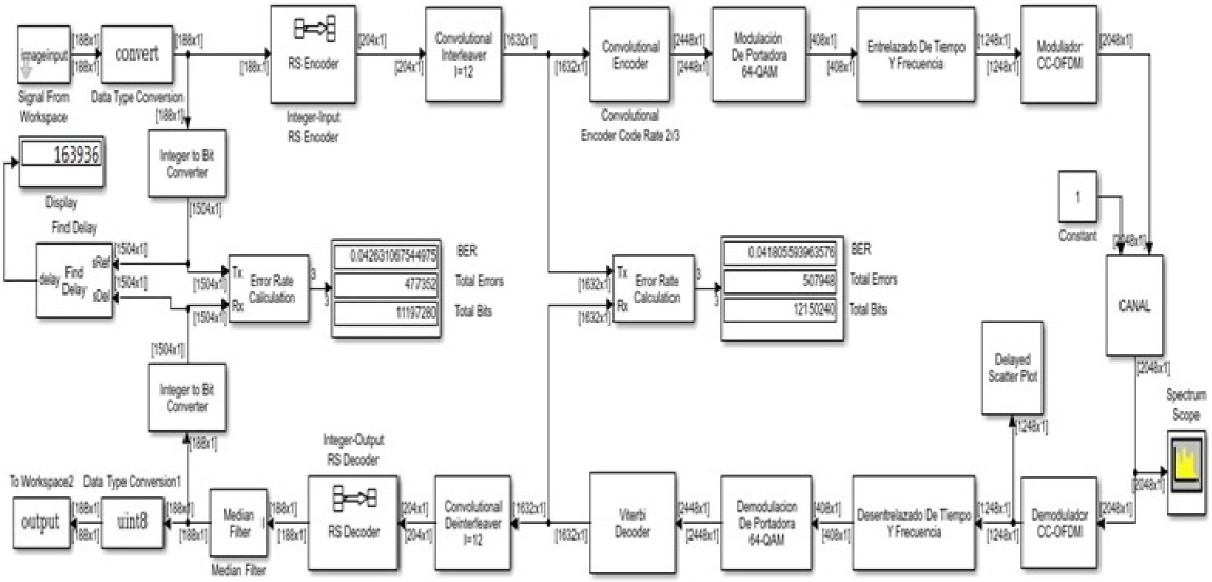

Figure 3. Block diagram of the ISDB-T standard with CC-OFDM modulation, created in Matlab Simulink.

In this subsystem, the carrier demodulation performs the bits deinterleaving, to further demodulate the 64-QAM with the rectangular demodulation block. The bit to integer converter converts the 1632 bits entered in the matrix deinterleaver, to 204 integers required in the following block [23]. In the values of the parameters in the Reed Solomon decoder match the values entered in Reed Salomon encoder, the recovered binary message vector will be equal to the message sent [24]. The median filter block was used to diminish the salt and pepper effect present in the received images, which was introduced in the communication channel; this filter calculates the mean of the pixels of the processed image, and uses a kernel to approximate the closer pixels thus reducing the noise [25]. In order to present the transmitted image, a To Workspace block is used in the ISDB-T standard with modulation CC-OFDM.

The Simulink blocks with CC-OFDM modulation use bits interleaving and de-interleaving for error correction. In addition, a convolutional encoder and its inverse, a Viterbi decoder, are added to obtain a smaller BER [26]. The Convolutional Interleaver block carries out a convolutional interleaving of bytes, to improve the performance against errors. The convolutional encoder was applied to a punctured vector, choosing a coding rate of 2/3 with an extension of 7 bits of convolution [?]. The Viterbi Decoder block decodes the signal coded by the convolutional encoder, using the Viterbi algorithm. This decoder uses the Trellis features of the convolutional code, and the Viterbi algorithm reduces the difficulty in the calculation to avoid taking into account all possible sequences [27]. The convolutional deinterleaver rearranges the symbols of the signal, which was interleaved using shift registers with fixed delay.

3. Results and discussion

Table 1 shows the bit error rate (BER) for different TDT standards and the corresponding modulations with a SNR of 19 [dB], since this value will enable to obtain a clear image with low noise.

Table 1. Bit Error Rate results

Standard	**ISDB-T (BER)**	
SNR[dB]	**OFDM**	**CC-OFM**
19	0,04333	0,04263

Calculations were conducted with a SNR = 16 [dB] [22], since this value will yield the best efficiency in the presence of multipath, both in sites A and C.

Table 2 shows the delays, given in seconds, for each of the modulations schemes of the TDT standards under consideration.

Table 2. Delay results

Standard	**ISDB-T (BER)**	
Modulations	**OFDM**	**CC-OFM**
Delay	6,9963 [ms]	8,3640 [ms]

Table 3 shows the results corresponding to BER *vs.* SNR, having as input a RGB image. The results are different because of the variation in the SNR, which is produced in the 2 channels SUI implemented in the simulation, in order to determine which of the standards exhibits the best performance in the presence of multipath. It can be seen that the BER is smaller for the CC-OFDM modulation.

Table 3. BER *vs.* SNR [dB] results with multipath

ISDB-T				
	OFDM VER		**CC-OFM VER**	
SNR Db	**Terrain A**	**Terrain C**	**Terrain A**	**Terrain C**
10	0,13040	0,11866	0,32612	0,24866
12	0,10997	0,09436	0,20365	0,09556
14	0,09357	0,07342	0,10164	0,04618
16	0,08112	0,05699	0,05799	0,04277
48	0,07194	0,04702	0,04650	0,04263
20	0,06546	0,04291	0,04439	0,04263

Figure 4 shows the results corresponding to the ISDB-T standard, where it is observed that the plots corresponding to sites A (urban) and C (rural) with CC-OFDM modulation, of color gray and yellow, respectively, show a better BER for SNR 16 dB, tan their OFDM counterparts. In the presence of multipath, the images transmitted using CC-OFDM modulation exhibit lower salt and pepper noise.

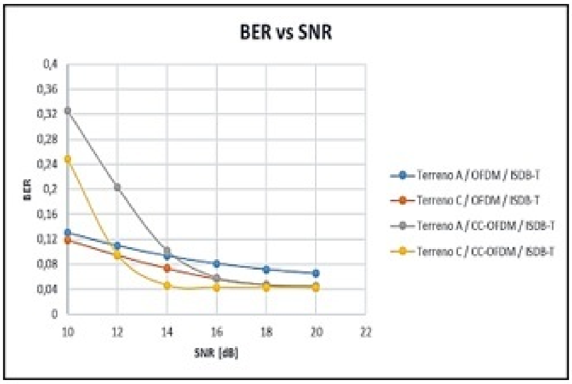

Figure 4. BER *vs.* SNR for a RGB input image applying the effect of multipath for the ISDB-T standard.

Table 4 confirms that CC-OFDM is more efficient in both sites.

Table 4. Approximate values of efficiency for the ISDB-T standard, with a SNR = 16 [dB]

ISDB-T				
	OFDM VER		**CC-OFM VER**	
SNR Db	**Terrain A**	**Terrain C**	**Terrain A**	**Terrain C**
16	91,887	94,300	94,201	95,273

At last, the results obtained for an image with SNR=16 [dB] for a site of type C (urban) are shown. Figure 5 is the original transmitted image, Figure 6 is the image received using OFDM, and Figure 7 is the image received with CC-OFDM.

Table 3 shows the results corresponding to BER vs. SNR, having as input a RGB image. The results are different because of the variation in the SNR, which is produced in the 2 channels SUI implemented in the simulation, in order to determine which of the standards exhibits the best performance in the presence of multipath. It can be seen that the BER is smaller for the CC-OFDM modulation.

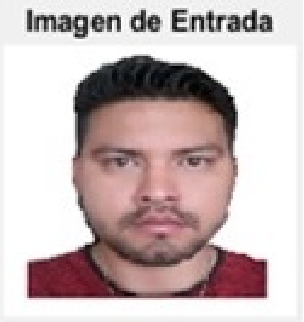

Figure 5. Original input image.

Figure 6. Output image after passing through site C with SNR=16 [dB] and OFDM modulation.

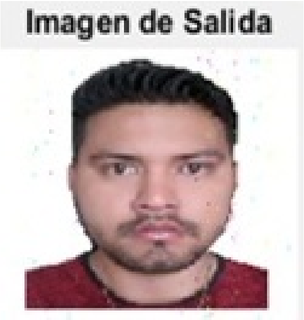

Figure 7. Output image after passing through site C with SNR=16 [dB] and CC-OFDM modulation.

4. Conclusions

An OFDM system has many carriers for the ISDB-T standard, because the bandwidth allocated for each carrier is narrow. This reduces the symbol velocity in a proportional manner, thus increasing the time to transmit each symbol. As a consequence, this system is more susceptible to interferences due to multipath.

It is concluded that a CC-OFDM modulation is more 24.95% more efficient than OFDM for the ISDB-T standard, according to the BER obtained in the simulation of an urban site with a delay of 8.3640 [ms]. It is also more reliable, but with a delay 16.35% greater as compared to the OFDM modulation.

References

[1] M. Fuentes Muela, *Evaluación de prestaciones (rendimiento e interferencias) del estándar de Televisión Digital Terrestre ISDB-Tb, mediante simulaciones y mediciones.* Proyexcto final de Carrera, Universidad Politécnica de Valencia, España, 2012. [Online]. Available: https://goo.gl/LQyMFm

[2] N. O. Pisciotta, "Remultiplexor isdb-tb," *Memoria Investigaciones en Ingeniería*, no. 12, pp. 57–69, 2014. [Online]. Available: https://goo.gl/5UdD74

[3] ——, "Sistema isdb-tb. (primera ppart)," *UBP Serie Materiales de Investigación*, no. 9, pp. 1–45, 2010. [Online]. Available: https://goo.gl/Tktnh9

[4] S. Hara and R. Prasad, *Multicarrier Techniques for 4G Mobile Communications.* Norwood, MA, USA: Artech House, Inc., 2003. [Online]. Available: https://goo.gl/iLGLJj

[5] J. Armstrong, "OFDM for optical communications," *Journal of Lightwave Technology*, vol. 27, no. 3, pp. 189–204, Feb 2009. [Online]. Available: https://doi.org/10.1109/JLT.2008.2010061

[6] M. Engels, *Wireless OFDM Systems: How to Make Them Work?* Norwell, MA, USA: Kluwer Academic Publishers, 2002.

[7] V. Sharma, A. Shrivastav, A. Jain, and A. Panday, "Ber performance of ofdm-bpsk,-qpsk,- qam over awgn channel using forward error correcting code," *International Journal of Engineering Research and Applications (IJERA)*, vol. 2, no. 3, pp. 1619–1624, 2012. [Online]. Available: https://goo.gl/2Fs5AU

[8] M. Taguchi, K. Murayama, T. Shitomi, S. Asakura, and K. Shibuya, "Large-capacity wireless transmission technology," *ITE Transactions on Media Technology and Applications (MTA)*, vol. 1, no. 1, pp. 34–39, 2013. [Online]. Available: https://goo.gl/XJnDxo

[9] A. Joshi and D. S. Saini, "Performance analysis of coded ofdm for various modulation schemes in 802.11a based digital broadcast applications," in *Information Processing and Management*, V. V. Das, R. Vijayakumar, N. C. Debnath, J. Stephen, N. Meghanathan, S. Sankaranarayanan, P. M. Thankachan, F. L. Gaol, and N. Thankachan, Eds. Berlin, Heidelberg: Springer Berlin Heidelberg, 2010, pp. 60–64. [Online]. Available: https://doi.org/10.1007/978-3-642-12214-9_11

[10] K. Thenmozhi and V. Prithiviraj, "Suitability of coded orthogonal frequency division multiplexing (cofdm) for multimedia data transmission in wireless telemedicine applications," in *International Conference on Computational Intelligence and Multimedia Applications (ICCIMA 2007)*, vol. 4, Dec 2007, pp. 288–292. [Online]. Available: https://doi.org/10.1109/ICCIMA.2007.166

[11] M. D. Hassib, J. Mandeep, M. Abdullah, M. Ismail, R. Nordin, and M. Islam, "Improved concatenated (rs-cc) for ofdm systems," *IEICE Electronics Express*, vol. 9, no. 6, pp. 538–543, 2012. [Online]. Available: https://doi.org/10.1587/elex.9.538

[12] F. Tarrés and C. M., *Codificación de canal II: códigos convolucionales.* Universidad Oberta de Catalunya, 2012. [Online]. Available: https://goo.gl/J2WMP9

[13] S. S. Joshi and A. P. Laturkar, "Ber improvement in ofdm using coding techniques," *International Journal of Electrical and Electronics Research*, vol. 2, no. 3, pp. 167–173, 2014. [Online]. Available: https://goo.gl/Q22qJ2

[14] L. R. Cantos Sanchez, S. J. Tapuy Rendon, and B. Ramos Sanchez, *Simulación Del Estándar de Televisión Digital ISDB-Tb Basado En Un Esquema De Modulación/ Demodulación OFDM Implementado en Matlab-Simulink.* Tesis de grado, Escuela SUperior Politécnica del Litoral, Ecuador, 2014. [Online]. Available: https://goo.gl/mA12pc

[15] P. S. Calderón Valarezo, *Análisis del Desempeño de la Técnica OFDM Sobre Canales Dispersos.* Tesis de grado, Universidad de las Fuerzas Armadas, Ecuador, 2007. [Online]. Available: https://goo.gl/vVu1PC

[16] J. Espitia Juarez, *Codificador Reed-Solomon en software.* Tesis de grado, Instituto Politécnico Nacional, México, 2012. [Online]. Available: https://goo.gl/egNKBn

[17] C. Mateos, *Simulador de un sistema de Transmisión, Recepción y ecualización de DVB-T*

en Simulink. Tesis de grado, Universidad de Sevilla. España, s.f. [Online]. Available: https://goo.gl/WPJfWW

[18] A. Delgado Gutiérrez, *Transmisión de señales de TV Digital en el Estándar Terreno DVB-T.* Universidad Poliécnica de Madrid, España, 2002. [Online]. Available: https://goo.gl/Rwpq6N

[19] D. Argüellos and J. A., *Simulación del diagrama funcional de transmisión del sistema ISDB-T, para el estudio de su estructuración.* Tesis de grado, Universidad Central de Venezuela, Venezuela., 2017. [Online]. Available: https://goo.gl/tu83My

[20] N. Pérez, *Gestión del espectro radioeléctrico para TV Digital.* Universidad de los Andes, Venezuela., 2013.

[21] S. Landeros-Ayala, S. A. Chávez-Cárdenas, and J. C. González-Sánchez, "Análisis de la eficiencia de los estándares de transmisión de televisión digital." *Ingeniería Investigación y Tecnología*, vol. 14, no. 3, pp. 335–353, 2013. [Online]. Available: https://goo.gl/sw7jxt

[22] DIBEG. (2018) Comparison of 3 DTTB systems. Digital Broadcasting Experts Group. [Online]. Available: https://goo.gl/rJomDY

[23] CRC, *Definición de las especificaciones técnicas de la TDT en Colombia.* Comisión de Regulación de Comunicaciones, Colombia., 2012. [Online]. Available: https://goo.gl/A5iy6T

[24] R. G. Acosta Arias, *Estudio Teórico Practico de los códigos no binario de Reeds-Solomon.* Tesis de grado, Escuela Politécnica Nacional, Ecuador., 1994. [Online]. Available: https://goo.gl/nMohzK

[25] MathWorks. (2018) Communications toolbox – examples. The MathWorks, Inc. [Online]. Available: https://goo.gl/RY85fW

[26] A. F. Padilla Narváez, *Detección y corrección de errores en códigos convolucionales mediante el algoritmo de Viterbi usando una microcomputadora.* Tesis de grado, Escuela Politécnica Nacional, Ecuador., 1985. [Online]. Available: https://goo.gl/9nLXYm

[27] L. Arnone, C. Gayoso, C. González, J. C. García, and J. Castiñeira, *Diseño De Un Decodificador Viterbi Para Ser Utilizado En Enlaces Infrarrojos.* Universidad Nacional del Mar del Plata., 2012. [Online]. Available: https://goo.gl/gK3bMk

Scientific Paper / Artículo Científico

UNIVERSIDAD POLITÉCNICA SALESIANA ECUADOR
INGENIUS
Revista de Ciencia y Tecnología
https://doi.org/10.17163/ings.n21.2019.08
pISSN: 1390-650X / eISSN: 1390-860X

MIGRATION TO NGN IN THE GRANMA PROVINCE

MIGRACIÓN HACIA NGN EN LA PROVINCIA GRANMA

Randy Verdecia Peña[1]

Abstract

Due to the need of introducing and integrating the province network into a Next Generation Network (NGN), as a solution to the deficiencies of its infrastructure, in this paper a NGN for Granma province is proposed, based on its current conditions and considering the existence of the IP/ MPLS national backbone as vehicle. First, the NGN model structure features, facilities and signaling protocols are analyzed. Then, a detailed analysis of the equipment proposed by the manufacturer Huawei is performed, evaluating the availability and potentials of this technology. At last, elements that contribute to the migration of the current telecommunications network in Granma Province to a NGN are discussed.

Palabras clave: Granma Province, Solution, Next Generation Network (NGN), IP/MPLS, Multiservice Access Node (MSAN), NGN migration.

Resumen

Debido a la necesidad de introducción e integración de la red de la provincia Granma, hacia una red NGN, como solución a las deficiencias en la infraestructura de la misma, en el presente trabajo se brinda una propuesta de Red de Nueva Generación para la provincia Granma partiendo de las condiciones actuales de esta y considerando la existencia del dorsal nacional IP/MPLS como transporte. Primeramente, se analiza la estructura del modelo NGN, así como sus características, facilidades y protocolos de señalización. Posteriormente se realiza un profundo análisis del equipamiento propuesto por el fabricante Huawei, evaluando la disponibilidad y las potencialidades de esta tecnología. Finalmente, se exponen elementos que contribuyen a la migración de la red de telecomunicaciones actual de Granma hacia una red NGN.

Keywords: Provincia Granma, solución, red de nueva generación (NGN), IP/MPLS, nodo de acceso multiservicio (MSAN), migración hacia NGN.

[1,*] Department of Electrical Engineering, Center of Telecommunication Studies (CETUC), Pontificia Universidad Católica de Río de Janeiro. Río de Janeiro - Brazil. Corresponding author ✉: randy.verdecia@cetuc.puc-rio.br. http://orcid.org/0000-0003-4798-2681.

Received: 17-12-2018, accepted after review: 05-11-2018

Suggested citation: Verdecia Peña, R. (2019). «Migration to NGN in the Granma province». INGENIUS. N.°21, (january-june). pp. 78-87. DOI: https://doi.org/10.17163/ings.n21.2019.08.

1. Introduction

Nowadays, the telecommunications sector has been in significant and intense evolution, mainly due to the variable and increasingly demanding requirements of the users [1]. This evolution implies that telecomm operators should continuously improve their networks in order to fulfill the needs of users who expect more and better services [2, 3].

On the side of the demand, the growth has been propelled by the involvement of telecommunication and information technology in all facets of human life, in all sectors of economic and social activities [4–6], public administration [7], public service supply and management of public infrastructure [8], education [9, 10], health [11] and cultural expression, management of the environment and emergencies, either natural or man-made. From the supply side, the growth has been encouraged by the fast technologic evolution that continuously improves the efficiency of existing products, systems and services, and lays the foundations for a constant flow of innovations in each of these sectors [12].

In recent years there has been a continuous increase on the volume of information traffic in telecommunication networks, mainly due to the proliferation of new applications that combine voice, data and video. The data traffic (demand of the market) increases, both in the residential and corporate segments, mainly as a result of the combination of traditional data services, Internet traffic and e-commerce. This increase in the demand of bandwidth, together with the request for good performance of the associated services, requires a reassessment of existent public networks and a project to fulfill the demands. In terms of evolution, the Next Generation Network (NGN) is a step towards the replacement of the Public Switched Telephone Network (PSTN) by an IP (Internet Protocol) network, which is packet-based. In this regard, the NGN integrates the TDM (Time Division Multiple) voice network and the packet network based on IP/ATM (Internet Protocol/ Asynchronous Transfer Mode) [3, 13].

In Cuba, the Cuban Telecommunication Company (ETECSA) has been in charge of the development of the telephony infrastructure and data networks. For some years now, ETECSA started an intensive investment plan aimed at the implementation of modern solutions that lead to the integration of telephony and data services in a unique system, thus improving the throughput to users [14].

One of the main defects of the telecommunication network in the Granma Province is the coexistence of two networks, namely, telephony and data. This complicates the resources management and hinders, in many cases, the implementation of new services based on the IP technology. Based on this discussion, the objective of this research is to propose a solution for migrating the telecommunication network of the Granma Province to a NGN.

2. Materials and methods

The telecommunication network of the Granma Province is mainly constituted by four loops; 93% of the municipalities use optic fiber as transmission media, which employs SDH (Synchronous Digital Hierarchy) as transportation technology. This network has 63 commutation elements, which are implemented on 80 Huawei transmission devices such as: OSN 3500, OSN 2500, Metro 2050, Metro 1000, Metro 100, Metro 500. For commutation of voice the network has a provincial tandem Huawei C&C08, located in Bayamo.

On the other hand, the data network is constituted by devices DSLAM (Digital Subscriber Line Access Multiplexer) IP distributed all over the province, which are connected to the national network through a redundant link implemented on a NE-40 router, one with the Santiago de Cuba Province and the other with Holguín. All this network is based on the existence of the IP/MPLS (Multiprotocol Label Switching) national backbone as transportation network.

The NGN is a packet network capable of supplying broadband communication services, to users from different providers. Its main advantage is that all services, voice and data, operate on a single network. Its architecture is based on four fundamental layers that, together with the signaling protocols, achieve a correct functioning. Some of these protocols are the H.248, H.323, SIP [15].

A migration to NGN was proposed some years ago, in which it was recommended to use a Huawei NE40 border router, to aggregate all the network at this point. That router does not have the capability to carry out such task, since it should handle all the traffic of the province. Such work does not specify the locations at the province where the technology (MSAN IP) might be installed in order to yield the migration to this network, neither makes reference to necessary quantity of POTS, ADSL2+ y SHDSL lines. As a consequence, the transmission velocity which should be used in the different data links of the Granma Province is not calculated.

Different service providers have proposed a solution for this type of network, but Huawei offers a complete solution according to the possibilities of the country's economy. To this effect, this manufacturer has available various devices such as UMG8900, Softswitch3000, UA5000, that make this network flexible, as described in [16–18].

3. Results and discussion

Based on the current situation of the telecommunication network of the Granma Province, as well as the existence of the backbone IP/MPLS, of the Softswitch and the possibilities offered by Huawei, the migration to NGN of the Granma Province was proposed. In this proposal, a CX300 is the element that will do all the voice and data commutation. In addition, this device will be in charge of the communication with the national network. A gateway UMG8900 with 32 E1 flows is located in the digital exchange C&C08, and this element will be used to communicate the IP world with the TDM. Other elements used are the MSAN IP, which are deployed all over the province.

The actual solution is maintained for data subscribers since the DSLAM IP will stay for connectivity, and will be inserted in the IP world through the border router like the MSAN IP. In order to extend the services of the NGN to all the URA connected to the C&C08, all the equipment must support NGN functionalities. There are in the province devices RSM, RSP, ESM, OLT and the Alcatel exchange, that do not support NGN functionalities; as a consequence, the segments of the network that involve such equipment will not benefit from all the advantages of the solution. Therefore, it is necessary that the consolidation stage of the NGN includes their successive replacement.

A call from the current PSTN of Granma Province telephone exchange with the NGN world (external to this province) will be made through the UMG (used as media gateway); the traffic will be directed by the border router located at Bayamo, which will travel through the IP/MPLS backbone to his destination. On the contrary, a territorial call from the new NGN segment to the PSTN and vice versa will be established through the UMG, whose routing is guaranteed in the border router located at the province, without leaving to the backbone IP/MPLS. The complete control of establishing the call and metering, among other network supervising actions, will be carried out by the two softswitches.

The Figure 1 illustrates the proposed migration to NGN for Granma Province. The service provider will be Huawei, since it offers a more complete solution, at a reasonable cost consistent with the current economic situation of Cuba. It is proposed that the digital exchange TDM C&C08 and the UMG 8900 are located in the same site; the latter will be used as the gateway of the TDM C&C08, allowing the communication between the TDM and IP users. In addition, two 24-port S5328 lanswitches connected in stack will be installed in the same premises, with the purpose of adding all the services supplied by the MSAN IP which will be also located in the same site. It is suggested to foresee future expansions of the MSAN IP and the gradual migration of the subscribers connected to the C&C08 towards NGN.

In the site of the CMT it is proposed to locate the Huawei CX 300, which will carry out all provincial network commutations, and will have aggregation functionalities for both networks, voice and data. It will connect via two G/E links to the lanswitches S5328 and through F/E to the provincial SDH network using the OSN 3500 device located at the CMT, and with national SDH network through two G/E links using the OSN 7500. The CX 300 has a backplane velocity of 48 Gbps, and uses the routing protocols OSPF, IS-IS and BGPv4. In the proposed migration, the MSAN TDM, the URA and other equipment that is currently used to provide services to the municipalities in the province will be maintained. A total of 8 MSAN IP will be installed, including one in the site of the digital exchange to provide service to 24000 new subscribers in all the province, even though in this solution only 9408 services will be installed, between fixed telephony and data.

Future actions should be directed toward the consolidation of the NGN networks, thus the current MSAN with TDM functionality should be gradually migrated to the IP world, eliminating the function carried out nowadays by the C&C08 by connecting them directly to the CX 300 router; similarly, all new sites added to the network should already include IP functionalities. Only 8 sites will be installed in this proposal, due to three main reasons: technological change, low telephone density and network expansion. Table 1 shows the equipment to be used and their location.

Erlang's theory is applicable to the basic telephone service, independently of the support, medium or technology used to supply such service; its validity is determined by the behavior of the users. It is applied to the service, not to the technology. There are two theories: losses (Erlang B) and queuing (Erlang C). Therefore, it is applicable to dimensioning the resources that will support the NGN; in this case, the transmission velocity VoIP required to carry traffic on this type of network. In traditional TDM networks, when calculating the quantity of required circuits to carry a particular traffic with one percent losses, the transmission velocity is being indirectly calculated because each circuit is a PCM channel with a transmission velocity of 64 Kbps.

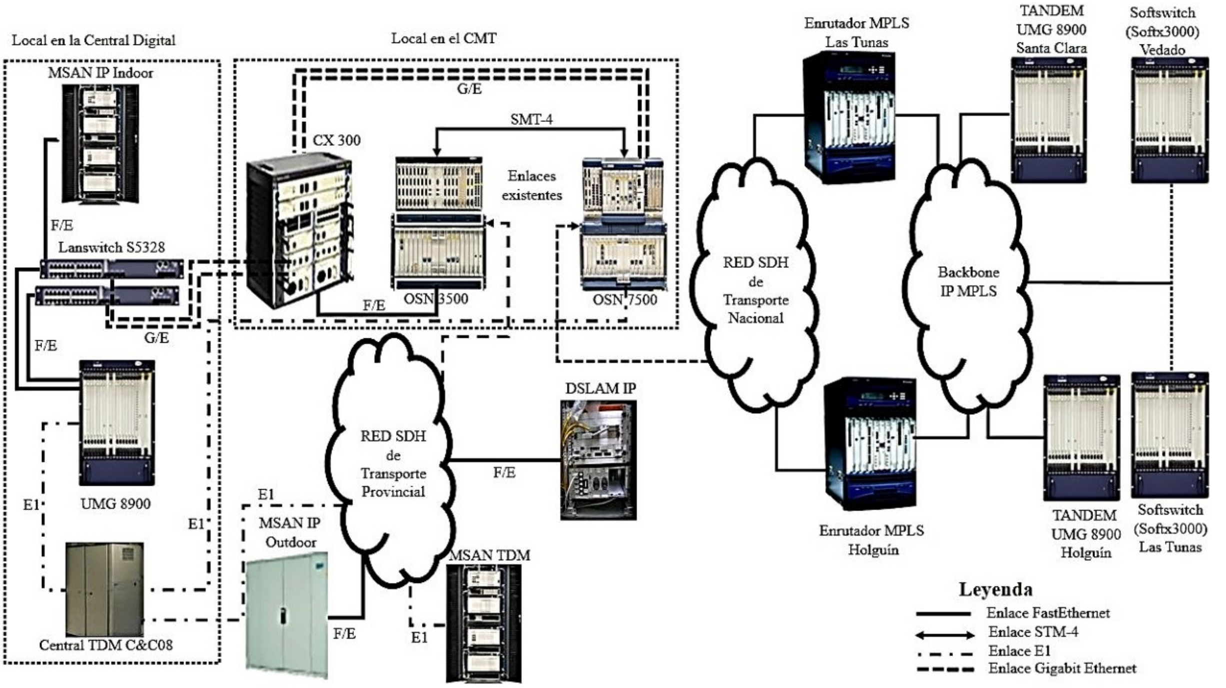

Figure 1. Proposed migration to NGN for Granma Province, Huawei provider.

Table 1. Location of the MSAN IP

Equipment	Location	Transmission device
MSAN IP (Inside)	Bayamo	Metro 1000
MSAN IP (Inside)	Cauto Cristo	Metro 1000
MSAN IP (Inside)	Río Cauto	Metro 1000
MSAN IP (Inside)	Niquero	Metro 1000
MSAN IP (Inside)	Manzanillo	OSN 3500
MSAN IP (Outside)	Vázquez	OSN 500
MSAN IP (Outside)	Camilo 1	OSN 500
MSAN IP (Outside)	Camilo 2	OSN 500

Table 2. Number of lines and necessary transmission velocities

Locations	N.° lines	Voice (Mbps)	Data (Mbps)	Voice + Data (Mbps)
Bayamo	896	12	26	38
Cauto Cristo	864	12	22	34
Río Cauto	1216	15	34	49
Niquero	960	13	26	39
Manzanillo	896	12	26	38
Vázquez	960	13	26	39
Camilo I	960	13	26	39
Camilo II	960	13	26	39

For calculating the velocity of transmission of the voice, it is necessary to take into account that each protocol or layer encapsulates an IP packet by adding some headings to be able to process and route it. As a consequence, the packet to be transmitted has a bit size much greater than the Payload (usable load of the voice). Each CODEC has a predetermined transmission velocity of voice packets; the required velocity should be higher due to the increase in the size of the packet. In order to transmit the voice from a MSAN IP through the IP network, the following protocols should be used: Layer 2 link, IEEE 802.3, IP, UDP (User Datagram Protocol) and RTP (Real-time Transport Protocol) [19].

Table 2 shows the transmission velocities calculated in [20], as well as the necessary number of lines in each of the 8 locations.

3.1. Migration of sites Camilo I and II

The Camilo Cienfuegos neighborhood is one of the greatest areas of the provincial town (Bayamo). It is a location with a high density of households and a low density of telephones (only 8.58% of demand of twisted pairs). Currently, the network is saturated with low capacity cables, as compared with the number of existent households and the demand for telephony services. The problem of the network in this zone is due to the saturation of the networks in the province: fixed, mobile, radio. In addition, there are no more ports available in the URAs at Bayamo, which results in the following facts:

- 66.67% of the households demands, at least, one telephone pair.
- 41.67% of the buildings are two-story or more.

- The remaining 33.33% demands one telephone pair for two households.
- The density of the telephone service is 2.04 for every 100 inhabitants.

Figure 2 shows the network structure for Camilo Cienfuegos. For migrating this zone, it is proposed to use two Outdoor MSAN IP (Camilo Cienfuegos I y Camilo Cienfuegos II). Those MSAN IP will employ the provincial SDH network to carry the IP packets. It is also proposed to install two OSN 500 that will be utilized as transmission elements for the new network structure of the site; they will have an EFS card for Ethernet services, foreseeing future connections for data transmission associated to the external distribution area. In addition, the MSAN IP will use two control cards for narrowband services (PVM), and two for broadband services (IPMD).

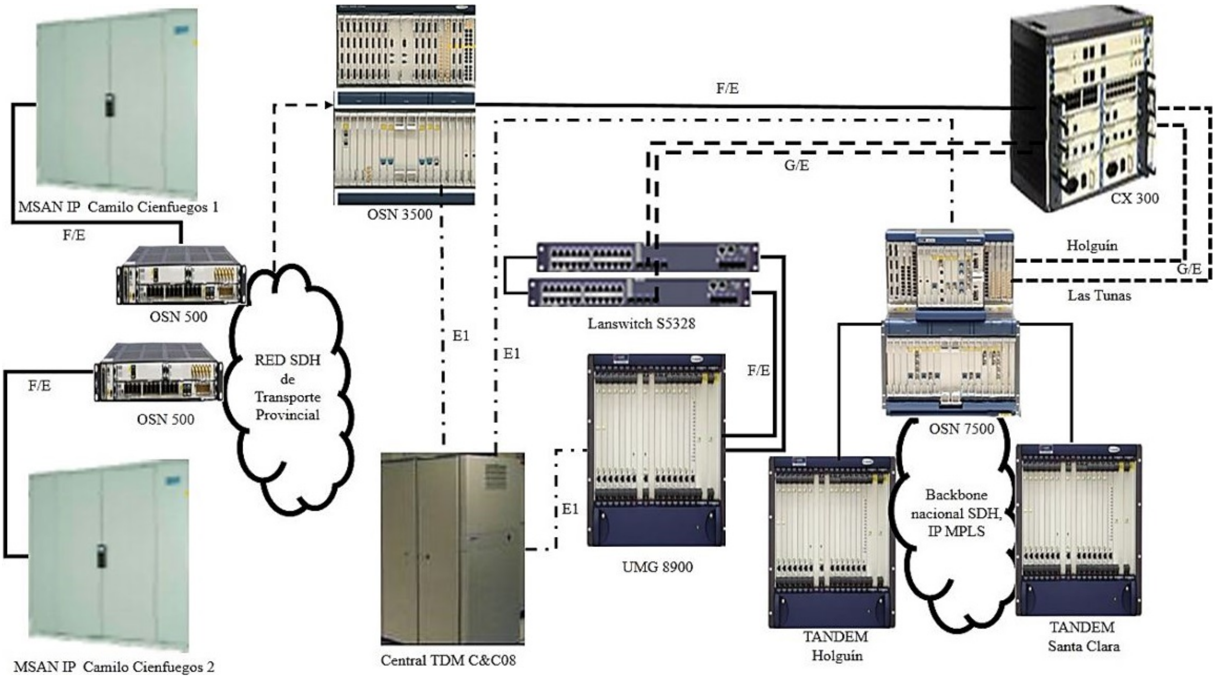

Figure 2. Proposed network for sites Camilo Cienfuegos I and II.

3.2. Migration of site Bayamo

The Bayamo site has an exchange TDM C&C08 with 51520 lines, 9040 of which are installed in the telephone center itself distributed in three RSP cabinets, with 8942 currently in operation. Besides being considered an obsolete technology, they already reached maximum capacity.

As can be seen in Figure 3, the MSAN of Bayamo will be directly connected to the s5328 lans witches, and these to the CX300, which is the device in charge of carrying out the commutation to the final destination.

The MSAN of Bayamo will have two control cards for narrowband services (PVM), and two for broadband services (IPMD). The four cards will be wired to the S5328 lanswitches, which will concentrate the traffic of the URA IP. Softswitches in El Vedado and Las Tunas will control de MSAN IP by means of the protocol H.248.

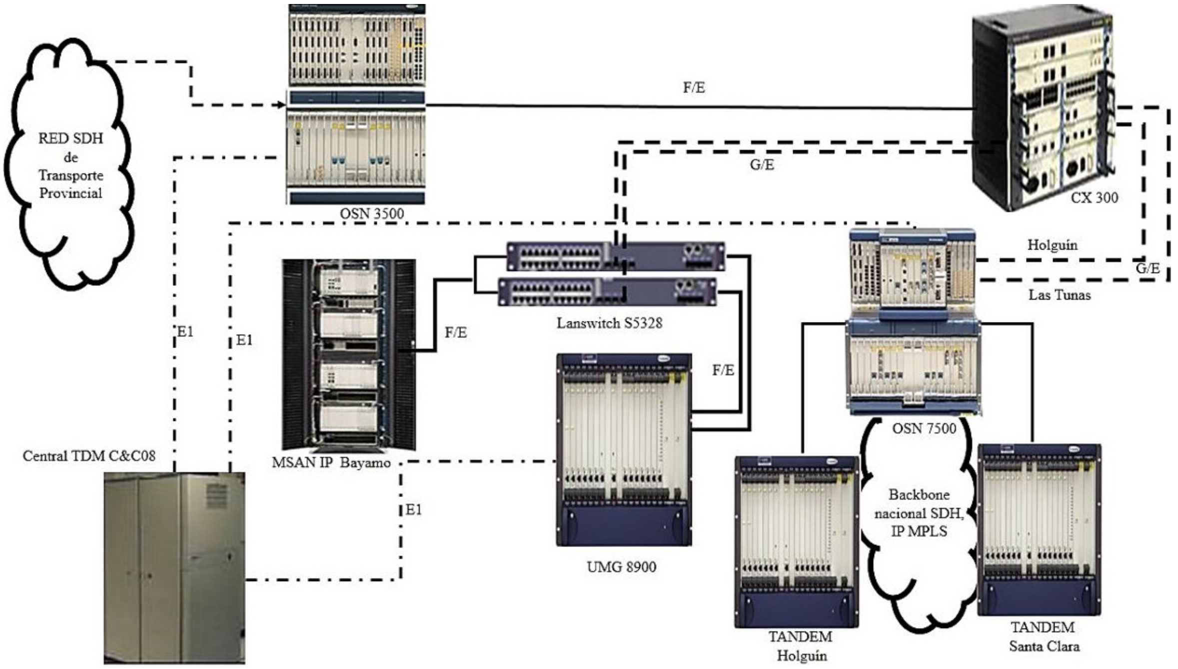

Figure 3. Proposed network for site Bayamo.

3.3. Migration of site Río Cauto

The Río Cauto municipality currently has a URA DLC of the exchange TDM C&C08, with a total of 800 lines, 788 of which are in operation; this technology is considered obsolete.

To solve the problem in this municipality, it is necessary to completely replace the DLC technology in the site. This will be achieved through the installation of a Huawei Indoor MSAN IP type F02A HABA with rear wiring, which will be controlled by softswitches in El Vedado and Las Tunas. The MSAN IP will have a S3328 lanswitch to receive the wiring from the FE interfaces of the PVM and IPMD control cards. The transmission equipment that will be used is the Metro 1000 currently installed in the municipality, as shown in Figure 4.

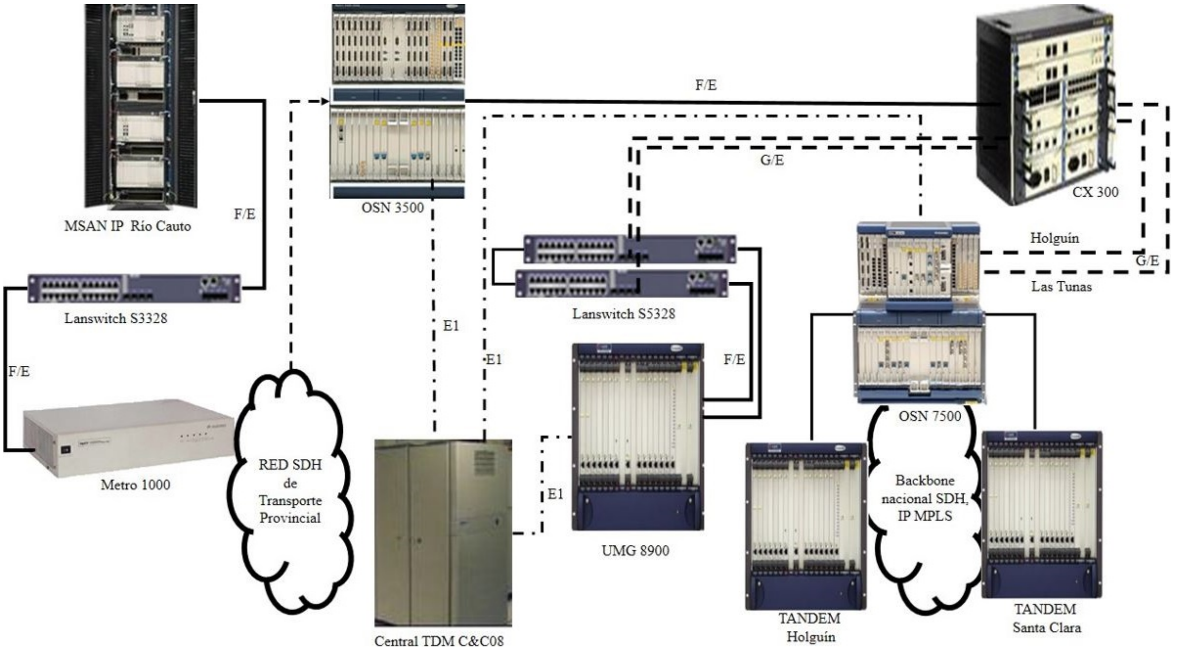

Figure 4. Proposed network for site Río Cauto.

3.4. Migration of site Cauto Cristo

Cauto Cristo has an exchange CDPC A4300 of small capacity, linked to the central TDM C&C08. It has 704 lines installed, of which 666 are in operation in this equipment which is considered obsolete technology. Therefore, a Huawei MSAN IP will be installed to make a technological change in the CDPC.

Figure 5 shows the structure of the network of Cauto Cristo, where the MSAN with rear wiring will have a S3328 lanswitch to receive the wires from the FE interfaces from the ports of the broadband (IPMD) and narrowband (PVM) control cards. The MSAN IP will have 864 POTS, 160 ADSL2+ and 16 SHDSL lines.

The POTS lines in the cards H60D00VASL01 will be for 64 subscribers, while the ADSL2+ lines in the cards H60DCSRB6101 (which in this case operate as a combo because it also houses POTS subscribers) will be for 32 subscribers. The lines SHDSL (H60-SHLB) have 16 service ports. A Metro 1000 is proposed as the transmission element for the site, which will be used to travel on the SDH network of the province.

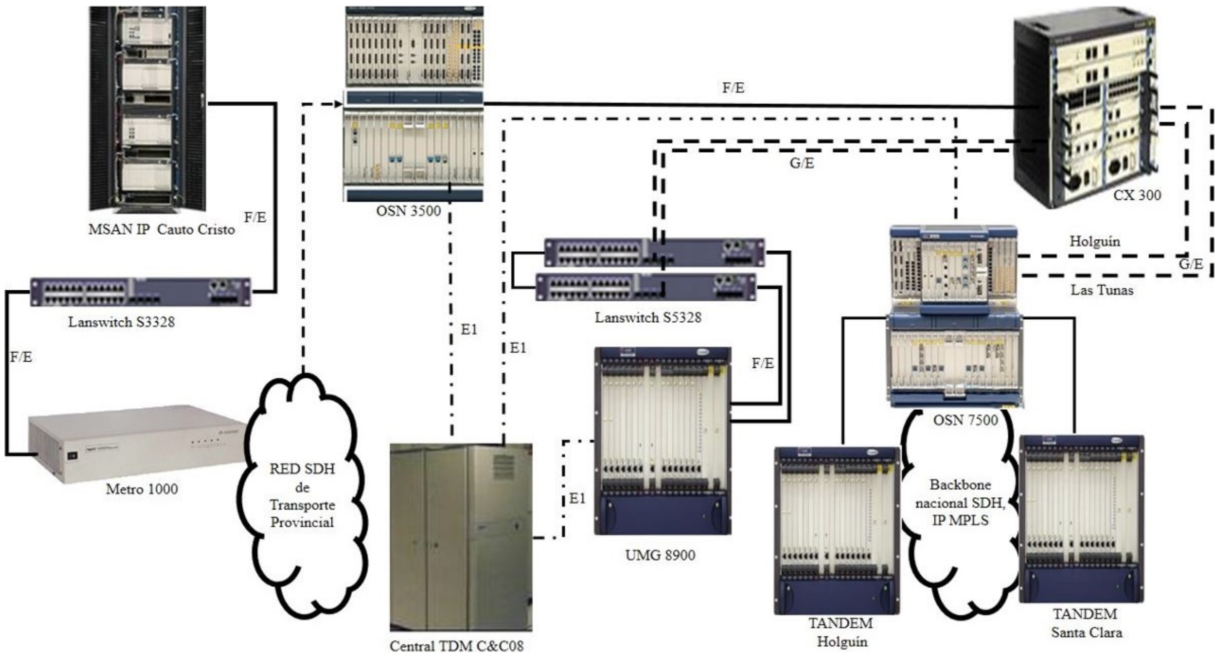

Figure 5. Proposed network for site Cauto Cristo.

3.5. Migration of site Manzanillo

The Manzanillo municipality has a URA in the exchange TDM C&C08 that has 5776 lines, 5447 of which are in operation, and distributed in four cabinets of an ESM, which is considered obsolete technology. In order to increase the number of lines in the city, it is proposed to install a Huawei MSAN IP type F02A HABA with rear wiring, inserted in the solution of the province NGN. This device will be controlled by softswitches in El Vedado and Las Tunas, by means of the protocol H.248.

For this increment, it has been devised the acquisition of a MSAN IP UA5000 that will have a S3328 lanswitch to receive the wiring from the FE interfaces from the ports of the broadband (IPMD) and narrowband (PVM) control cards, with 896 POTS, 192 ADSL2+ and 16 SHDSL lines.

The POTS lines in the cards H60D00VASL01 will be for 64 subscribers, while the ADSL2+ lines in the cards H60DCSRB6101 (which in this work are called combo because they also may house POTS subscribers) will be for 32 subscribers. The lines SHDSL (H60-SHLB) will have 16 service ports. The OSN 3500 in service will be used for the transmission, thus carrying the traffic on the provincial SDH network, as shown in Figure 6.

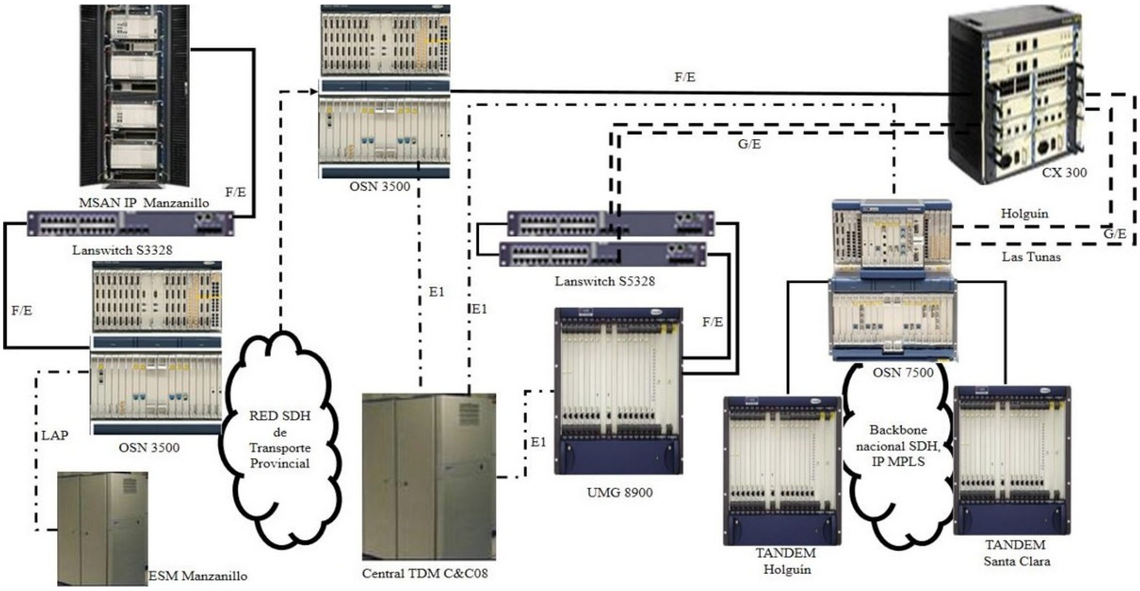

Figure 6. Proposed network for site Manzanillo.

3.6. Migration of site Vazquez

The neighborhood Vázquez is one of the largest of the Manzanillo municipality. It is a zone of high density of households, and low density of telephones. To overcome the situation previously described, a MSAN IP of type F01D1000 with 960 POTS, 192 ADSL2+ (combos) and 16 SHDSL (pure data) lines, equipped to offer VoIP services. The MSAN will use narrowband (PVM) and broadband (IPMD) control cards.

Figure 7 shows the structure of the network of site Vázquez. The MSAN IP will use the provincial SDH network for carrying the IP packets, and an OSN 500 is proposed as the transmission element for this zone; it will have an EFS card for the Ethernet services, foreseeing the future connections for data transmission associated to the external distribution area. The telephone and data traffic may be from the IP world to the TDM, and between worlds IP, municipal, provincial and national. The communication of this network segment with the provincial and national subscribers will travel through the provincial SDH network, in the same way as in the Camilo Cienfuegos site, using an OSN 500 as transmission element.

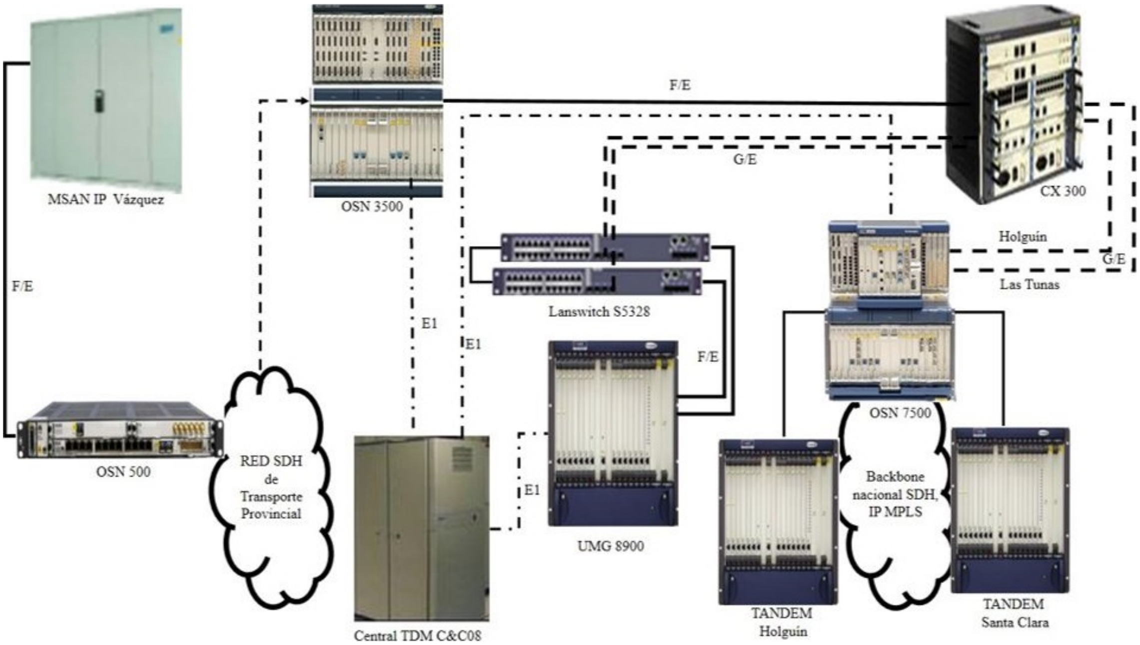

Figure 7. Proposed network for site Vázquez.

3.7. Migration of Niquero site

The MSAN will have a S3328 lanswitch to receive the wiring from the FE interfaces from the ports of the broadband (IPMD) and narrowband (PVM) control cards, with 896 POTS, 192 ADSL2+ and 16 SHDSL lines. This equipment will comprise 960 POTS, 192 ADSL2+ and 16 SHDSL lines. It will be inserted in the provincial transport network by means of a Metro 1000 that is operating in the site, as shown Figure 8.

Currently, the Niquero coastal municipality has a URA RSM in the exchange TDM C&C08 that comprises 1216 lines, 1153 of which are in operation. Since this is an obsolete equipment, its internal hardware cannot be expanded.

In order to expand the number of lines in this part of the Granma province, a Huawei MSAN IP F02A HABA with rear wiring will be included in the Huawei NGN solution for the province.

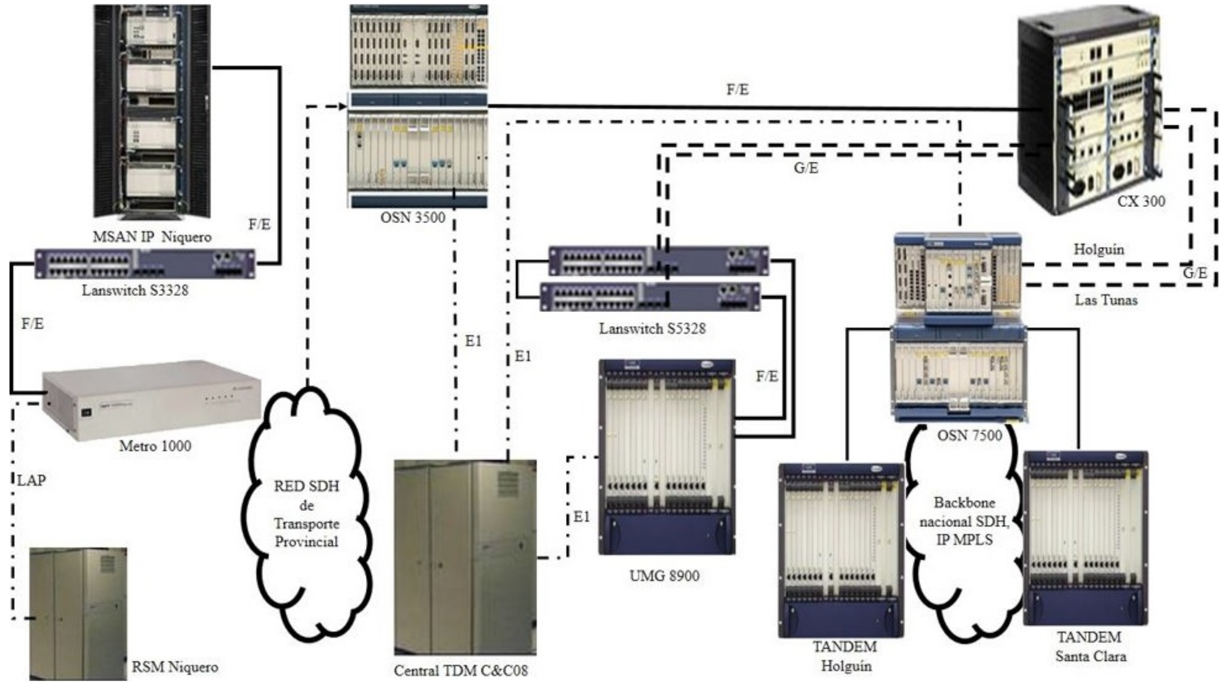

Figure 8. Proposed network for site Niquero.

4. Conclusions

The migration proposal toward NGN of the Granma Province telephony and data network, reuses the current telecommunication infrastructure to the maximum extent possible, thus allowing significant savings in the budget allocated to the project.

The proposed solution does not lead to the total migration of the Granma Province to NGN, because the capital to cover all sites is not completely available; nevertheless, it lays the foundations for the rapid expansion of this technology to the places which are not reached in this phase.

The fact that more than 90% of the municipalities are connected to the national optic fiber, facilitates the future installation of the necessary NGN equipment in the sites that were not taken into account in this phase of the project.

References

[1] E. Öztürk, E. Basar, and H. A. Çirpan, "Generalized frequency division multiplexing with flexible index modulation," *IEEE Access*, vol. 5, pp. 24 727–24 746, 2017. [Online]. Available: https://doi.org/10.1109/ACCESS.2017.2768401

[2] UIT, *Informe sobre el desarrollo mundial de las telecomunicaciones 2002.* Union internacional de Telecomunicaciones, 2002. [Online]. Available: https://goo.gl/HLLi74

[3] CET, *Las telecomunicaciones y la movilidad en la sociedad de la información.* Entro de estudios de telecomunicaciones de América Latina, 2004. [Online]. Available: https://goo.gl/oGBt4P

[4] S. Jiménez and J. Lira, *Desarrollo de las Telecomunicaciones: Una Fuente para el Progreso.* Libertad y desarrollo, 2015. [Online]. Available: https://goo.gl/5HWYgT

[5] M. Rodríguez, "Crecimiento y expansión de los servicios de telecomunicaciones en argentina durante la posconvertibilidad ¿concentración económica con descentralización productiva?" *Galega de Economía*, vol. 25, no. 1, pp. 121–136, 2016. [Online]. Available: https://goo.gl/o6QmmQ

[6] A. L. Mellado Ochoa, "La infraestructura de telecomunicaciones y el desarrollo económico de los países," Master's thesis, Universidad del Pacífico, Perú, 2016. [Online]. Available: https://goo.gl/82nRgN

[7] ENS, *El sector de las telecomunicaciones: Entramado de relaciones laborales con lox gigantes colombianos*. ENS. Escuela Nacional Sindical, 2015. [Online]. Available: https://goo.gl/dDpqmo

[8] M. de Telecomunicaciones, *Plan Nacional de Telecomunicaciones y Tecnologías de la Información del Ecuador 2016-2021*. Ministerio de Telecomunicaciones y de la Sociedad de la Información, Ecuador, 2016. [Online]. Available: https://goo.gl/kJwWaa

[9] R. Verdecia Peña and M. Paneque Mojena, "Aula especializada para el fortalecimiento de la preparación integral de los trabajadores de la Empresa de Telecomunicaciones de Cuba," *Didasclia: Didáctica y Educación,*, vol. 8, no. 1, pp. 131–142, 2017. [Online]. Available: https://goo.gl/pDoKg7

[10] R. M. Hernandez, "Impacto de las tic en la educación: Retos y perspectivas," *Propósitos y Representaciones*, vol. 5, no. 1, pp. 325–347, 2017. [Online]. Available: http://dx.doi.org/10.20511/pyr2017.v5n1.149

[11] L. Y. Avella Martinez and P. P. Parra Ruiz, *Tecnologías de la Información y la Comunicación (TICS) en el sector salud*. Especialización en Administración en Salud Pública y Servicios de Salud, Universidad Nacional de Colombia., 2013. [Online]. Available: https://goo.gl/8e8eTQ

[12] G. E. Cano Pita, "Las tic en las empresas: evolución de la tecnología y cambio estructural en las organizaciones," *Dominio de las Ciencias*, vol. 4, no. 1, pp. 499–510, 2018. [Online]. Available: https://goo.gl/JFPNRs

[13] S. K. Mohapatra, "Integrated planning for next generation networks," in *2009 IFIP/IEEE International Symposium on Integrated Network Management-Workshops*, June 2009, pp. 205–210. [Online]. Available: https://doi.org/10.1109/INMW.2009.5195961

[14] O. A. Gusmán Obregón, Y. A. Marín Muro, and C. Rodríguez López, *Red de Próxima Generación. Una alternativa para la implementación de nuevos servicios en la red de telecomunicaciones de Cuba.* Facultad de Ingeniería Eléctrica. Universidad Central Marta Abreu de las Villas, Cuba., 2007. [Online]. Available: https://goo.gl/aXtjBV

[15] A. B. Johnston, *SIP: Understanding the Session Initiation Protocol*. Artech House, 2009. [Online]. Available: https://goo.gl/jCCYgk

[16] ETECSA, *U-SYS NGN*. Empresa de telecomunicaciones de CUBA S. A., 2006.

[17] HUAWEI, "U-sys softx3000 softswitch system," Huawei Technologies Proprietary, Tech. Rep., 2004. [Online]. Available: https://goo.gl/xSp4Wy

[18] Huawei, "System description of umg5900," Huawei Technologies, Tech. Rep., 2004. [Online]. Available: https://goo.gl/HXAXGU

[19] O. Gonzalez Soto, *Concepto y arquitectura de las Redes NGN*. International Telecommunications Union (ITU), 2006. [Online]. Available: https://goo.gl/RZ4sD7

[20] R. Verdecia Peña, *Propuesta para la migración hacia NGN en la provincia de Granma*. Tesis presentada en opción al título de Ingeniero en Telecomunicaciones y Electrónica, Universidad de Oriente Sede ISPJAM, Santiago de Cuba, Cuba, 2014.

Scientific Paper / Artículo Científico

UNIVERSIDAD POLITÉCNICA SALESIANA ECUADOR
INGENIUS
Revista de Ciencia y Tecnología
https://doi.org/10.17163/ings.n21.2019.09
pISSN: 1390-650X / eISSN: 1390-860X

ANALYSIS OF ELECTROLYTE OF AN AUTOMOTIVE ACCUMULATOR AT DIFFERENT TEMPERATURES AT START CONDITION

ANÁLISIS DEL ELECTROLITO DEL ACUMULADOR AUTOMOTRIZ A DIFERENTES TEMPERATURAS EN CONDICIÓN DE ENCENDIDO

Johnny Pancha[1,*], Vicente Rojas[1], Vicente Romero[1], Jorge Nejer[1]

Abstract

An automotive battery of the acid lead type is an element that generates an electromotive force capable of supplying energy to the entire electrical system of the vehicle. In this investigation, the behavior of the specific density of the electrolyte during the start-up condition of a heat engine is analyzed; the operating temperature gradient at which the battery can be exposed is also considered as a variable. According to the results, the electrolyte temperature is inversely proportional to its density in the cells of the accumulator during the start-up condition. It is concluded that external conditions, such as the temperature, can directly affect the density and electrical conditions of an accumulator, and can identify the behavior of these during the operation in a vehicle.

Palabras clave: Starting, Battery, Leaf acid, Temperature.

Resumen

Una batería automotriz del tipo plomo ácido es un elemento que genera una fuerza electromotriz capaz de abastecer de energía a todo el sistema eléctrico del vehículo. En el presente estudio se analiza el comportamiento de la densidad específica del electrolito durante la condición de arranque de un motor térmico; además, se considera como una variable, el gradiente de temperatura de funcionamiento que puede estar expuesto una batería automotriz. Obteniendo resultados de una variación inversamente proporcional del comportamiento de la temperatura del electrolito y su densidad en las Cells del acumulador durante la condición de arranque. Se concluye que las condiciones externas como la temperatura pueden afectar directamente a la densidad y las condiciones eléctricas de un acumulador, así como identificar el comportamiento de estas durante el funcionamiento en un vehículo.

Keywords: arranque, batería, electrolito, temperatura.

[1,*]Faculty of Mechanics, Escuela Superior Politécnica del Chimborazo, Ecuador. Corresponding author ✉: johnny.pancha@espoch.edu.ec. http://orcid.org/0000-0001-7320-2154, http://orcid.org/0000-0001-5658-3055, http://orcid.org/0000-0003-2317-7071, http://orcid.org/0000-0002-5744-2585.

Received: 15-11-2018, accepted after review: 17-12-2018

Suggested citation: Pancha, J.; Rojas, V.; Romero, V. y Nejer, J. (2019). «Analysis of electrolyte of an automotive accumulator at different temperatures at start condition». INGENIUS. N.°21, (january-june). pp. 88-94. DOI: https://doi.org/10.17163/ings.n21.2019.09.

1. Introduction

An automotive battery has been designed to work together with the starting motor, when an internal combustion engine needs to turn on. In particular, the battery should have the capacity of supplying energy to produce the initial turns of the engine. Therefore, during the start-up condition the battery should have its highest performance and correlation between the specific density of the electrolyte of the accumulator and the temperature [1]. Such specific density is related with the state of charge of a battery and the interaction with the active material, and the temperature is related with the voltage and the intensity of current it can supply [2]. The variation in the temperature gradient and the start-up condition give results that can be related with the obtained in the study of the electrolyte gasification of the accumulator during charging operation and the temperature of exposure [3], which gives additional data about the behavior in a rather common condition during the operation of an automotive. It is very important to study the effect of the temperature on the operation of the negative and positive plates, during the process of charge, discharge, behavior at start-up and external conditions such as temperature that affect its useful life and, besides, when being exposed to an electrolyte like sulfuric acid [1].

1.1. Automotive battery

Essential element in the electric system of the vehicle, designed to supply energy in some electrical conditions, being the most important to provide start-up capability to achieve the key objective of turning on the engine [4]. In an accumulator, the start-up capability is effective for a time period of 10 seconds, during which it should supply the maximum possible amperage that it can deliver based on the internal design, in the electrical condition that occurs when the initial turns of the engine are produced. This test, known as start-up condition, has been standardized at an ambient temperature of 25°C, while the test carried out at a temperature between 0°C and –18°C is known as cold start-up condition [5].

1.2. Specific density

In 1860, Gaston Plante combined Pb / $PbSO_4$ with an electrode of PbO_2 / $PbSO_4$ in a solution of sulfuric acid, and obtained a source of electrochemical energy with a significant electromotive force [4].

The temperature is an important factor that influences the electromotive force of an accumulator, thus the automotive batteries exposed to low temperatures have internal design problems them prevent them from working normally; this is the characteristic of the vehicles in cold regions [6]. On the other hand, the exposition of the accumulator to high temperatures accelerates the deterioration of the internal elements and the rusting of positive plates.

The electrical resistance, specifically the resistivity of the H_2SO_4 electrolyte, is one of the basic parameters that determine the internal resistance and the power of each of the cells in an acid lead battery [7]. When the internal resistance of the cell is high, a significant portion of the usable energy is consumed inside the own cell, i.e. the energy is dissipated as heat when the electrical current flows through the cell, depending on the concentration and temperature of the electrolyte [7].

1.3. Temperature

It is considered that the electrolyte ($H_2SO_4 + H_2O$) has a density of 1280 g/cm^3, i.e. 1280 times heavier than a similar volume of pure water, when both liquids are at the same temperature [8].

In automotive diagnosis, the most useful and effective tool to know the state of the specific density is known as hydrometer [5]. A density between 1290 g/cm^3 and 1270 g/cm^3 indicates that the accumulator is completely charged, while a density between 1240 g/cm^3 and 1200 g/cm^3 indicates that the charge has reduced. When the specific density obtained in the hydrometer is smaller than 1150 g/cm^3, it is considered that the battery is discharged. These values are established for a temperature of the electrolyte between 20°C and 25°C [5]. Therefore, a correction of 0.0035 units should be applied in the relative density, for every 5 degrees of variation in the temperature of the electrolyte above 25°C [5].

1.4. Start-up condition

During the start-up condition of a heat engine, the starting motor is the fundamental device since it is responsible of producing the initial turns of the engine thus it can become on [5]. A particular behavior of the voltage occurs in the electrical system when the motor initiates turning, as can be seen in Figure 1. The ISO 16750-2 standard establishes that during the start-up condition, the voltage oscillates for a standardized time between 3 and 10 seconds during which there is a high demand in start-up intensity. This causes that the battery discharges due to the work done, and this is reflected in the specific density of the electrolyte [9].

The voltage of the electric system decreases momentarily during engine start-up. The particular value of the voltage depends on the condition of the battery. The values may decrease at a level between 10.5 and 10.9 volts when the accumulator is in good condition [5].

The temperature is determining in the performance of the accumulator, which is better at high temperature as compared to the capability of cold start-up [9]. The specific electrical resistance (resistivity) of the H_2SO_4 electrolyte is one of the essential parameters that determine the internal resistance and the power an acid lead cell.

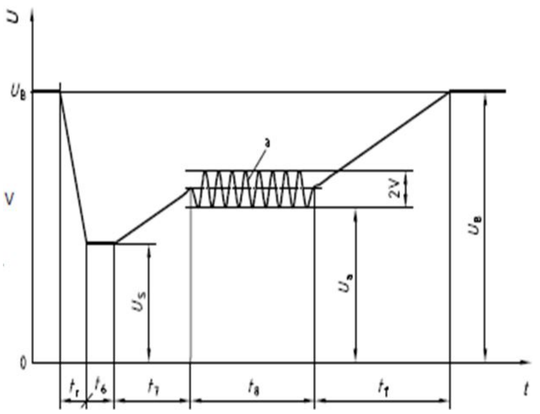

Figure 1. Behavior of the voltage of the electric circuit during start-up of the heat engine [4].

In an acid lead accumulator, the sulfate is a closed system that can be found in the plates or in the electrolyte, according to the state of charge or the operating condition. If the battery is completely charged, the sulfate is in the electrolyte; on the other hand, if the battery is discharged, the sulfate is in the plates. The final result of the specific density is a picture related to the voltage and, therefore, to the state of charge [9].

The objective of this analysis is to know the behavior of the specific density of the electrolyte of an automotive accumulator during the start-up condition, causing a variation of the ambient temperature to which the battery is exposed. In general, the analysis of the specific density of the electrolyte is carried out in order to know the state of the charge, but searching for an analysis of its effect when it is subject to a change in ambient temperature during the storage process, and confirm the structural change in the density and its relationship with the voltage and intensity offered by the battery [10].

This study searches to identify the behavior of the specific density of the battery during the start-up condition, to find sign that can direct this analysis toward initial research elements, and future improvements regarding the design of automotive batteries. There are no studies about the behavior of the specific density of acid lead batteries during start-up, thus it is desired to obtain values based on the variation of the temperature.

2. Materials and methods

The research is based on an experimental method, which comprises the analysis of the behavior of the specific density of an automotive battery during the start-up condition, for different values of ambient temperature. To achieve this purpose, the specific density has been measured in the six cells that constitute the automotive battery in optimal operating conditions, with a nominal voltage of 12 volts.

The process applied is for determining, in a practical manner, the status of a battery during the start-up of an engine. At the beginning of the study, the value of the specific density in each cell is determined at the initial rest condition. Then, the engine start-up process is initiated, but avoiding to completely turning it on. This test is repeated 6 times, and the specific density of the cells is measured at the end of each test. It is important to mention that the temperature of the electrolyte is also registered before and after the test, to further fit a model that gives the specific density as a function of transition temperature.

3. Results and discussion

3.1. High temperature condition

The external temperature of the battery is progressively increased, for which a thermal heater is used to simulate ambient temperature. Then, the value of specific density for each of the cells in the battery is registered. Table 1 shows the data obtained at 20°C, and the fitted values calculated as a function of temperature [5].

The fitted values of density are calculated based on the percentage of loss and expansion, but the obtained and fitted values in each test and measurement are analyzed during the process.

Figure 2 illustrates the behavior of the density for a temperature stable at 55°C, which indicates a significant change in the first block of cells, but a greater stability mostly on the central cells, and the greatest stability for the group of cells close to the negative terminal.

Table 1. Density and temperature before the start-up

Cell	**Ambient temperature °C**	**Temperature of the battery box °C**	**Temperature of the electrolite °C**	**Specific density g/cm^3**	**Voltage of the battery (V)**	**Fifted specific density g/cm^3**
1	55	44	21,7	1,2	11,62	1,198
2	55	44	19,3	1,19	11,67	1,186
3	55	44	19,3	1,2	11,57	1,196
4	55	44	19,3	1,2	11,57	1,196
5	55	44	19,4	1,175	11,6	1,171
6	55	44	20,5	1,2	11,57	1,197

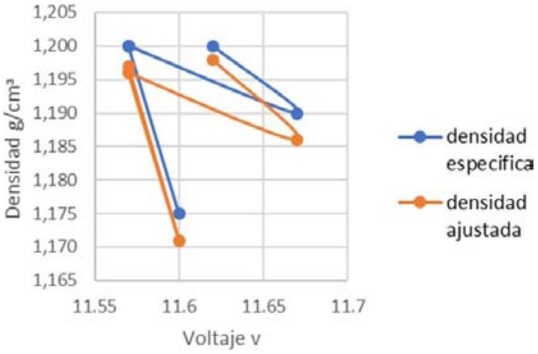

Figure 2. Plot of the behavior of the density before start-up at 55 °C.

Table 2 shows the results obtained after carrying out the continuous start-up process, to observe the stability condition of the accumulator and the fitted values calculated as a function of temperature [5].

Table 2. Density and temperature after the start-up

Cell	Ambient temperature °C	Temperature of the battery box °C	Temperature of the electrolite °C	Specific density g/cm^3	Voltage of the battery (V)	Fifted specific density g/cm^3
1	55	44	20	1,190	11,62	1,187
2	55	44	18,9	1,180	11,67	1,176
3	55	44	19	1,205	11,57	1,201
4	55	44	18,6	1,210	11,57	1,206
5	55	44	19,9	1,180	11,6	1,176
6	55	44	22,1	1,175	11,57	1,173

Figure 3 shows the behavior of the density for a temperature stable at 55°C, keeping also stable the voltage of the battery when the start-up process is generated. This results in a notable change in the first block of cells, stability in the central cells, and also an important change for the group of cells close to the negative terminal.

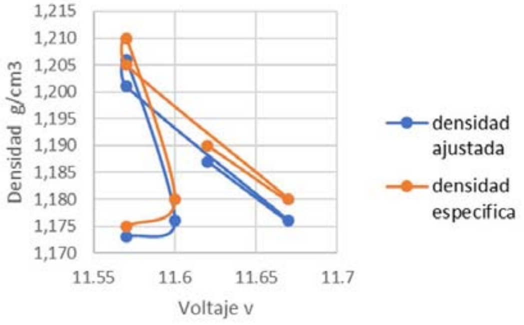

Figure 3. Plot of the behavior of the density after start-up at 55 C.

3.2. CLow temperature condition

The low temperature condition is achieved by enclosing the battery in a capsule with dry ice until the indicated value of temperature is reached. In order to register the data for this condition, the cells are subject to a temperature variation smaller than in the previous test, being stabilized at a temperature of 1 °C. Table 3 includes the obtained and fitted values calculated as a function of the temperature [5].

Table 3. Density and temperature after the start-up

Cell	Ambient temperature °C	Temperature of the battery box °C	Temperature of the electrolite °C	Specific density g/cm^3	Voltage of the battery (V)	Fifted specific density g/cm^3
1	-2	1,4	6,4	1,250	11,17	1,231
2	-2	1,4	7,7	1,245	11,24	1,226
3	-2	1,4	8,3	1,250	11,24	1,231
4	-2	1,4	8,9	1,250	11,11	1,231
5	-2	1,4	9	1,245	11,2	1,226
6	-2	1,4	9,3	1,225	11,23	1,206

Figure 4 shows the behavior of the density for a temperature stable at -2 °C: the behavior of the electrolyte at low temperatures is more stable than for high temperatures.

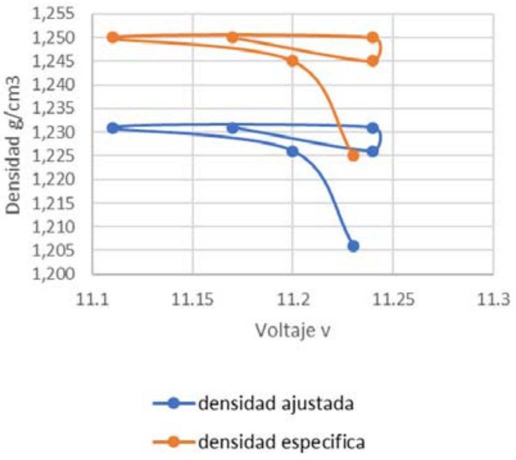

Figure 4. Plot of the behavior of the density before start-up at -2 °C.

Table 4 shows the results obtained after carrying out the continuous start-up process, to observe the stability condition of the accumulator and the fitted values calculated as a function of temperature [5].

Table 4. Density and temperature after the start-up

Cell	Ambient temperature °C	Temperature of the battery box °C	Temperature of the electrolite °C	Specific density g/cm^3	Voltage of the battery (V)	Fifted specific density g/cm^3
1	-2	1,4	6,4	1,230	12,46	1,211
2	-2	1,4	7,7	1,215	12,28	1,196
3	-2	1,4	8,3	1,250	11,43	1,231
4	-2	1,4	8,9	1,275	11,27	1,256
5	-2	1,4	9	1,250	11,31	1,231
6	-2	1,4	9,3	1,265	11,3	1,246

Figure 5 shows the behavior of the density for a temperature stable at -2°C, after the start-up process; there was a considerable drop on the values of electrolytic density and voltage, even more for the group of cells in the positive terminal. This indicates a minor reaction and an effort in the discharge process of the battery during this phase of the test.

3.3. Ambient temperature condition

The data for an ambient temperature of 27°C are obtained by means of the process established in previous cases. Table 5 shows the obtained values of specific density and temperature [5].

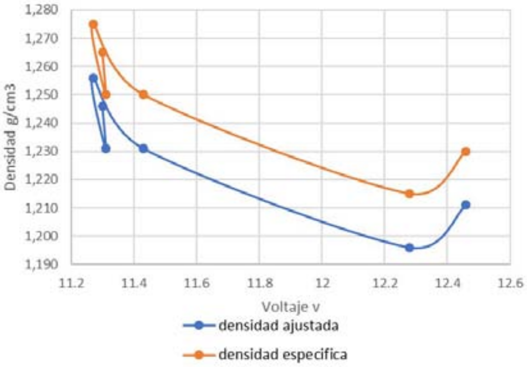

Figure 5. Plot of the behavior of the density after start-up at -2 °C

Figure 6 shows the behavior of the density for a temperature stable at 20°C, indicating stability of the voltage and of the density of the battery.

In addition, it can be observed that there is cyclic flow behavior of the electrolyte density, for more than one stable value of the voltage of the battery, which remains stable regardless of the start-up condition.

Table 5. Density and temperature after the start-up

Cell	Ambient temperature °C	Temperature of the battery box °C	Temperature of the electrolite °C	Specific density g/cm^3	Voltage of the battery (V)	Fifted specific density g/cm^3
1	20	27,2	14,06	1,200	11,17	1,197
2	20	27,2	14,11	1,190	11,24	1,187
3	20	27,2	14.49	1,200	11,24	1,197
4	20	27,2	14,73	1,200	11,11	1,197
5	20	27,2	15,15	1,175	11,2	1,172
6	20	27,2	16,15	1,200	11,23	1,197

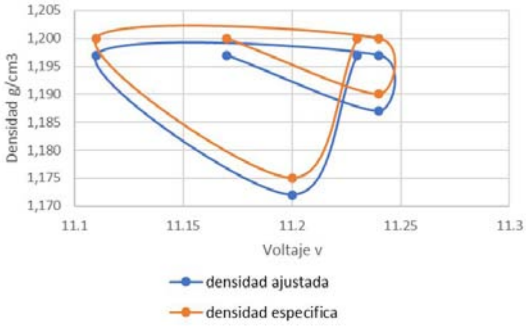

Figure 6. Plot of the behavior of the density after start-up at 20 °C.

The results are compared in the start-up test, to analyze the behavior of the voltage and density of the battery under extreme conditions, which results in a percentage of change of the ambient temperature of 0.39 % and of 3,1375 % with respect to the high and low temperature conditions, respectively. This indicates that the density of the electrolyte is more affected by low conditions, as opposed to the estimated time of start-up and voltage stability that are more affected by high temperature conditions, as can be seen in Figure 7.

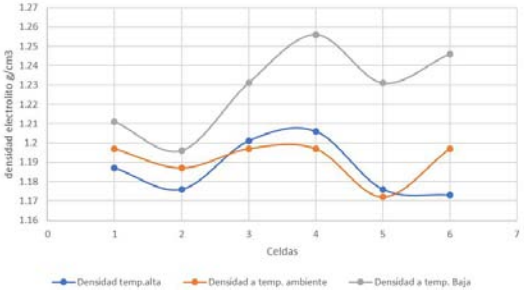

Figure 7. Comparison plot of the density at different temperatures

4. Conclusions

The figures show the change in density and voltage due to change in the temperature and stabilization. In addition, each point in the plots represents a cell, and shows the behavior of its electrolyte.

Figure 2 indicates the value of battery voltage before the consumption due to the start-up process. The stability of the accumulator during operation can be verified in both voltage and density.

Figure 3 indicates that the change in the battery voltage is not very significant due to the consumption at the moment of start-up, but the density of the electrolyte is altered, especially in the central cells.

An average of the operation of the cells indicates that the nominal tension keeps is maintained stable.

Figure 4 shows the value of the battery voltage before the consumption due to the start-up process. A stability can be observed in the density of the accumulator, but not in its voltage.

Figure 5 shows that the change in the battery voltage is very significant due to the consumption at the moment of start-up, but the change in the density of the electrolyte is small with respect to previous tests, especially in the final cells. This indicates that the stability drop in the operating conditions of the accumulator is more affected when the start-up process is carried out at low temperatures.

Figure 6 shows that the change in battery voltage is not very significant due to the consumption at the moment of start-up, but the density of the electrolyte is minimally altered in all cells. The stability drop in the operating conditions of the accumulator is more affected when the start-up process is carried out at ambient temperature.

Figure 7 presents the results corresponding to the behavior of the density at different temperatures. At low temperatures the density is more stable, but some strength is lost in the start-up condition. On the other hand, there is more start-up strength when hot, but the voltage drop is much greater.

The electrolyte density is directly proportional to the temperature change. When the temperature of the engine cabin increases to the higher values registered, the stability is maintained.

The stability condition of the density of the battery is altered, especially in the central and final cells, when the temperature drops significantly due to the displacement of electrons between them. This produces an abrupt drop in the voltage, but the recovery is much faster because the density of the electrolyte stabilizes.

The voltage remains constant as the temperature increases, but an extreme variation in the density occurs during start-up. This affects the operation and the durability of the battery, since its useful life is significantly reduced due to the variability in the density.

When the temperature of the electrolyte drops to its minimum values in real operation, there is an extreme change in the battery voltage, which produces a greater effort in the main consumers during the start-up process; this causes damage in the components of the vehicle.

When the electrolyte temperature decreases, the intensity drops due to the difficulty in the displacement of the electrons, placing a greater effort on the functionality of electric and electronic consumers. This would generate an improvement in the design of the structure of the batteries.

Based on the obtained results, it is concluded that the electrolyte temperature for different ambient conditions produces changes in the functionality. It is recommended to use new materials and designs, to improve the behavior of the battery during the start-up condition.

References

[1] J. E. Torres, A. Sierra, D. Y. Peña, I. Uribe, and H. Estupiñan, “Velocidad de corrosión de una aleación base plomo en una solución de ácido sulfúrico a diferentes temperaturas,” *Materia (Rio de Janeiro)*, vol. 19, pp. 182–196, 06 2014. [Online]. Available: https://goo.gl/tZqkW2

[2] A. Zolfaghari and G. Jerkiewicz, “Temperature-dependent research on pt(111) and pt(100) electrodes in aqueous h_2so_4,” *Journal of Electroanalytical Chemistry*, vol. 467, no. 1, pp. 177–185, 1999. [Online]. Available: https://doi.org/10.1016/S0022-0728(99)00084-4

[3] C. A. Cadena and R. F. Farfán, “Sensor de gaseo para baterías de plomo - ácido: estudio preliminar,” *Asociación Argentina de Energías Renovables y Ambiente; Avances en Energías Renovables y Medio Ambiente*, vol. 14, pp. 175–182, 2010. [Online]. Available: https://goo.gl/m9Ug3G

[4] D. Pavlov, *Lead-Acid Batteries: Science and Technology: A Handbook of Lead-Acid Battery Technology and Its Influence on the Product.* Elsevier, 2017. [Online]. Available: https://goo.gl/WMEFcn

[5] J. M. Alonso, *Técnicas del automóvil equipo eléctrico.* Thomson Paraninfo, 2005. [Online]. Available: https://goo.gl/4p4ymo

[6] D. Diemand, *Automotive Batteries at low temperatures.* US Army Corps of Engineers, 1991. [Online]. Available: https://goo.gl/uWhBMV

[7] D. Pavlov, A. Kirchev, M. Stoycheva, and B. Monahov, “Influence of h2so4 concentration on the mechanism of the processes and on the electrochemical activity of the pb/pbo2/pbso4

electrode," *Journal of Power Sources*, vol. 137, no. 2, pp. 288–308, 2004. [Online]. Available: https://doi.org/10.1016/j.jpowsour.2004.06.006

[8] ISO, *Road vehicles - Environmental conditions and testing for electrical and electronic equipment - Part 2: Electrical loads (ISO 160750-2)*, International Organization for Standardization Std. [Online]. Available: https://goo.gl/nSXN3w

[9] Megger, *Battery testing guide.* Megger, 2017. [Online]. Available: https://goo.gl/5RopkA

[10] E. Rojas, "Análisis de la densidad específica del electrolito de un acumulador de energía automotriz plomo ácido a diferentes temperaturas," *Sectei*, vol. 5, no. 1, pp. 80–84, 2018.

UNIVERSIDAD POLITÉCNICA SALESIANA ECUADOR
INGENIUS
Revista de Ciencia y Tecnología
pISSN: 1390-650X / eISSN: 1390-860X

GUIDELINES FOR PUBLICATION IN INGENIUS JOURNAL

1. General Information

INGENIUS is a scientific publication of the *Universidad Politécnica Salesiana* of Ecuador, published since January 2007, with a fixed biannual periodicity, specialized in Mechanical Engineering, Electrical Engineering, Electronics, Computer Science and its integration in what is now known as Mechatronics; these lines of action strengthen areas such as automation, control, robotics, among others..

It is a scientific journal, which uses the peer-review system, under double-blind review methodology, according to the publication standards of the Institute of Electrical and Electronics Engineers (IEEE). Compliance with this system allows authors to guarantee an objective, impartial and transparent review process, which facilitates the publication of their inclusion in reference databases, repositories and international indexing.

INGENIUS is indexed in the directory and selective catalog of the Regional Online Information System for Scientific Journals of Latin America, the Caribbean, Spain and Portugal (Latindex), in the Directory of Journals of Open Access DOAJ, In the Information Matrix for the Analysis of Journals, MIAR, In the Ibero-American Network of Innovation and Scientific Knowledge, REDIB and in repositories, libraries and specialized catalogs of Latin America.

The journal is published in a double version: printed (ISSN: 1390-650X) and digital (e-ISSN: 1390-860X), in Spanish, each work being identified with a DOI (Digital Object Identifier System. The articles sent to INGENIUS magazine must comply with the following criteria:

2. Scope and policy

2.1. Theme

Original contributions in Mechanical Engineering, Electrical and Electronic Engineering, Computer Science and its integration in what is now known as Mechatronics, as well as related areas: Automation, Control, Domotics, Robotics in their different fields of action and all those related disciplines with the same central theme.

All the work carried out by national or foreign researchers may be published once they meet the required scientific quality criteria.

2.2. Contributions

INGENIUS Journal preferably publishes articles related to empirical research, and also reports of technological development, proposals for models and innovations, products for the elaboration of graduate and postgraduate thesis that contribute to the field of science and technology, as well as select revisions of literature. (state-of-the-art).

- **Research:** 5,000 to 6,500 words of text, including title, abstracts, descriptors, charts and references.
- **Reports:** 5,000 to 6,500 words of text, including title, abstracts, charts and references.
- **Reviews:** 6,000 to 7,000 words of text, including charts and references. Current, selective and justified references, would be specially valued from among 40 works

The INGENIUS Journal publishes original and unpublished works written in Spanish and English, they may not have been published through any printed or electronic media, nor be in the process of arbitration or publication.

Every article will be subjected to a rigorous arbitration process; the evaluation of the article will be made according to criteria of originality, relevance, relevance, contributions, scientific rigor and compliance with established editorial guidelines.

Being an arbitrated publication, the Editorial Board approves its publication based on the concept of specialized pairs. The reception of a document does not imply commitment of publication.

It is essential to present a letter of presentation and grant of rights which can be downloaded from: <
urlhttps://goo.gl/ZNkMRD>.

Contributions must be exclusively sent and through the OJS (Open Journal System) <`https://goo.gl/JF7dWT`>. In which all authors must previously register as a user. For any consultation of the procedure you should contact:

<revistaingenius@ups.edu.ec>,
<jcalle@ups.edu.ec> ó
<mquinde@ups.edu.ec>.

3. Presentation and structure of the manuscripts

For those works that are empirical investigations, the manuscripts will follow the IMRDC structure (Introduction, Materials and Methods, Results and Discussion and Conclusions), being optional the Notes and Supports. Those papers that, on the contrary, deal with reports, studies, proposals and reviews may be more flexible in their epigraphs, particularly in material and methods, analysis, results, discussion and conclusions. In all typologies of works, references are mandatory.

Articles may be written on Microsoft Word (.doc or .docx) or LaTeX(.tex). The template to be used can be downloaded from the journal's website, a, <`https://goo.gl/gtCg6m`>, while for LaTeX in <`https://goo.gl/hrHzzQ`>, it is necessary that the file be anonymised in Properties of File, so that the author(s) ID is not displayed.

Figures, Graphs and/or Illustrations, as well as Charts shall be numbered sequentially including an explanatory description for each. The equations included in the article must also be numbered; the figures, charts and equations must be cited in the text.

Use space after point, commas and question marks.

Use “enter” at the end of each paragraph and title heading. Do not use .enter.anywhere else, let the word processor program automatically break the lines.

Do not center headings or subheadings as they should be aligned to the left.

Charts must be created in the same program used for the document body, but must be stored in a separate file. Use tabs, not spaces, to create columns. Remember that the final size of printed pages will be 21 x 28 cm, so the tables must be designed to fit the final print space.

3.1. Structure of the manuscripts

3.1.1. Presentation and cover letter

1. **Título (español) / Title (inglés):** Concise but informative, in Spanish on the front line and in English on the second, when the article is written in Spanish and vice versa if it is written in English.
2. **Authors and affiliations:** Full name and surname of each author, organized by order of priority and their institutional affiliation with reference to the end of the first sheet, where it must include: Dependency to which belongs within the

institution, Institution to which he/she belongs, country, ORCID. A maximum of 5 authors will be accepted, although there may be exceptions justified by the complexity and extent of the topic.

3. **Abstract (Spanish) / Abstract (English):** It will have a maximum extension of 230 words, first in Spanish and then in English. : 1) Justification of the topic; 2) Objectives; 3) Methodology and sample; 4) Main results; 5) Main conclusions.
4. **Keywords (Spanish) / Keywords (English):** 6 descriptors must be presented for each language version directly related to the subject of the work. The use of the key words set out in UNESCO's Thesaurus will be positively valued.
5. **Presentation (Cover Letter):** A statement that the manuscript is an original contribution, not submission or evaluation process in another journal, with the confirmation of the signatory authors, acceptance (if applicable) of formal changes in the manuscript according to the guidelines and partial assignment of rights to the publisher, according to the format established in: <`https://goo.gl/ZNkMRD`>

3.1.2. Manuscript

1. **Título (español) / Title (inglés):** Concise but informative, in Spanish on the front line and in English on the second, when the article is written in Spanish and vice versa if it is written in English.
2. **Authors and affiliations:** Full name and surname of each author, organized by order of priority and their institutional affiliation with reference to the end of the first sheet, where it must include: Dependency to which belongs within the institution, Institution to which he/she belongs, country, ORCID. A maximum of 5 authors will be accepted, although there may be exceptions justified by the complexity and extent of the topic.
3. **Abstract (Spanish) / Abstract (English):** It will have a maximum extension of 230 words, first in Spanish and then in English. : 1) Justification of the topic; 2) Objectives; 3) Methodology and sample; 4) Main results; 5) Main conclusions.
4. **Keywords (Spanish) / Keywords (English):** 6 descriptors must be presented for each language version directly related to the subject of the work. The use of the key words set out in UNESCO's Thesaurus will be positively valued.
5. **Introduction:** It should include the problem statement, context of the problem, justification, rationale and purpose of the study, using bibliographical citations, as well as the most significant and current literature on the topic at national and international level.
6. **Material and methods:** It must be written so that the reader can easily understand the development of the research. If applicable, it will describe the methodology, the sample and the form of sampling, as well as the type of statistical analysis used. If it is an original methodology, it is necessary to explain the reasons that led to its use and to describe its possible limitations.
7. **Analysis and results:** It will try to highlight the most important observations, describing, without making value judgments, the material and methods used. They will appear in a logical sequence in the text and the essential charts and figures avoiding the duplication of data.
8. **Discussion and Conclusions:** It will summarize the most important findings, relating the observations themselves to relevant studies, indicating contributions

and limitations, without adding data already mentioned in other sections. It should also include deductions and lines for future research.

9. **Supports and acknowledgments (optional):** The Council Science Editors recommends the author (s) to specify the source of funding for the research. Priority will be given to projects supported by national and international competitive projects.
10. **The notes (optional):** will go, only if necessary, at the end of the article (before the references). They must be manually annotated, since the system of footnotes or the end of Word is not recognized by the layout systems. The numbers of notes are placed in superscript, both in the text and in the final note. The numbers of notes are placed in superscript, both in the text and in the final note. No notes are allowed that collect simple bibliographic citations (without comments), as these should go in the references.
11. **References:** Bibliographical citations should be reviewed in the form of references to the text. Under no circumstances should references mentioned in the text not be included. Their number should be sufficient to contextualize the theoretical framework with current and important criteria. They will be presented sequentially in order of appearance, as appropriate following the format of the IEEE.

3.2. Guidelines for Bibliographical references

Journal articles:

[1] J. Riess, J. J. Abbas, "Adaptive control of cyclic movements as muscles fatigue using functional neuromuscular stimulation". IEEE Trans. Neural Syst. Rehabil. Eng vol. 9, pp.326–330, 2001. [Onine]. Available: https://doi.org/10.1109/7333.948462

Books:

[1] G. O. Young, "Synthetic structure of industrial plastics" in Plastics, 2nd ed., vol. 3, J. Peters, Ed. New York: McGraw–Hill, 1964, pp. 15–64.

Technical reports:

[1] M. A. Brusberg and E. N. Clark, "Installation, operation, and data evaluation of an oblique–incidence ionosphere sounder system," in "Radio Propagation Characteristics of the Washington–Honolulu Path," Stanford Res. Inst., Stanford, CA, Contract NOBSR–87615, Final Rep., Feb. 1995, vol. 1

Articles presented in confeences (unpubished):

[1] Vázquez, Rolando, Presentación curso "Realidad Virtual". National Instruments. Colombia, 2009.

Articles of memories of Conferences (Published):

[1] L. I. Ruiz, A. García, J. García, G. Taboada. "Criterios para la optimización de sistemas eléctricos en refinerías de la industria petrolera: influencia y análisis en el equipo eléctrico," IEEE CONCAPAN XXVIII, Guatemala 2008.

Thesis:

[1] L.M. Moreno, "Computación paralela y entornos heterogéneos," Tesis doctoral, Dep. Estadística, Investigación Operativa y Computación, Universidad de La Laguna, La Laguna, 2005.

Guidelines:

[1] IEEE Guide for Application of Power Apparatus Bushings, IEEE Standard C57.19.100–1995, Aug. 1995.

Patents:

[1] J. P. Wilkinson, "Nonlinear resonant circuit devices," U.S. Patent 3 624 125, July 16, 1990.

Manuals:

[1] Motorola Semiconductor Data Manual, Motorola Semiconductor Products Inc., Phoenix, AZ, 1989.

Internet resources:

[1] E. H. Miller, “A note on reflector arrays” [Online]. Available. https://goo.gl/4cJkCF

3.3. Epigraphs, Figures and Charts

The epigraphs of the body of the article will be numbered in Arabic. They should go without a full box of capital letters, neither underlined nor bold. The numbering must be a maximum of three levels: 1. / 1.1. / 1.1.1. At the end of each numbered epigraph will be given an enter to continue with the corresponding paragraph.

The charts must be included in the text according to order of appearance, numbered in Arabic and subtitled with the description of the content, the subtitle should go at the top of the table justified to the left.

Figures can be linear drawings, maps or black and white halftone or color photographs in 300 dpi resolution. Do not combine photographs and line drawings in the same figure.

Design the figures so that they fit eventually to the final size of the journal 21 x 28 cm. Make sure inscriptions or details, as well as lines, are of appropriate size and thickness so that they are not illegible when they are reduced to their final size (numbers, letters and symbols must be reduced to at least 2.5 mm in height After the illustrations have been reduced to fit the printed page). Ideally, the linear illustrations should be prepared at about a quarter of their final publication size.

Different elements in the same figure should be spelled a, b, c, etc.

Photographs should be recorded with high contrast and high resolution. Remember that photographs frequently lose contrast in the printing process. Line drawings and maps should be prepared in black.

The text of the figures and maps must be written in easily legible letters.

If the figures have been previously used, it is the responsibility of the author to obtain the corresponding permission to avoid subsequent problems related to copyright.

Each figure must be submitted in a separate file, either as bitmap (.jpg, .bmp, .gif, or .png) or as vector graphics (.ps, .eps, .pdf).

4. Submission process

The manuscript must be sent through the OJS system of the journal, <`https://goo.gl/JF7dWT`>,the manuscript should be uploaded as an original file in .pdf without author data and anonymized according to the above; In complementary files the complete manuscript must be loaded in .doc or .docx (Word file), that is to say with the data of the author (s) and its institutional ascription; Also the numbered figures should be uploaded in independent files according to the corresponding in the manuscript (as bitmap .jpg, .bmp, .gif, or .png or as vector graphics .ps, .eps, .pdf). It is also obligatory to upload the cover letter and grant of rights as an additional file.

All authors must enter the required information on the OJS platform and only one of the authors will be responsible for correspondence.

Once the contribution has been sent the system will automatically send the author for correspondence a confirmation email of receipt of the contribution.

5. Editorial process

Once the manuscript has been received in OJS, a first check by the editorial team of the following points:

- The topic is in accordance with the criteria of the journal.
- Must have the IMRDC structure.
- Must be in the Ingenius format.
- Must use the IEEE citation format.
- All references should be cited in the text of the manuscript as well as charts, figures and equations.
- The manuscript is original; for this, software is used to determine plagiarism.

The assessment described above can take up to 4 weeks.

If any of the above is not complete or there is inconsistency, an email will be sent to the author to make the requested corrections.

The author will make the corrections and resend the contribution through an email in response to the notification and will also upload the corrected manuscript into OJS supplementary files.

The editorial team will verify that the requested corrections have been incorporated, if it complies, the manuscript will start the second part of the process that may be followed by the author through OJS, otherwise the author will be notified and the manuscript will be archived.

The second phase of the process consists of the evaluation under the methodology of double-blind review, which includes national and foreign experts considering the following steps:

- The editor assigns two or more reviewers for the article.
- After reviewing the article, the reviewers will submit the evaluation report with one of the following results.
    - Publishable
    - Publishable with suggested changes
    - Publishable with mandatory changes
    - Non publishable
- The editor once received the evaluation by the reviewers will analyze the results and determine if the article is accepted or denied.
- If the article is accepted, the author will be notified to make corrections if required and the corresponding editorial process will be continued.
- If the article is denied, the author will be notified and the manuscript will be archived.
- In the two previous cases the result of the evaluation of the reviewers and their respective recommendations will be sent.

The second phase of the process lasts at least 4 weeks, after which they will be notified to the author giving instructions to continue with the process.

6. Publication

The Ingenius Journal publishes two issues per year, on January 1st and July 1st, so it is important to consider the dates for sending the articles and their corresponding publication. Articles received until October will be considered for the January publication and those received until April for the July publication.

UNIVERSIDAD POLITÉCNICA SALESIANA DEL ECUADOR
Javier Herrán Gómez, sdb
Rector

Turuhuayco 3-69 y Calle Vieja
Postal code 2074
Cuenca, Ecuador
Teléfono: (+593 7) 205 00 00
Fax: (+593 7) 408 89 58
Email: srector@ups.edu.ec

Exchange

Exchange with other periodicals is accepted.

Address:
Secretaría Técnica de Comunicación
Universidad Politécnica Salesiana
Turuhuayco 3-69 y Calle Vieja
Postal code 2074
Cuenca, Ecuador
Phone: (+593 7) 205 00 00 Ext. 1182
Fax: (+593 7) 408 89 58
Email: rpublicas@ups.edu.ec
www.ups.edu.ec
Cuenca – Ecuador

INGENIUS, Journal Science of Technology,
Semester publication, N.° 21, january/june 2019
John Calle Sigüencia, Editor in chief
revistaingenius@ups.edu.ec

Printed

Centro Gráfico Salesiano: Antonio Vega Muñoz 10-68 y General Torres.
Phone: (+593 7) 283 17 45
Cuenca – Ecuador
Email: centrograficosalesiano@lns.com.ec